Title

Towards High-Performance Tandem Photovoltaics Based on Metal Halide Perovskites

Permalink

https://escholarship.org/uc/item/8vt6n599

Author

Huang, Tianyi

Publication Date

2021

Peer reviewed|Thesis/dissertation

UNIVERSITY OF CALIFORNIA

Los Angeles

Towards High-Performance Tandem Photovoltaics Based on Metal Halide Perovskites

A dissertation submitted in partial satisfaction of the

requirements for the degree Doctor of Philosophy

in Materials Science and Engineering

by

Tianyi Huang

2021

ABSTRACT OF THE DISSERTATION

Towards High-Performance Tandem Photovoltaics Based on Metal Halide Perovskite

by

Tianyi Huang

Doctor of Philosophy in Materials Science and Engineering

University of California, Los Angeles, 2021

Professor Yang Yang, Chair

Organic-inorganic metal halide perovskites (MHPs) for photovoltaic applications have emerged rapid progress since their first successful demonstration since a decade ago. The record power conversion efficiency (PCE) of lab-sized (typically <1 cm^2) perovskite solar cells (PSCs) have risen from 14.1% to 25.5%, and small modules have reached 17.9% PCE in early 2021. With representative compositions including methylammonium lead triiodide (MAPbI$_3$), formamidinium lead triiodide (FAPbI$_3$), cesium lead triiodide (CsPbI$_3$), or hybrids of these cations with mixed halide compositions (e.g. FA$_x$Cs$_{1-x}$PbI$_3$, FA$_x$MA$_{1-x}$PbI$_{3-y}$Br$_y$), perovskite materials generally exhibit near infrared bandgap, ideal for single-junction solar cells. However, as the band edges formed by the hybridization of the electronic orbitals from the B-site lead and the X-site halide, the optical bandgap of perovskites could be precisely tuned by controlling the halide I/Br ratio, making configuring tandem photovoltaics with halide-perovskite possible which is also the core of this dissertation.

Starting from Chapter 1, I will give a brief introduction on MHPs and tandem photovoltaics.

The critical role of defect physics plays in halide perovskite solar cell's performance and stability will also be discussed in this chapter, and I will introduce my early work at UCLA in delivering a certified 22.0% efficiency monolithic perovskite-CIGS tandem which is the origin of most of my ideas proceed to this thesis.

After that, I will introduce strategies we developed that achieved highly efficient 4-terminal perovskite-Cu(In,Ga)(Se,S)$_2$ and perovskite-silicon tandem solar cells in Chapter 2. Numerical simulation and analysis unraveled the efficiency losses in the perovskite sub-cell were still the bottlenecking factor in limiting the performance of perovskite-based tandem photovoltaics. An electronic defects passivation strategy at perovskite surface were developed utilizing a synergetic effect of post-treated surface fluoride and phenethylammonium iodide (PEAI) that mitigated surface traps.

In Chapter 3, a more in-depth investigation of the surface reconstruction of perovskite during post-treatments was carried out at the microscale level based on a series of surface-sensitive or depth-resolved characterizations. A change of the perovskite surface could be induced by the commonly used post-treatment solvent, isopropyl alcohol (IPA), which directly affect the surface electronic affinity, surface termination, and surface defect feature. However, it was also found the IPA wash in fact assisted the ligand adsorption (e.g. PEA$^+$) to the perovskite surface and thus enhanced their defect passivation effect.

In Chapter 4, a set of in-situ or carefully designed ex-situ experiments were developed to distinguish the different formation dynamics and defect physics between the wide bandgap mixed-halide perovskite for tandem applications and the low bandgap tri-iodide perovskite for single junction solar cells, as the performance losses in the mixed-halide perovskite were significantly larger than their tri-iodide counterpart. The results show that the inclusion of bromide introduced a halide homogenization process during the perovskite growth stage from an initial bromide-rich phase

towards the final target stoichiometry. We further elucidated a physical model that correlates the role of bromide with the formation dynamics, defect physics, and eventual optoelectronic properties of the film.

After recognizing the critical role of surface properties and surface defects in halide perovskite, Chapter 5 will introduce a theoretical investigation of the formation and energy levels of perovskite surface defects. $FAPbI_3$, which is the composition that delivered the record photovoltaic performance among the perovskite family, was chosen for this study. All surface point defects were considered under two most commonly seems terminations, namely PbI_2 termination and FA-I termination. Insights of combining theoretical results and experimental outcomes were also discussed.

In Chapter 6, I will introduce organic small molecules named Y1 and Y2 that also showed tremendous potential in tandem application. They are non-fullerene acceptors (NFAs) with near infrared absorption and could serve as an ideal absorber as rear cell. The optoelectronic properties of Y1 and Y2 were delicately tuned by the introduction of unconventional electron-deficient-core-based fused structure, and their single junction devices exhibited a low voltage loss of 0.57 V and high short-circuit current density of 22.0 mA cm^{-2}, resulting in record-breaking power conversion efficiencies of over 13.4% (certified 12.6%).

The dissertation of Tianyi Huang is approved.

Subramanian S. Iyer

Xiaochun Li

Jaime Marian

Yang Yang, Committee Chair

University of California, Los Angeles

2021

The whole problem with the world is that fools and fanatics are always so certain of themselves, and the wiser people so full of doubts.

-Bertrand Russell

Table of Contents

List of Figures

Figure 2.3 Measurements and characterizations of the wide-band-gap perovskite cells. (A) J-V curves and (B) SPO profiles of the semitransparent perovskite cells with the targeted synergistic passivation treatment (target) and without any treatment (control). (C) EQE and transmittance spectra of the target cell. (E) J-V curves of the opaque perovskite cell with the target treatment. (E) PCE evolution of the target semitransparent cells without any encapsulation. First 1128 h was measured as ambient stability stored in dark, and the following 500 h was measured as operational stability kept under continuous illumination (90 ± 10 mW cm^{-2}), both under open-circuit condition.

Figure 2.4 Measurement and estimation results for the tandem solar cells. (A and B) J-V curves, (C and D) EQE spectra by combining the target semitransparent perovskite with commercially available silicon (blue) and CIGS (green) solar cells. The semitransparent perovskite cells without splitting into mini cells were used as an optical filter to measure the filtered characteristics of the rear cells. (E) An estimation for the efficiency loss for different bandgap materials with different V_{OC} losses. (F) The estimated PCE for tandem cells when the subcells' V_{OC} varies. The bandgaps of the front and the rear cells were assumed to be 1.64 eV and 1.03 eV, respectively.

Figure 3.1 Defect generation by IPA treatment. (a) Schematic of the in situ PL measurement during IPA post-treatment. (b) In situ PL contour plot of a perovskite film undergoing surface treatment with IPA dropped at around 53 s. (c) Evolution of the PL parameters extracted from fitting (b). (d) PAS depth-profiling of the perovskite films.

Figure 3.2 Characterizations of the perovskite films. (a) High-resolution XPS spectra of the Pb 4f and I 3d$_{5/2}$ peaks of the perovskite films. Inset includes the calculated I:Pb ratios of the films. Solid lines are fitted plots. Dashed vertical lines demarcate the peak positions for the

control film. Intensities are normalized to Pb 4f peak. (b) UPS spectra of the perovskite films. Inset includes a schematic band diagram of the energy levels based on the UPS measurements. GIXRD diffraction patterns of the perovskite films measured with an incident angle of (c) $\omega =$ 0.2° or (d) $\omega = 1.0°$.

Figure 3.3 Surface reconstruction and its implications. (a), (b) Theoretical slab models for first-principles DFT calculations. Atoms are colored black (lead), red (iodine), gray (nitrogen), and blue (hydrogen). (c) Calculated surface physiochemical properties. The asterisk indicates that surface energy is in units of eV nm^{-2}. (d) Enthalpy of adsorption of either PEAI or OAI on the surfaces. (e) Current density-voltage curves of devices treated with 10 mM OABr in CF. Inset includes the measured photovoltaic parameters. Brackets indicate parameters measured in forward bias. In situ PL contour plots of perovskite films undergoing surface treatment with (f) 10 mM OAI or (g) 10 mM PEAI in IPA.

Figure 4.1 Abnormal formation dynamics in wide bandgap mixed-halide perovskites. (A) Photographs of the as-cast (top) and fully annealed (bottom) perovskite films with the stoichiometries of $CsFAMAPb(I_{0.8}Br_{0.2})_3$ (left) and $CsFAMAPbI_3$ (right). (B) Absorption spectra of $FAMACsPbX_3$ films before(as-cast)/after fully annealed. (C) XRD spectra of (001) peak of $FAMACsPbX_3$ films.

Figure 4.2 In-situ photoluminescence measurements monitoring the formation kinetics of perovskite films. (A) Illustration of the in-situ PL measurement during spin-coating and annealing stage of perovskite formation. The contour plot of the captured PL spectra during the growth of (B) $CsFAMAPb(I_{0.8}Br_{0.2})_3$ and (C) $CsFAMAPbI_3$ films during spin-coating (left) and annealing (right). The extracted values of emission peak position (D), PL intensity (E), and FWHM (F) from the in-situ PL measurements.

Figure 6.1 Molecular structure and properties. (a) Chemical structure of the acceptor molecules. (b) Normalized absorption spectra of the acceptors Y1 and Y2. (c) energy diagrams of the materials used in OPVs.

Figure 6.2 Photovoltaic performance. (a) The J-V curves of PBDB-T:Y1 and :Y2 blend solar cells. (b) The EQE curves of PBDB-T:Y1 and :Y2 blend solar cells. (c) Statistical diagram of efficiency of PBDB-T:Y1 and :Y2. (d) Current-voltage parameters of PBDB-T:Y1 device certified (0.0548 cm2 device area) by Newport Corp.

Figure 6.3 Optical and electrical characterizations. (a) Fourier-transform photocurrent spectroscopy (FTPS) of PBDB-T:Y1 and Y2 blend solar cell. (b) The electroluminescence quantum efficiency of PBDB-T:Y1 and PBDB-T:Y2 blend solar cells at different injected currents. (c, d) Time-resolved PL for D:A blends and polystyrene (PS) blends. Black solid curves are fitting curves for extracting the lifetime $(\tau_{av} = \frac{\Sigma A_i \tau_i^2}{\Sigma A_i \tau_i})$.

Figure 6.4 Film morphology of blend films. (a-c) PBDB-T:Y1 films (a) Two-dimensional GIWAXS image (b), AFM image, and (c) TEM image; (d-f) PBDB-T:Y1 films (d) Two-dimensional GIWAXS image (e), AFM image, and (f) TEM image.

List of Tables

Acknowledgments

This dissertation and all work done during my PhD study have been supported by many and their great contributions behind. The PhD journey of me at UCLA could not be possibly completed without their help and guidance. My most sincere gratitude must go to these kind and wise minds who brought me here and accompanied me towards completing this journey.

First, I express my sincerest thanks to Prof. Yang Yang, my Ph.D. research advisor, for the opportunity to participate in his world-famous research group. Every idea and story shared by him has continuously driven me thinking into the fundamentals and challenging the established. During the years, I have never been lacking in inspiration, trust, and encouragement from my advisor, for which I thank him most. At the meantime, I would like to thank my committee members, Prof. Subramanian S. Iyer, Prof. Xiaochun Li, and Prof. Jaime Marian for their kind mentorship to my research.

I would also thank the faculties who I worked with in Materials Science and Engineering department as TA. They taught me how to teach and inspired me to set passing knowledge to the younger generation as one of my life-long missions. I must give my special thanks to Prof. Eric Bescher, who provided me my first TA opportunity and was so generous in sharing his amazing lecture skills.

As a member of YYLab, I was lucky to be mentored by the senior members at all time. Dr. Pei Cheng was the one who provided me my most preliminary PhD training when I started my OPV project at Prof. Yang's lab. He is a great mentor and friend with the most patience and kindest heart that helped me through the most challenging years of my early PhD study. Dr. Qifeng Han and Dr. Lei Meng taught me everything about halide perovskite and tandem solar cells, which turned out to be the main topic of this dissertation. There were so many unforgettable conversations

took place at the cleanroom we did CMP and the small office room we had technical discussions. Dr. Rui Wang and Dr. Jingjing Xue are the people I know who understand perovskite defect physics the best. They also taught me how to initiate cross-disciplinary collaborations. All these senior mentors have now become faculties in famous universities, and I sincerely wish their research career successful. I am also grateful to work with every research fellows, post-docs and graduate students in the group: Prof. Mingkui Wang, Prof. Zhao-Kui Wang, Prof. Yu Duan, Dr. Wenchao Huang, Dr. Bowen Zhu, Dr. Guangwei Xu, Dr. Le Cai, Dr. Dong Meng, Dr. Jin-Wook Lee, Dr. Pengyu Sun, Dr. Yao-Tsung Hsieh, Dr. Sheng-Yung Chang, Dr. Zhengxu Wang, Dr. Jun Yuan, Dr. Yuqiang Liu, Dr. Hao-Wen Cheng, Dr. Hao-Cheng Wang, Dr. Jiahui Zhu, Dr. Minhuan Wang, Dr. Selbi Nuryyeva, Dr. Quantan Wu, Ms. Zhiyu Zhao, Mr. Ran Zheng. I wish them the best for their life and career. For my fellow groupmates, Mr. Shaun Tan and Mr. Yepin Zhao, they have been like brothers during my PhD study, and I wish we all become who we want to be after getting our degree.

I would also like to thank my collaborators. Prof. Ilhan Yavuz, Prof. K.N. Houk, Prof. Yanfa Yan, and Dr. Canglang Yao provided tremendous computational supports. Dr. Carolin Sutter-Fella provided me the opportunity to work at LBNL with her team including Dr. Finn Babbe, Dr. Maged Abdelsamie, and Dr. Kootak Hong. I learned most of my knowledge of in-situ spectroscopic characterization from them. Dr. Marc Webber taught me about positron annihilation, which it was a very important tool in our perovskite research.

I am lucky to have my friends in the U.S. during my PhD study (I am pretty sure they feel the same to have me around too :D), especially we had COVID-19 pandemic hit the world during this time. Dr. Shiqi Dong and Dr. Lebo Wang are the loveliest couple I know, and I wish they are happy forever. I also got to know Dr. Xin Chen and his wife thanks to them, who were the warmest neighbor I ever had. I must thank Ms. Jin Cai, Ms. Zihang Peng, Mr. Dong Wu, Mr. Zeyan Liu and

Mr. Hao Yu for their company. Our friendship supported me during my PhD life, through the pandemic, and we shared a lot of sorrow and joy that every young people at our age would have. I also enjoyed every single philosophical and metaphysical conversation with Dr. Meng Gao and many others who have inspired, educated me through the years, to live as a human and justice being.

Lastly, I would like to give my deepest love and thank to my parents, grandparents, my girlfriend, and other family members in China. Travelling between U.S. and China was almost impossible during the pandemic, so it was their distant encouragement and blessing that have always accompanied me through the up and downs. I promise I won't fail your love ever.

Chapter 1 is a rewrite of *J. Phys. Chem. C* 2021, 125, 35, 19088–19096*, Nature Photonics* 2021, 15, 411–425, and *J. Phys. Energy* 3 042003; Chapter 2 is a version of *Small* (smll.202103887) just accepted as of writing; Chapter 3 is a version of *J. Am. Chem. Soc.* 2021, 143, 18, 6781–6786*;* Chapter 4 is a version of *Sci. Adv.* 2021 eabj1799; Chapter 5 is based on a manuscript submitted to *APL*; Chapter 6 is based on a version of *Nat Commun* 2019, 10, 570.

VITA

2013-2017   Bachelor's degree. Materials Chemistry, Sichuan University, Chengdu, China

2017-2021   Graduate Student Researcher, Department of Materials Science and Engineering, University of California, Los Angeles, CA, USA

2018-2019   Teaching Assistant, Department of Materials Science and Engineering, University of California, Los Angeles, CA, USA

2019-2021   Teaching Associate, Department of Materials Science and Engineering, University of California, Los Angeles, CA, USA

2021   Teaching Fellow, Department of Materials Science and Engineering, University of California, Los Angeles, CA, USA

Chapter 1 Introduction to metal halide perovskites and tandem photovoltaics

Photovoltaic (PV) technology has been considered as the most promising substitute for energy from traditional fossil fuels. In 1966, Shockley and Quessier calculated the theoretical power conversion efficiency (PCE) limit of a single-junction PV cell to be approximately 33% based on the principle of detailed balance.[1] In this scenario, most of the solar energy that cannot be utilized is attributed to spectrum loss, because of the limited optical response of semiconductor absorbers. Photons with an energy above the bandgap (E_g) can be absorbed by a semiconductor material and generate carriers with the identical energy of E_g. The excess energy is lost due to thermalization, and the photons with energy below E_g cannot be utilized. The E_g of an absorber is crucial to the PCE of a solar cell because E_g is correlated to both short-circuit current (J_{sc}) and open-circuit voltage (V_{oc}), which are the two crucial parameters of the PCE determines the total photocurrent and the voltage this photocurrent flows. To overcome the Shockley-Quessier limit (S-Q limit), tremendous strategies have been proposed and developed, such as multiple exciton generation,[2] hot carrier collection,[3] intermediate band structure,[4] and tandem architecture.[5] Among these studies, only tandem PV cells have practically surpassed the S-Q limit. The highest PCE of tandem devices achieved by a six-junction configuration has exceeded 47%.[6]

1.1 Basics of tandem photovoltaics

The basic working principle of tandem PVs is stacking different E_g junctions in optical series to mitigate the thermal energy loss of photogenerated carriers mentioned earlier and realize the efficient spectral splitting. The wider E_g absorber resides at the top to utilize and filter most of the high energetic photons, while the narrower E_g material at the bottom could absorb the rest low-energy photons, enabling maximum utilization of the solar spectrum (Figure 1.1A and B). The simplest tandem PV cell is based on a double-junction architecture, which contains one wide-E_g

front cell (~1.5-1.9 eV) and one narrow-E_g rear cell (~0.9-1.3 eV). Comparing with typical single junction solar cell, the ideal E_g is around 1.4~1.5 eV. The front and rear sub-cells can also be referred to as top and bottom sub-cells, respectively.

Double-junction tandem devices typically have two configurations based on how the two junctions are electrically connected: two-terminal (2-T) tandem and four-terminal (4-T) tandem. As shown in Figure 1.1C, 4-T tandem cells consist of two separate devices with their own electrodes, where the wide-E_g device and the narrow-E_g device are either mechanically stacked together or coupled with a spectral-splitting dichromatic mirror. The two subcells are fabricated individually and connected by an external circuit. Although the fabrication and operation processes of 4-T are relatively simple, the additional two electrodes and corresponding optical loss usually result in a high cost for this configuration.

On the other hand, the 2-T (or monolithic) tandem cell is fabricated sequentially on a single substrate with one transparent front electrode and one opaque rear electrode, where the front cell and rear cell are connected by an interconnection layer (ICL). As displayed in Figure 1.1D, the ICL is where the recombination of photogenerated charge carriers from the front and rear sub-cells occurs, to retain the charge neutrality, either in a metallic-like recombination layer or a band-to-band tunnelling junction layer. Generally, 2-T tandem PV can avoid extra manufacturing costs and parasitic optical loss, which makes it a little more promising than 4-T tandem cells in practical applications. However, owing to limitations in the fabrication process and the manipulation of electrical coupling, it is much more challenging to fabricate monolithic tandem cells than 4-T tandem cells and achieve high yield. The selection of ICL is affected by the surface roughness of the rear cell, compatibility of the solvent, and deposition temperature. More importantly, the bottom cell must be stable during the processing of the top cell and ICL, and the J_{sc} of both cells must be

well matched. That said, persistent research efforts have been devoted to achieving high-performance 2-T tandem PVs, where research on 4-T tandem often goes with the development of semi-transparent PVs.[7,8]

1.2 Metal halide perovskites

In the past decade, metal halide perovskite materials have been a focus of next-generation PV research due to their superior optoelectronic properties. With an approximate of only 11 years of rapid development, the record PCE of single-junction perovskite PVs has surged from an initial 3.8% to 25.5%.[9–15] The general chemical formula of a metal halide perovskite is ABX_3, where A refers to a monovalent cation like caesium (Cs^+), methylammonium (MA^+), or formamidinium (FA^+); B refers to a divalent cation like Pb^{2+} or Sn^{2+}; and X refers to a halide anion (Figure 1.1E). The remarkable bandgap tunability enabled by rich varieties of composition engineering is one of the major advantages of perovskite materials, which makes them versatile candidates as the subcell materials in a tandem device architecture. In light of this, perovskite-based tandem PVs in combination with several more matured photovoltaic technologies such as Si, $Cu(In,Ga)(S,Se)_2$ (CIGS), GaAs, and organic solar cells (or even low-bandgap perovskite itself) have been developed, and have the most potential to disrupt the commercial PV market dominated by conventional inorganic semiconductors. The highest certified PCE of perovskite-based tandem PV has reached 29.5% by stacking with Si by 2021 (NREL's Best Research-Cell Efficiency Chart).

Perovskite is also the only polycrystalline thin-film PV absorber material that has demonstrated >20% PCE with a wide bandgap (around 1.7 eV or larger). This makes perovskites uniquely fitted for tandem applications as the wide bandgap fron-cell, not only for all-perovskite tandem devices, but also for pairing with mature PV technologies (such as Si and CIGS) to further boost their performance. Since it is the valence band maximum and conduction band minimum are

3

composed by the orbitals of the lead and halide atoms, which allowed the tunability of the materials bandgap by easily controlling the composition especially the halide ratio. For example, $MAPbX_3$-based perovskites have been both theoretically and experimentally investigated to show a shift in the bandgap from ~2.25 eV for $MAPbBr_3$ to ~1.55 eV for $MAPbI_3$.[16,17] In fact, as the front cell, $MAPbBr_3$ successfully split $MAPbI_3$'s absorption spectrum in the visible light region, which allows effective current matching.

However, when the rear cell has an even lower bandgap, such as Pb-Sn perovskites (E_g ~ 1.25 eV), Si ($E_g = 1.1$ eV), or copper indium selenide (E_g ~ 0.98 eV), the optimal bandgap region for the front cell will be in the range from 1.8 eV to 1.65 eV to maximize current matching. McMeekin et al. systematically studied the halide composition tunability in the more thermally stable $FAPb(I_{1-x}Br_x)_3$ and $FACsPb(I_{1-x}Br_x)_3$ perovskites, in which case, caesium (Cs), is required to achieve continuous and stable perovskite bandgap evolution in the entire Br-to-I range, from ~2.25 eV when x=1 to ~1.53 eV when x=0.[19] Otherwise, a "yellowing" (highly degradable) of the $FAPb(I_{1-x}Br_x)_3$ films would occur for compositions of x between 0.3 and 0.6, associated with the transition from a trigonal (x < 0.3) to cubic (x>0.5) structure. With the optimal perovskite composition, $FA_{0.83}Cs_{0.17}Pb(I_{0.6}Br_{0.4})_3$, they achieved over 22%-efficiency perovskite/Si heterojunction tandem solar cells.

Although the goal in tuning the perovskite composition for front cells is to achieve suitable bandgaps, issues could arise, including phase instability and halide segregation in Br-rich systems. In fact, incorporating alkali elements such as Cs and Rb not only stabilizes the perovskite structure in the entire Br-to-I range, but also creates a more homogeneous halide distribution and suppresses halide segregation of these wide-bandgap perovskites driven by excited charge carriers upon further illumination or current injection.[20] When halide ions of different types segregate, such

inhomogeneity could lead to domains of higher (Br-rich) and lower (I-rich) bandgaps within one perovskite film,[21] resulting in photo-unstable optoelectrical properties including excess energy losses within the lower bandgap domain. This issue was observed to be more severe in MA-based perovskites, which could be barely resolved, even with A-site Cs incorporation.[20] As a result, most reported highly efficient wide-bandgap perovskite cells with high Br-to-I ratios have mixed FA-Cs double cation or FA-MA-Cs triple cation compositions.

Besides the challenges lying under successful bandgap engineering, interface properties and electronic defects are also critical in the case of tandem devices. Regardless of theoretically predicted defect tolerance, proper management of defects in halide perovskites is still necessary to achieve high mobility, long carrier lifetimes, minimized nonradiative losses, and thus high-performance solar cells. Defects are also reported to easily capture moisture and oxygen and become where device degradation initiates. In fact, like most crystalline semiconductors, defect management in perovskite materials starts from the first step in their processing, which includes composition engineering and crystal growth, and eventually it was my attempt to link the dots between these aspects for highly efficient perovskite-based tandem photovoltaics.

1.3 Defect physics in metal halide perovskites

Taking $APbI_3$ lead tri-iodide perovskites (A: methylammonium (MA) or formamidinium (FA)) as an example (while the anion site can also be Br or a mixture of Br/I), it can form twelve types of intrinsic point defects, namely the three interstitial defects (A_i, Pb_i, I_i), three vacancy defects (V_A, V_{Pb}, V_I) and six antisite defects (A_{Pb}, A_I, Pb_A, Pb_I, I_A, I_{Pb}). Theoretical studies have shown that the dominant defects with low formation energies have transition levels within 0.05 eV of the conduction or valence band edges, making them shallow in nature and thus do not act as Shockley-Read-Hall non-radiative recombination centers (Table 1.1).[22,23]

However, it is also known that the photoluminescence quantum yields and open-circuit voltages (V_{OC}) of perovskite thin films and devices are still not at their theoretical limits, suggesting that deep traps still detrimentally contribute to recombination energy losses limiting the performance of perovskite solar cells (PSCs).[24,25] Moreover, due to the characteristic ionic nature of perovskites, defects are mobile under an electric field, and this phenomenon is known to be responsible for photocurrent hysteresis, photoinduced phase segregation, and long-term operational instability of PSCs.[26–29] Shallow defects are particularly mobile due to their low activation energies for migration, typically <0.5 eV.[8] Moreover, defects can also accelerate the phase degradation of metastable cubic FAPbI$_3$ into its photoinactive hexagonal delta phase,[30] especially relevant since the vast majority of high-performance PSCs are based on a majority FAPbI$_3$ composition. Given the detrimental consequences on efficiency and stability, it is thus necessary to apply defect mitigation and passivation strategies to realize high performance PSCs.

Even though significant progress achieved in understanding the role of defects in perovskite, it remains challenging to identify specific defect species, pinpoint their location and distribution, or elucidate their energetics and formation. Despite advanced computational studies on these subjects, direct experimental evidence may still be lacking. These are crucially necessary in order to rationally explain the fundamental mechanisms of how and why certain strategies work. Moreover, such knowledge would facilitate the design of more effective targeted mitigation strategies, for example, by screening for more ideal chemical structures to maximize the beneficial effects.

Relatedly, there is a lack of experimental characterization tools that can directly and unambiguously detect and visualize defects. This is due in large part to the soft nature and sensitivity of perovskite materials, which makes them incompatible with various characterizations

such as conventional high-resolution electron microscopy. Some of the most common complementary tools used for defect studies include PL spectroscopy, admittance spectroscopy, and SCLC, but these are unable to directly detect and resolve defects. Some recent developments have aimed at tackling this issue. Positron Annihilation Spectroscopy (PAS) is a spatially-resolved, non-destructive technique that can distinguish defects based on their charge, recently utilized to identify iodine interstitials and formamidinium vacancies at the surface.[30,31] Aberration-corrected HRTEM equipped with low dose sensitivity has also been used to directly visualize individual point defects at the atomic scale.[32]

1.4 Monolithic perovskite-CIGS tandem solar cells

As it is discussed in Chapter 1.1, $Cu(In,Ga)(S,Se)_2$ (CIGS) with a bandgap ~1.0 eV is an ideal rear cell candidate to couple with wide bandgap perovskite materials for tandem applications. Compared with silicon, CIGS has a lower bandgap that can cover an even larger solar spectrum. As a polycrystalline thin film solar cell, its deposition can be carried out on a large variety of substrates from soda-lime glass to stainless steel foils to deliver flexible PVs. Calculated by researchers from Swiss Federal Laboratories for Materials Science and Technology (EMPA), CIGS-perovskite tandem with the state-of-the-art bandgap ranges can theoretically achieve 43.6% PCE for the 2-T design and 44.5% for the 4-T design.

My pioneering work on perovskite-based tandem PVs initiated from delivering this proof-of-concept on monolithic perovskite-CIGS tandem. CIGS adopts a front-illumination configuration where the surface TCO layer (usually AZO or BZO) functions as both a window layer for light to penetrate through and a transparent electrode for electrical contact. For a monolithic tandem device, the thin film perovskite cell needs to be directly deposited on the CIGS cell in order to be optically coupled together. Such a device design led to three major challenges for the perovskite cell

fabrication: 1. transparent electrode for the perovskite front cell is required so photons with energy lower than the bandgap could go pass the entire perovskite front cell and captured by the CIGS rear cell; 2. bandgap of the perovskite absorber must be carefully tuned to tailor the total absorption of the tandem to achieve photocurrent matching of the sub-cells; 3. making the surface morphology of polycrystalline CIGS cell compatible for the upcoming perovskite cell deposition.

The device structure of the perovskite sub-cell was redesigned to be substrate (either glass or the CIGS cell as the substrate)/ITO/poly[bis(4-phenyl)(2,5,6-trimethylphenyl)amine (PTAA, 20 nm)/perovskite (800 nm)/phenyl-C61-butyric acid methyl ester ($PC_{61}BM$, 30 nm)/ZnO nanoparticles (~15nm)/ITO, where the ZnO nanoparticles layer was intentionally inserted before the final sputter ITO deposition to form a compact buffer layer to protect the fragile organics from the mechanical damage during sputtering. The bandgap of the perovskite absorber was delicately tuned by controlling the halide ration and the cation composition to be in the range of 1.64-1.68 eV with 17-20% of I% substituted by Br% to pair with the CIGS cell, while suppressing the potential (but unfavourable) halide segregation at the same time. More details about the near-infrared (NIR) transparency of these perovskite front-cells and physics in mixed-halide perovskite are discussed in Chapter 2 and Chapter 4.

The most challenging part is to integrate the efficient wide bandgap NIR transparent perovskite front cell with the CIGS rear cell. The surface profile of the CIGS rear cell usually exhibits a roughness up to several hundreds of nanometres (inherited from the CIGS absorber layer), shown in Figure 1.2A. This roughness was extremely unfavoured for the deposition of the perovskite cell, since the all charge transporting layers and the perovskite absorber layers must be prepared by solution process (spin-coating) which is not a conformal deposition. As a result, discontinuity during solution deposition can occur, especially for the transporting layers whose

thickness are only tens of nanometres, leading to the collapse of the perovskite cell junction. To flatten the CIGS rear cell surface without damaging the junction in it, a sacrificial ITO layer was sputtered to the CIGS surface. This ITO layer that inherits the surface roughness was then polished by chemical mechanical polishing (CMP) to reduce the surface roughness to approximately 20 nm (Figure 1.2B and C). With this strategy, the CIGS cell was flattened, and the deposition of the planer perovskite cell was made possible. Figure 1.1D showed the device structure of the monolithic perovskite-CIGS tandem cell, a clear transition from the rough CIGS cell to the planer perovskite cell interconnected by the polished ITO layer could be visualized. The device was sent to National Renewable Energy Laboratory (NREL) for a third-party certification measurement, and a power conversion efficiency as high as 22.0% was achieved (Figure 1.3).

1.5 References

1. Shockley, W. & Queisser, H. J. Detailed balance limit of efficiency of p-n junction solar cells. *J. Appl. Phys.* **32**, 510–519 (1961).

2. Beard, M. C. Multiple exciton generation in semiconductor quantum dots. *J. Phys. Chem. Lett.* **2**, 1282–1288 (2011).

3. Knig, D. *et al.* Hot carrier solar cells: Principles, materials and design. *Phys. E Low-Dimensional Syst. Nanostructures* **42**, 2862–2866 (2010).

4. Okada, Y. *et al.* Intermediate band solar cells: Recent progress and future directions. *Appl. Phys. Rev.* **2**, (2015).

5. De Vos, A. Detailed balance limit of the efficiency of tandem solar cells. *J. Phys. D. Appl. Phys.* **13**, 839–846 (1980).

6. Geisz, J. F. *et al.* Six-junction III–V solar cells with 47.1% conversion efficiency under 143 Suns concentration. *Nat. Energy* **5**, 326–335 (2020).

7. Barnett, A. M. The Spectral p-n Junction Model for Tandem Solar-Cell Design. *IEEE Trans. Electron Devices* **34**, 257–266 (1987).

8. Brown, A. S. & Green, M. A. Detailed balance limit for the series constrained two terminal tandem solar cell. *Phys. E Low-Dimensional Syst. Nanostructures* **14**, 96–100 (2002).

9. Wang, R. *et al.* Constructive molecular configurations for surface-defect passivation of perovskite photovoltaics. *Science.* **366**, 1509–1513 (2019).

10. Min, H. *et al.* Efficient, stable solar cells by using inherent bandgap of a-phase formamidinium lead iodide. *Science.* (2019). doi:10.1126/science.aay7044

11. Yang, S. *et al.* Stabilizing halide perovskite surfaces for solar cell operation with wide-bandgap lead oxysalts. *Science.* (2019). doi:10.1126/science.aax3294

12. Xue, J. *et al.* Crystalline Liquid-like Behavior: Surface-induced secondary grain growth of photovoltaic Perovskite Thin Film. *J. Am. Chem. Soc.* **141**, 13948–13953 (2019).

13. Tan, H. *et al.* Efficient and stable solution-processed planar perovskite solar cells via contact passivation. *Science).* **355**, 722–726 (2017).

14. Kim, H. S. *et al.* Lead iodide perovskite sensitized all-solid-state submicron thin film mesoscopic solar cell with efficiency exceeding 9%. *Sci. Rep.* **2**, 591 (2012).

15. Kojima, A., Teshima, K., Shirai, Y. & Miyasaka, T. Organometal halide perovskites as visible-light sensitizers for photovoltaic cells. *J. Am. Chem. Soc.* (2009). doi:10.1021/ja809598r

16. Saidaminov, M. I. *et al.* High-quality bulk hybrid perovskite single crystals within minutes by inverse temperature crystallization. *Nat. Commun.* **6**, 1–6 (2015).

17. Jesper Jacobsson, T. *et al.* Exploration of the compositional space for mixed lead halogen perovskites for high efficiency solar cells. *Energy Environ. Sci.* **9**, 1706–1724 (2016).

18. Heo, J. H. & Im, S. H. CH3NH3PbBr3–CH3NH3PbI3Perovskite–Perovskite Tandem Solar

Cells with Exceeding 2.2 V Open Circuit Voltage. *Adv. Mater.* **28**, 5121–5125 (2016).

19. McMeekin, D. P. *et al.* A mixed-cation lead mixed-halide perovskite absorber for tandem solar cells. *Science.* **351**, 151–155 (2016).

20. Braly, I. L. *et al.* Current-Induced Phase Segregation in Mixed Halide Hybrid Perovskites and its Impact on Two-Terminal Tandem Solar Cell Design. *ACS Energy Lett.* **2**, 1841–1847 (2017).

21. Correa-Baena, J. P. *et al.* Homogenized halides and alkali cation segregation in alloyed organic-inorganic perovskites. *Science.* **363**, 627–631 (2019).

22. Yin, W.-J., Shi, T. & Yan, Y. Unusual defect physics in CH 3 NH 3 PbI 3 perovskite solar cell absorber. *Appl. Phys. Lett.* **104**, 063903 (2014).

23. Liu, N. & Yam, C. First-principles study of intrinsic defects in formamidinium lead triiodide perovskite solar cell absorbers. *Phys. Chem. Chem. Phys.* **20**, 6800–6804 (2018).

24. Braly, I. L. *et al.* Hybrid perovskite films approaching the radiative limit with over 90% photoluminescence quantum efficiency. *Nat. Photonics* **12**, 355–361 (2018).

25. Yang, Y. *et al.* Top and bottom surfaces limit carrier lifetime in lead iodide perovskite films. *Nat. Energy* **2**, 16207 (2017).

26. Tan, S. *et al.* Steric Impediment of Ion Migration Contributes to Improved Operational Stability of Perovskite Solar Cells. *Adv. Mater.* **32**, 1906995 (2020).

27. Meloni, S. *et al.* Ionic polarization-induced current–voltage hysteresis in CH3NH3PbX3 perovskite solar cells. *Nat. Commun.* **7**, 1–9 (2016).

28. Azpiroz, J. M., Mosconi, E., Bisquert, J. & Angelis, F. De. Defect migration in methylammonium lead iodide and its role in perovskite solar cell operation. *Energy Environ. Sci.* **8**, 2118–2127 (2015).

29. Huang, T., Tan, S. & Yang, Y. Material, Phase, and Interface Stability of Photovoltaic Perovskite: A Perspective. *J. Phys. Chem. C* **125**, 19088–19096 (2021).

30. Tan, S. *et al.* Shallow Iodine Defects Accelerate the Degradation of α-Phase Formamidinium Perovskite. *Joule* **4**, 2426–2442 (2020).

31. Tan, S. *et al.* Surface Reconstruction of Halide Perovskites During Post-treatment. *J. Am. Chem. Soc.* **143**, 6781–6786 (2021).

32. Rothmann, M. U. *et al.* Atomic-scale microstructure of metal halide perovskite. *Science* **370**, eabb5940 (2020).
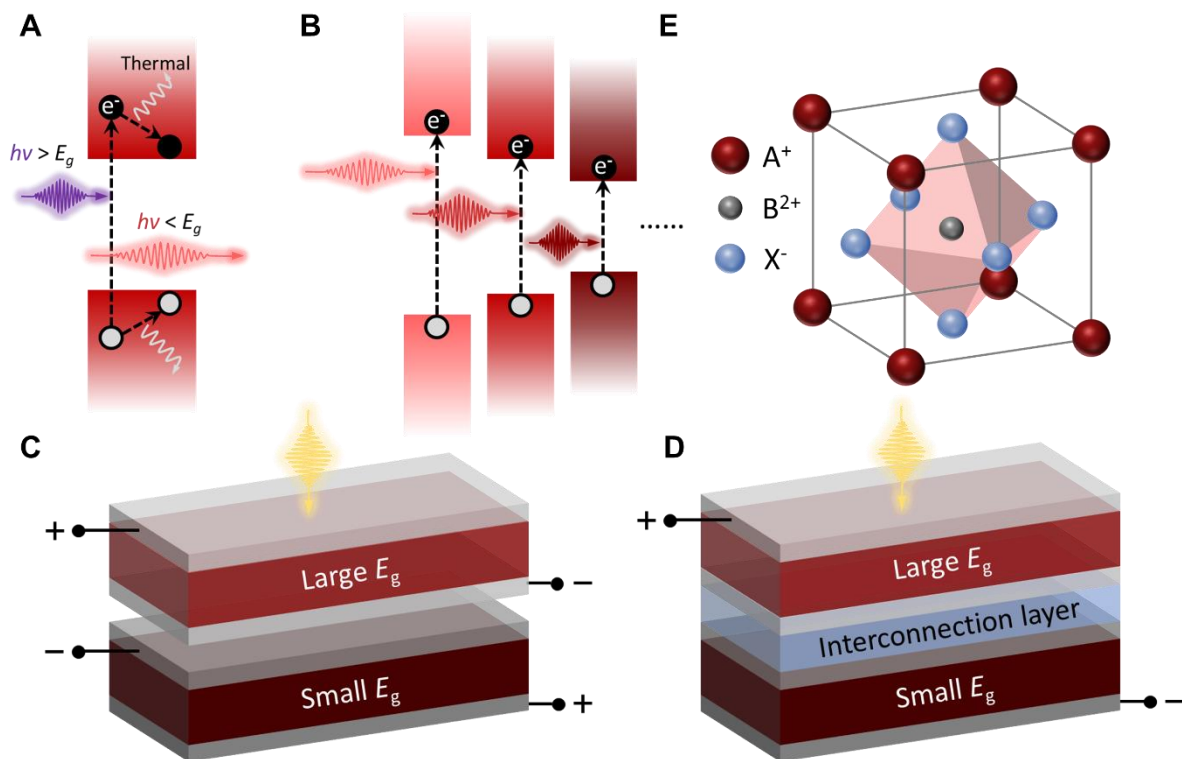
Figure 1.1 Introduction of Tandem Photovoltaics and Metal Halide Perovskites. Schematic illustration showing light absorption in A. single and B. multijunction photovoltaics. C. Four-terminal and D. two-terminal tandem photovoltaics. E. Crystal structure of metal halide perovskites.
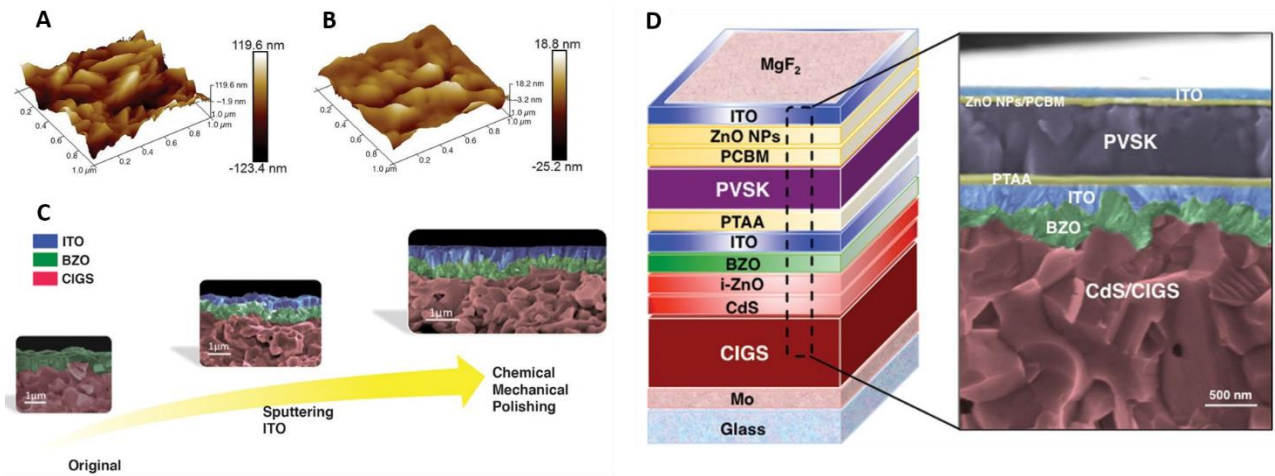
Figure 1.2 Monolithic perovskite-CIGS tandem device. AFM results for the pristine (A) and polished (B) CIGS cell surface. C. Schematic illustration showing the CIGS surface flattening strategy. D. Schematic illustration of the monolithic perovskite-CIGS tandem device structure and the cross-sectional SEM of the device.

14

UCLA

Perovskite/CIGS Tandem Cell

Device ID: A1-09

11:33 AM 3/26/2019

Spectrum: ASTM G173 global

Device temperature: 0.0 ± 0.0 °C

Device area: 0.025 cm^2 ± 1.3%

Irradiance: 1000.0 W/m^2
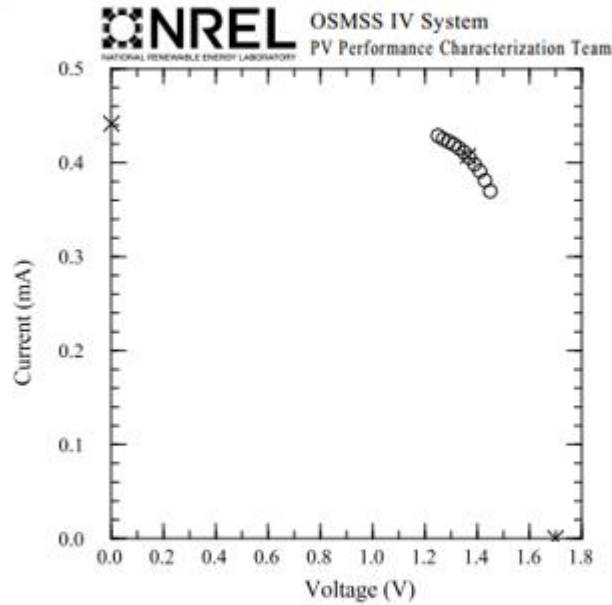
OSMSS IV System

PV Performance Characterization Team

V_{oc} = 1.6995 V ± 0.4%

I_{sc} = 0.44144 mA ± 1.4%

J_{sc} = 17.450 mA/cm^2 ± 1.8%

I_{max} = 0.40699 mA ± 1.6%

V_{max} = 1.3645 V ± 0.4%

P_{max} = 0.55535 mW ± 1.9%

Efficiency = 21.95 ± 0.53%

elapsed P_{max} time: 286 s

0.1%/min current slope

Figure 1.3 Certification report of the monolithic perovskite-CIGS tandem champion device at NREL.

Table 1.1 Formation energies (in eV) of the twelve neutral defects in MAPbI$_3$ and FAPbI$_3$ under moderate conditions.[2,3]

	Interstitial defects			Vacancy defects			Antisite defects					
	A_i	Pb_i	I_i	V_A	V_{Pb}	V_I	A_{Pb}	A_I	Pb_A	Pb_I	I_A	I_{Pb}
MAPbI$_3$	0.93	2.91	0.83	1.28	1.62	1.27	1.15	2.25	2.51	3.62	3.01	3.45
FAPbI$_3$	1.86	2.29	1.13	0.54	1.95	1.16	1.61	1.27	1.69	3.01	1.37	2.34

Chapter 2 Wide-gap perovskite via synergetic surface passivation and its application towards efficient stacked tandem PVs

Multi-junction solar cells mitigate the unavoidable thermalization losses in traditional single-diode-based photovoltaics (PVs) that limit their maximum performance. By tailoring the solar spectrum harvesting by proper choice of absorbers with cascading band gaps [1], multi-junction solar cells have the potential to overcome the single-junction Shockley-Queisser efficiency limit of 33.7%. Commercial multi-junction solar cells are limited to the costly III-V semiconductor-based technologies, however the emergence of solution-processable organic metal halide perovskites at the bandgap between 1.65-1.70 eV has enabled the development and initiated the recent surge in multi-junction solar cells based on rear cells such as Sn-Pb perovskite[2,3] or commercialized PVs such as silicon and $Cu(In,Ga)(S,Se)_2$ (CIGS) [4–9].

As of writing, the record power conversion efficiency (PCE) for perovskite-based tandem solar cells is 29.5%, achieved in late 2020 by Oxford PV with a 2-terminal design.[10] However, the mismatch of long-term stability between halide perovskite and silicon (or CIGS) still limits the useful lifetime of perovskite-silicon tandem solar cells (commercial silicon solar cells generally have ~30 years lifetime warranty). Stacked tandem structure, adopting a 4-terminal configuration based on a semitransparent transparent perovskite cell and a commercially available silicon or CIGS cell, could be a potential solution to this lifetime challenge. Compared with monolithic tandem, this device configuration includes several advantages including the unnecessity of current matching, "replacement" of the stacked perovskite cell after it expires, and the possibility of maintaining the optimum process for both cells.

In this chapter, a highly efficient wide bandgap (WBG) semitransparent perovskite cell was developed by introducing a thin fluoride layer in between the organic ammonium ligand and the perovskite surface that a synergistically amplified trap passivation effect. The PCE of the WBG

semitransparent cell was improved from 15.4% to 17.7% as the modulated trap passivation interaction exhibited preferred alignment of the interface energy band and effective suppression of the non-radiative energy losses. With the champion semitransparent perovskite cell, the stacked tandem structure boosted c-Si and CIGS with original efficiencies of 18.0% and 20.2% (both provided by commercial PV companies) to over 25%, and a theoretical 28.1% PCE could be achieved given the availability of the record silicon cell. These improvements achieved by the amplified trap passivation and the stacked configuration provides a crucial step towards integrating perovskite PVs into the current PV market and lowering the levelized cost of energy (LCEO) without either sacrificing their long-term operation or having to modify the current product line of commercial PV industries [11].

2.1 Post-treatment by ammonium salts for wide-gap perovskite

The genesis of this approach originates from the seek for surface trap passivation strategies that most effectively mitigate voltage deficits in WBG perovskite cells for tandem PVs. These perovskite devices usually adopt a p-i-n configuration (to be compatible with the process of sputtered TCO window layer), where post-deposition of an ultra-thin electrically inert alkali fluoride layer on top of perovskite is the most used strategy for suppression of surface defects. However, many of the recent highly efficient single junction perovskite solar cells utilize organic cations with ammonium ($-NH_3^+$) functionalities for surface passivation such as phenylethylammonium iodide (PEAI), octylammonium iodide (OAI), oleyammonium iodide (OLAI) etc.[12,13]

The compatibility of these two distinct approaches and the potential synergetics when both species simultaneously exist on the perovskite surface, however has rarely been studied. In fact, from Fourier-transform infrared (FTIR) spectroscopy for a PEAI and alkali fluoride mixture

18

(potassium fluoride was used in this work) shown in Figure 2.1A, we identified a downshift of ~50 cm^{-1} from 2910 cm^{-1} to 2860 cm^{-1} vibrational frequency for the N-H bond stretching vibration in PEAI when the fluoride was introduced. Considering that the C-H and O-H vibrational frequencies also populate this IR region, we also referred to the N-H bond bending mode of PEAI samples found at 1564 cm^{-1}, which also downshifted to 1535 cm^{-1} in the fluoride mixture. Clearly, there exists a strong interaction between the fluoride and the ammonium group of PEAI that leads to shifting in the vibration modes, as a result of which their dynamics when co-existing at defective perovskite surface could be more complicated.

To investigate these interactions and understand whether the synergetic effects benefit the surface charge carrier properties, the target samples were prepared by thermally evaporating the fluoride to the surface of a triple cation mixed halide perovskite (approx. E_g = 1.64 eV), followed by spin-coating of 10 mM PEAI solution dissolved in isopropyl alcohol (IPA), also denoted as PVSK-F-PEAI. The PEAI-only and fluoride-only perovskite samples were also prepared (denoted as PVSK-PEAI, PVSK-F, and control sample without any treatments as PVSK). From high-resolution X-ray photoelectron spectroscopy (XPS) measurements shown in Figure 2.1B, the characteristic Pb 4f orbital peaks were located at 138.66 eV and 143.55 eV for Pb 4f 7/2 and Pb 4f 5/2, respectively, for the control sample. Both surface treatments individually showed strong interaction with the electronic orbitals of Pb 4f. Treatment with only PEAI shifted the peaks to higher binding energies of 138.92 eV and 143.79 eV, and treatment with fluoride alone also shifted them to 138.80 eV and 143.69 eV. The target samples sequentially post-treated with fluoride then PEAI demonstrated the strongest interaction with the surface Pb orbitals, with the corresponding binding energy shifting to 139.13 eV for the Pb 4f 7/2 peak and 144.00 eV for the Pb 4f 5/2 peak, respectively. Similar shifting was also observed for the I 3d characteristic peaks, where the target

treatment with both F and PEAI showed the largest shifts to higher binding energies, similar to the Pb 4f orbitals. Instead of countering the surface passivation effect, these results suggested that the insertion of the fluoride emerges to enhance the interaction.

Ultraviolet photoelectron spectroscopy (UPS) unraveled additional surface electronic properties affected by the treatments (Figure 2.1C). The extracted valence band maximum (VBM) and the work function (WF) energy levels of the films were summarized in Supplementary Figure C2.2. The kinetic energy cutoff and fermi level remained mostly unchanged with the fluoride treatment and remained at 16.10 eV and 0.58 eV, respectively. However, PEAI treatment tremendously decreased the surface WF of the film as the energy cutoff shifted to 16.39 eV. With the fermi level determined to be at 0.70 eV, the PEAI treatment turned the perovskite surface into slightly n-type. Interestingly, the target treatment led to a smallest work function among all treatments, where largest shifting in the energy cutoff was observed. While the fluoride treatment alone did not markedly affect the surface energy levels, it does synergistically amplify the effect of PEAI and lead to an even more n-type perovskite surface, which is rather preferential in the inverted device configuration adopted by most semitransparent perovskite cells or in perovskite-based tandem cells.[14]

To rationalize the experimentally observed synergies between the defective perovskite surface and the post-treating materials at an atomic scale, density functional theory (DFT) calculations were carried out (see Supplementary Text A2.1). The perovskite surface models specifically with the iodine vacancy (V_I) and Pb-I antisite (Pb_I) defects were used for computations, due to their lowest formation energies on formamidinium-based perovskite surface as per our previous study[15]. As shown in Supplementary Figure C2.1 and C2.5, DFT calculations show a strong interaction of PEA with both charged defects at the perovskite surface at the conduction

band minimum (CBM) with interaction energy of -1.7 eV with V_I and Pb_I. All interaction energy calculations on neutral defects near valence band maximum (VBM) show a similar trend (see details in the Appendix). We observed favorable electrostatic stabilization and hydrogen-bonding between the ammonium group of PEA and the iodine on the perovskite surface with an average N-H•••I bond length of as short as 2.5 Å. In the case of Pb_I defect, the phenyl group of PEA slightly tilts towards the interstitial Pb, engaging in a cation-π interaction further stabilizing the complex.

Given the strong proton-donating character of ammonium, the fluoride would more likely participate in the interaction between the ammonium salt and the surface defects rather than the alkali cation introduced simultaneously during the fluoride treatment. It was found that the fluoride preferred to occupy a thermodynamically stable site near both defects (as shown in Supplementary Figure C2.4 and C2.5). The interaction energy between PEA and both V_I and Pb_I defects at CBM increased to -3.8 eV and -3.6 eV, respectively, when the fluoride was present. Interestingly, two different modes of synergy between PEA was observed, the fluoride and the surface defects. Due to its smaller size compared to iodine, the fluoride, in the case of V_I, acts as an anchor that forms stronger electrostatic bonds with the ammonium group of PEA, which as a result strengthens the interaction of PEA with the defects on the surface of the perovskite. In the case of Pb_I, while the fluoride lodges itself between the antisite and native lead atoms, the phenyl group coordinates to the interstitial lead. This synergistic dynamic of fluoride and PEA in both Pb_I and V_I surface defects are hypothesized to play a significant role in increased interaction energies that could potentially lead to an even stronger passivating effect.

2.2 Synergetic defect passivation effect of the post-treatment

Photoluminescence (PL) spectroscopy analysis of the perovskite films prepared on glass substrates without transporting layers was performed to evaluate the defect passivation effect and

surface charge carrier dynamics. As shown in Figure 2A, both PEAI and the fluoride treatment enhanced the PL intensity as nonradiative recombination was suppressed via defect passivation. The sample treated with both fluoride and PEAI exhibited the strongest signal. Similar trend was observed when treating with another commonly used organic ammonium salt, OAI (Figure A2.3). Time-resolved photoluminescence (TRPL) spectroscopy results shown in Figure 2B also point to the existence of the synergy on the surface. The fitted parameters (bi-exponential decay model, see Supplementary Text A2.2) suggest that the PEAI treatment alone significantly increases the carrier lifetime from $\tau_{average}$ = 291.6 ns (τ_1 = 2.5 ns, τ_2 = 336.6 ns) to $\tau_{average}$ = 371.4 ns (τ_1 = 34.4 ns, τ_2 = 482 ns), while treatment with just F enhanced the $\tau_{average}$ to 532.3 ns (τ_1 = 34.3 ns, τ_2 = 708.5 ns). Both surface treatments separately improved the carrier decay profile. With both treatments present, the perovskite film showed the longest carrier lifetime of $\tau_{average}$ = 677.1 ns (τ_1 = 39.4 ns, τ_2 = 1336.6 ns), indicating the most improved and superior charge recombination dynamics when the interaction between the perovskite surface defects and PEAI was enhanced with the fluoride bridge. Together with our DFT studies pinpointing the most favorable occupancy location for F, it is highly possible that the synergistic effect was established by facilitating a stronger hydrogen bonding between the surface Pb_I defects and the ammonium group of PEAI.

Figure 2.2C and 2.2D show the positron annihilation spectroscopy (PAS) results of the as prepared films. PAS utilizes positively charged positrons to annihilate negatively charged/neutral defects in semiconductor films (that emit gamma-ray), and by controlling the kinetic energy of the incident positron beam, a depth-dependent gamma-ray annihilation spectrum (where a stronger gamma-ray signal from positron annihilation could derive a larger shape parameter, indicating a higher density of negatively charged/neutral defects) could be extracted. Interestingly, the fluoride treatment did not affect the annihilation spectrum, indicating the F⁻ did not form traps, and its

22

passivation effect was mostly achieved by suppressing the positively charged defects, such as V_I. However, PEAI treatment effectively lowered the shape parameter, especially in the low kinetic energy region, indicating its successful passivation of negative/neutral defects, especially in the surface region. Again, when the fluoride was incoporated together with PEAI, the PAS results did not experience further changes, which suggests that the improved defect passivation effect from PEAI was not because the fluoride increased the density of defect passivated, but because of the enhanced interaction between the existing PEAI and the defects it was passivating.

2.3 Solar cell device characterizations

Semitransparent perovskite solar cells were fabricated with an inverted device configuration shown in Supplementary Figure C2.6. The *J-V* curves (illuminated from the home-deposited ITO/MgF$_2$ side), as well as the solar cell parameters of the control and the target devices, are provided in Figure 2.3A. The champion target device demonstrated a PCE of 17.7% with a V_{OC} of 1.17 V and fill factor (FF) of 81%. This is an improvement from the 1.13 V and 75% of the control device as a result of the effective surface passivation of perovskite and improved energy level alignment between the perovskite and the electron transport layer. J_{SC} was slightly increased, potentially due to the suppressed non-radiative recombination at the surface as well. We note that, to the best of our knowledge, this is one of the highest V_{OC} reported for state-of-the-art semitransparent perovskite PVs, which are usually under inadequate light absorption near band edge, compared with opaque devices. The Steady-state Power Output (SPO, Figure 2.3B) efficiency was also obtained by measuring the photocurrent under constant biases, in which both showed stable SPO performances. Power conversion efficiencies of 20 devices for each of the target and control groups (Supplementary Figure C2.7) was measured. The average efficiency of the target devices was enhanced by 1.5% over the control devices. The photovoltaic parameters for

devices with only F or PEAI treatment are provided in Supplementary Table B2.2. It is notable that PEAI alone effectively increased only the V_{OC}, while both V_{OC} and FF were improved with the target F-PEAI treatment. The external quantum efficiency (EQE) and transmittance spectra of the semitransparent perovskite cells were also measured (Figure 2.3C), which showed approximately 92% peak transmission at the infrared region, which is ideal for tandem applications. Opaque perovskite cells with the target treatment were fabricated by replacing the ITO layer with silver but retaining the ZnO layer to minimize the modified variables. The inverted opaque device, shown in Figure 2.3D (and B2.8), exhibited a V_{OC} of 1.20 V with a PCE of over 21%.

To demonstrate that our semitransparent perovskite cells can be appropriately integrated with commercial PVs for multi-junction tandem applications, we first measured the ambient stability (room temperature, in dark) of the semitransparent perovskite cells. Compared with opaque perovskite solar cells with silver contacts, our semitransparent devices demonstrated far superior ambient stability presented in Figure 2.3e owing to the following intrinsic advantages: (1) silver was replaced with ITO, and the risk of its migration and the consequent degradation of the perovskite[16,17] is mitigated; (2) the sputtered ITO layer was rather compact and rigid compared with conventional metal electrodes[18]; (3) the MgF_2 anti-reflection coating served as a self-encapsulation layer[19], making future commercial lamination and encapsulation processes easier. Since the surface defects, which would have otherwise acted as degradation initiation points, have been effectively passivated, the semitransparent solar cells showed negligible efficiency loss after ~1000 h without further encapsulation. After the first 1128 h of ambient stability test, we carried out an operational stability test for the same batch of devices. With continuous illumination of one-sun, the devices still retained ~87% of the original performance after 500 h.

In addition, we performed further characterizations to verify the conclusions drawn from our device performance results. Admittance spectroscopy (AS) was used to measure the trap density of states (*t*DOS) of the devices, with details provided in Supplementary Text A2.3. Supplementary Figure C2.9 shows that the control device had an overall higher *t*DOS, while the target device exhibited lower density of traps, especially in the deeper trap region (0.3-0.4 eV). Transient photocurrent (TPC) and transient photovoltage (TPV) measurements were carried out to study the charge carrier dynamics in the complete solar cells. Under short circuit condition (TPC, Supplementary Figure C2.10A), the carrier lifetime was shortened from 10.45 µs for the control device to 6.50 µs for the target device, indicating that carriers can be more effectively transported to the external circuit, correlating with the higher fill factor of the target device. Under open circuit condition (TPV, Supplementary Figure C2.10B), where charge carriers are confined within the device, the lifetime was increased from 1.04 ms for the control device to 2.33 ms for the target device, which suggests that charges are less likely to recombine in the target device due to a reduced defect density, consistent with the TRPL and *t*DOS results.

2.4 4-terminal tandem devices based on the passivated perovskite

Lastly, I coupled our high-performance semitransparent target devices with silicon solar cells and CIGS solar cells provided by commercial PV companies Solargiga (China, original efficiency 18.0% c-Si) and Solar Frontier (Japan, original efficiency 20.2%). A four-terminal configuration was adopted to simplify the coupling process and to verify the concept as previously reported for perovskite in tandem applications. The *J-V* curves are shown in Figure 2.4A with silicon and Figure 2.4B with CIGS. The PCEs of the coupled devices were obtained by numerically adding up the efficiency of the target semitransparent perovskite front cell and the efficiencies of the rear cells (with the front cell as an optical filter). The photovoltaic parameters are summarized

in Table 2.1. Due to the absorption and additional reflection of the front cell, the J_{SC} of the rear cells dropped from 38.6 mA/cm^2 to 15.5 mA/cm^2 for silicon, and from 40.3 mA/cm^2 to 16.8 mA/cm^2 for CIGS, respectively. The V_{OC} of the rear cells dropped likewise due to the lower light intensity reaching the rear cells. The FF of the silicon rear cell was improved since the initial shunting due to poor device boundary conditions that were mitigated in the tandem configuration, while the FF for the CIGS rear cell remained similar as the shunting was already adequate from the beginning. The EQE of the separate cells are provided in Figure 2.4C and 2.4D for silicon and CIGS, respectively. The detailed method for determining the EQE of the rear cells established by Brabec's group [20] can be found in Supplementary Text A2.4. Consequently, in the rear cell configuration, the silicon and CIGS cells had efficiencies of 7.4% and 8.1%, respectively. Thus, the overall efficiencies of the four-terminal perovskite-silicon tandem cells reached 25.1% and the perovskite-CIGS tandem cells reached 25.8%, even when both silicon and CIGS cells were commercial products with much lower original efficiencies compared with other reports[7,21,22]. We also demonstrate that if the semitransparent perovskite cells in this work were stacked with the record-performing rear cells reported[23,24], the four-terminal solar cells could yield PCEs of 28.1% and 27.5% for perovskite-silicon and perovskite-CIGS, respectively (Supplementary Table B2.3).

There is an intuitive, but always a neglected fact, that with the same V_{OC} deficiency, solar cells with larger bandgaps theoretically undergo more efficiency losses (in converted power density). We elucidated the correlation between the absorber's bandgap and the voltage loss of a cell (compared with its SQ-limit V_{OC}, see method in Supplementary Text A2.5) to its maximum efficiency loss in Figure 2.4E that quantitatively confirmed it. In other words, higher energy electrons, converted from higher energy photons, are to be output at higher voltages, such that the same V_{OC} gain in the higher bandgap front cell (perovskite) relative to the lower bandgap rear cell

(silicon or CIGS) will gain more PCE. We also noted in Figure 2.4F that the V_{OC} of state-of-the-art semitransparent perovskite front cells (1.17 V in this work, one of the highest values reported) is still far from the 1.38 V SQ-limit V_{OC} (for a 1.66 eV bandgap). Whereas for commercial PVs such as CIGS, the V_{OC} deficiency has been highly suppressed to a value within 0.04 V [25]. It would, thus, be a promising and economic approach to advancing the overall power conversion efficiency by improving the fast-developing perovskite front cell and incorporate it with the haltingly perfecting commercialized PV technologies.

2.5 Conclusion

Overall, the synergistic interaction of the alkali fluoride and PEAI with the perovskite surface was elucidated in this study. The synergy between the fluoride and PEAI was investigated at an atomic scale with a combination of theoretical and experimental approach. The existence of the fluoride effectively enhanced the interaction between the ammonium group of the PEA ligand and the surface defects of the perovskite, leading to more effective passivation effect thus suppressed non-radiative recombination of the film. The energy band alignment at the perovskite surface was also modulated for more efficient charge extraction with the synergistic interaction. Based on this synergetic surface passivation strategy, we delivered a high-performance WBG semitransparent perovskite with a record V_{OC} of 1.17 V, readily suitable for use in stacked tandem PVs. The target cell was coupled with commercial silicon and CIGS solar cells with original efficiencies of 18.0% and 20.2%, respectively, to demonstrate that even with commercial products, the tandem solar cells can still reach efficiencies of over 25% using our strategy (28.1% if the record silicon cell was available).

2.6 References

[1]   T. Leijtens, K. A. Bush, R. Prasanna, M. D. McGehee, *Nat. Energy* **2018**, *3*, 828.

[2]   J. Tong, Z. Song, D. H. Kim, X. Chen, C. Chen, A. F. Palmstrom, P. F. Ndione, M. O. Reese, S. P. Dunfield, O. G. Reid, J. Liu, F. Zhang, S. P. Harvey, Z. Li, S. T. Christensen, G. Teeter, D. Zhao, M. M. Al-Jassim, M. F. A. M. van Hest, M. C. Beard, S. E. Shaheen, J. J. Berry, Y. Yan, K. Zhu, *Science.* **2019**, *364*, 475 LP.

[3]   K. Xiao, R. Lin, Q. Han, Y. Hou, Z. Qin, H. T. Nguyen, J. Wen, M. Wei, V. Yeddu, M. I. Saidaminov, Y. Gao, X. Luo, Y. Wang, H. Gao, C. Zhang, J. Xu, J. Zhu, E. H. Sargent, H. Tan, *Nat. Energy* **2020**.

[4]   D. Kim, H. J. Jung, I. J. Park, B. W. Larson, S. P. Dunfield, C. Xiao, J. Kim, J. Tong, P. Boonmongkolras, S. G. Ji, F. Zhang, S. R. Pae, M. Kim, S. B. Kang, V. Dravid, J. J. Berry, J. Y. Kim, K. Zhu, D. H. Kim, B. Shin, *Science.* **2020**, eaba3433.

[5]   Y. Hou, E. Aydin, M. De Bastiani, C. Xiao, F. H. Isikgor, D.-J. Xue, B. Chen, H. Chen, B. Bahrami, A. H. Chowdhury, A. Johnston, S.-W. Baek, Z. Huang, M. Wei, Y. Dong, J. Troughton, R. Jalmood, A. J. Mirabelli, T. G. Allen, E. Van Kerschaver, M. I. Saidaminov, D. Baran, Q. Qiao, K. Zhu, S. De Wolf, E. H. Sargent, *Science.* **2020**, *367*, 1135 LP.

[6]   A. Al-Ashouri, A. Magomedov, M. Roß, M. Jošt, M. Talaikis, G. Chistiakova, T. Bertram, J. A. Márquez, E. Köhnen, E. Kasparavičius, S. Levcenco, L. Gil-Escrig, C. J. Hages, R. Schlatmann, B. Rech, T. Malinauskas, T. Unold, C. A. Kaufmann, L. Korte, G. Niaura, V. Getautis, S. Albrecht, *Energy Environ. Sci.* **2019**, *12*, 3356.

[7]   D. H. Kim, C. P. Muzzillo, J. Tong, A. F. Palmstrom, B. W. Larson, C. Choi, S. P. Harvey, S. Glynn, J. B. Whitaker, F. Zhang, Z. Li, H. Lu, M. F. A. M. van Hest, J. J. Berry, L. M. Mansfield, Y. Huang, Y. Yan, K. Zhu, *Joule* **2019**, *3*, 1734.

[8]   Q. Han, Y.-T. Hsieh, L. Meng, J.-L. Wu, P. Sun, E.-P. Yao, S.-Y. Chang, S.-H. Bae, T. Kato, V. Bermudez, Y. Yang, *Science.* **2018**, *361*, 904 LP.

[9]   J. Xu, C. C. Boyd, Z. J. Yu, A. F. Palmstrom, D. J. Witter, B. W. Larson, R. M. France, J. Werner, S. P. Harvey, E. J. Wolf, W. Weigand, S. Manzoor, M. F. A. M. van Hest, J. J. Berry, J. M. Luther, Z. C. Holman, M. D. McGehee, *Science.* **2020**, *367*, 1097 LP.

[10]   B. R.-C. E. Chart, *https://www.nrel.gov/pv/cell-efficiency.html* **2021**.

[11]   Y. Rong, Y. Hu, A. Mei, H. Tan, M. I. Saidaminov, S. Il Seok, M. D. McGehee, E. H. Sargent, H. Han, *Science.* **2018**, *361*, eaat8235.

[12]   T.-H. Han, S. Tan, J. Xue, L. Meng, J.-W. Lee, Y. Yang, *Adv. Mater.* **2019**, *31*, 1803515.

[13]   B. Chen, P. N. Rudd, S. Yang, Y. Yuan, J. Huang, *Chem. Soc. Rev.* **2019**, *48*, 3842.

[14]   D. Luo, W. Yang, Z. Wang, A. Sadhanala, Q. Hu, R. Su, R. Shivanna, G. F. Trindade, J. F. Watts, Z. Xu, T. Liu, K. Chen, F. Ye, P. Wu, L. Zhao, J. Wu, Y. Tu, Y. Zhang, X. Yang, W. Zhang, R. H. Friend, Q. Gong, H. J. Snaith, R. Zhu, *Science.* **2018**, *360*, 1442 LP.

[15]   R. Wang, J. Xue, K.-L. Wang, Z.-K. Wang, Y. Luo, D. Fenning, G. Xu, S. Nuryyeva, T. Huang, Y. Zhao, J. L. Yang, J. Zhu, M. Wang, S. Tan, I. Yavuz, K. N. Houk, Y. Yang, *Science.* **2019**, *366*, 1509 LP.

[16]   J. Li, Q. Dong, N. Li, L. Wang, *Adv. Energy Mater.* **2017**, *7*, 1602922.

[17]   Y. Kato, L. K. Ono, M. V Lee, S. Wang, S. R. Raga, Y. Qi, *Adv. Mater. Interfaces* **2015**, *2*, 1500195.

[18]   K. A. Bush, C. D. Bailie, Y. Chen, A. R. Bowring, W. Wang, W. Ma, T. Leijtens, F. Moghadam, M. D. McGehee, *Adv. Mater.* **2016**, *28*, 3937.

[19]   M. Ghoshani, A. Behjat, F. Jafari, N. torabi, *ijop* **2013**, *7*, 11.

[20]   T. Kirchartz, S. Korgitzsch, J. Hüpkes, C. O. R. Quiroz, C. J. Brabec, *ACS Energy Lett.* **2018**, *3*, 1861.

[21]   Z. Wang, X. Zhu, S. Zuo, M. Chen, C. Zhang, C. Wang, X. Ren, Z. Yang, Z. Liu, X. Xu, Q. Chang, S. Yang, F. Meng, Z. Liu, N. Yuan, J. Ding, S. (Frank) Liu, D. Yang, *Adv. Funct. Mater.* **2020**, *30*, 1908298.

[22]   S. Gharibzadeh, I. M. Hossain, P. Fassl, B. A. Nejand, T. Abzieher, M. Schultes, E. Ahlswede, P.

Jackson, M. Powalla, S. Schäfer, M. Rienäcker, T. Wietler, R. Peibst, U. Lemmer, B. S. Richards, U. W. Paetzold, *Adv. Funct. Mater.* **2020**, *30*, 1909919.

[23]   M. A. Green, E. D. Dunlop, D. H. Levi, J. Hohl-Ebinger, M. Yoshita, A. W. Y. Ho-Baillie, *Prog. Photovoltaics Res. Appl.* **2019**, *27*, 565.

[24]   K. Yoshikawa, H. Kawasaki, W. Yoshida, T. Irie, K. Konishi, K. Nakano, T. Uto, D. Adachi, M. Kanematsu, H. Uzu, K. Yamamoto, *Nat. Energy* **2017**, *2*, 17032.

[25]   T. Kato, *Jpn. J. Appl. Phys.* **2017**, *56*, 04CA02.

[26]   S. Tan, I. Yavuz, M. H. Weber, T. Huang, C.-H. Chen, R. Wang, H.-C. Wang, J. H. Ko, S. Nuryyeva, J. Xue, Y. Zhao, K.-H. Wei, J.-W. Lee, Y. Yang, *Joule* **2020**, *4*, 2426.
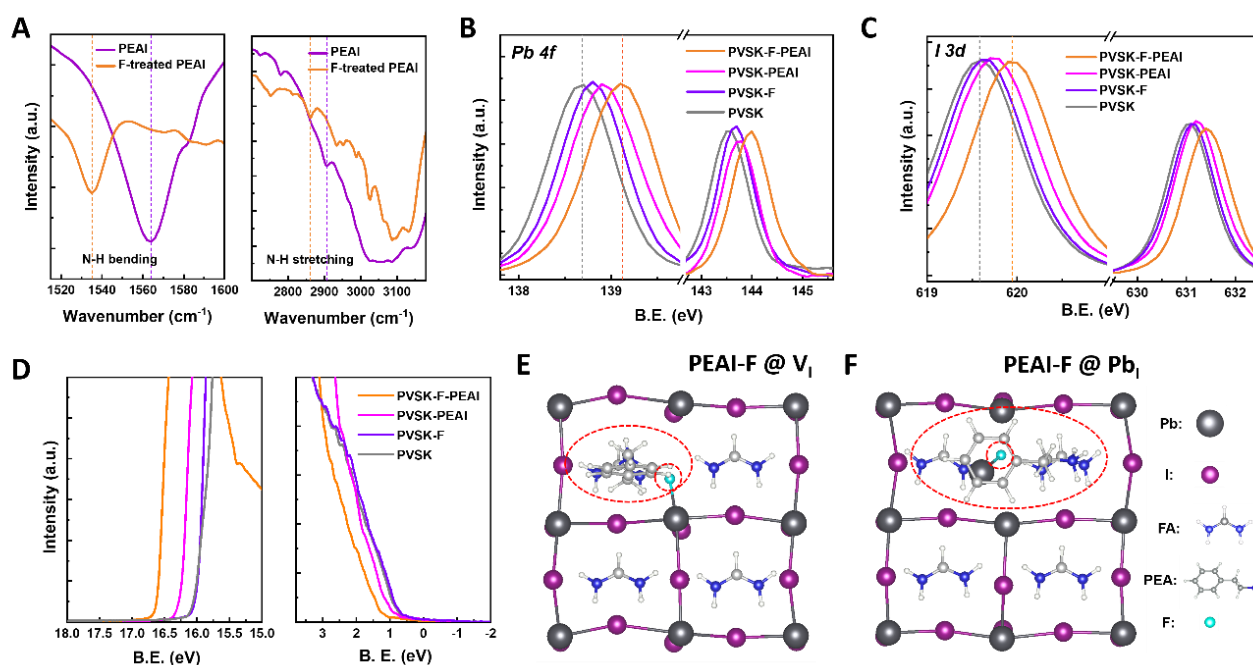
Figure 2.1 Characterizations and calculations of the perovskite surface passivation synergy. (A) FTIR spectra of PEAI and fluoride-PEAI mixture in the range of bending (left) and stretching (right) mode of N-H group. XPS data for Pb *4f* 7/2 and Pb *4f* 5/2 core level spectra (B), and I *3d* 5/2 and I *3d* 3/2 core level spectra (C) from perovskite films with various treatments. (D) UPS spectra of perovskite films with the treatments. Top view of the optimized configuration of the PEAI-F incorporated surface with I vacancy defect (E) and with Pb-I anti-site defect (F). The Pb, I, FA, PEA and F atoms are as depicted in the figure.
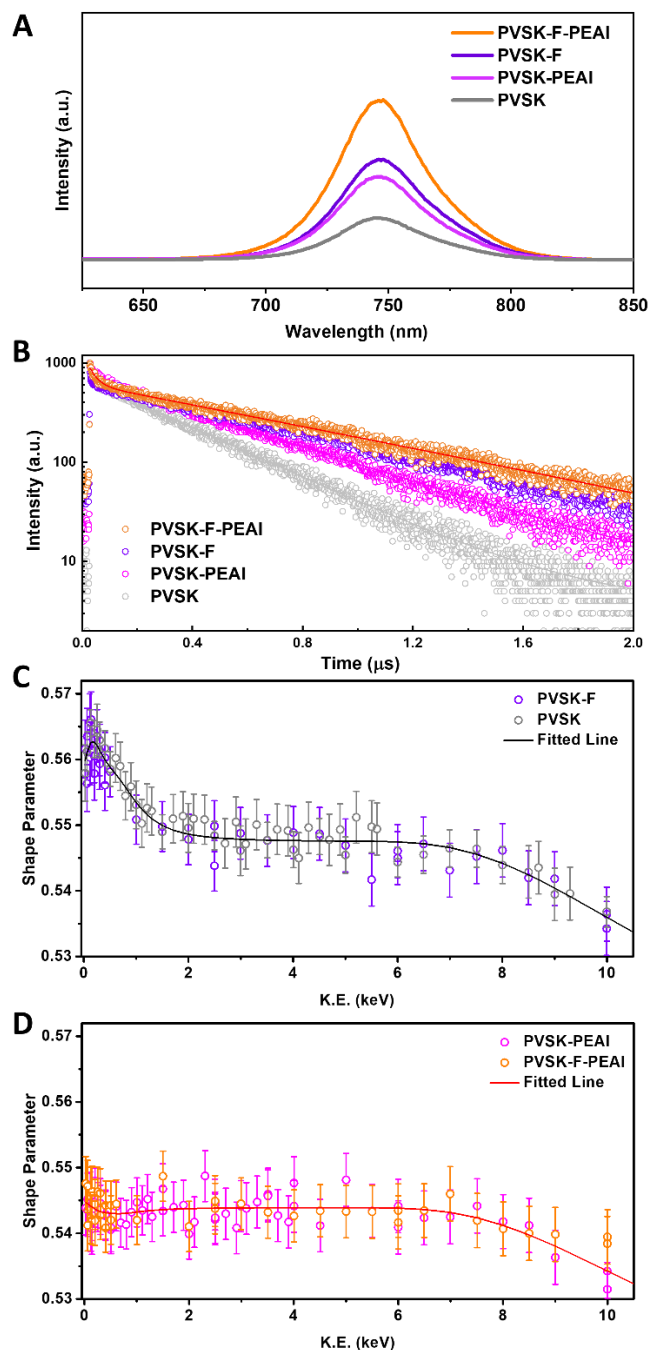
Figure 2.2 Charge carrier dynamics and defect physics characterizations. (A) Photoluminescence and (B) time-resolved photoluminescence of the perovskite films passivated with various treatments. Kinetic energy dependent shape parameters extracted from PAS test for (C) the control and fluoride-treated perovskite films, as well as (D) the PEAI-treated and the target film with both treatments.

Figure 2.3 Measurements and characterizations of the wide-band-gap perovskite cells. (A) J-V curves and (B) SPO profiles of the semitransparent perovskite cells with the targeted synergistic passivation treatment (target) and without any treatment (control). (C) EQE and transmittance spectra of the target cell. (E) J-V curves of the opaque perovskite cell with the target treatment. (E) PCE evolution of the target semitransparent cells without any encapsulation. First 1128 h was measured as ambient stability stored in dark, and the following 500 h was measured as operational stability kept under continuous illumination (90 ± 10 mW cm^{-2}), both under open-circuit condition.

Figure 2.4 Measurement and estimation results for the tandem solar cells. (A and B) J-V curves, (C and D) EQE spectra by combining the target semitransparent perovskite with commercially available silicon (blue) and CIGS (green) solar cells. The semitransparent perovskite cells without splitting into mini cells were used as an optical filter to measure the filtered characteristics of the rear cells. (E) An estimation for the efficiency loss for different bandgap materials with different V_{OC} losses. (F) The estimated PCE for tandem cells when the subcells' V_{OC} varies. The bandgaps of the front and the rear cells were assumed to be 1.64 eV and 1.03 eV, respectively.

Table 2.1 PV parameters of single- and multi-junction solar cells

	V_{OC} (V)	J_{SC} (mA/cm^2)	$J_{SC, EQE}$ (mA/cm^2)	FF (%)	Eff. (%)
ST-Perovskite	1.17	18.6	18.5	81.1	17.7
Silicon	0.66	38.6	38.0	70.3	18.0
Silicon (filtered)	0.65	15.5	15.2	73.7	7.4
CIGS	0.69	40.3	39.8	74.8	20.2
CIGS (filtered)	0.64	16.8	16.7	75.4	8.1
Perovskite-Silicon	---				25.1
Perovskite-CIGS	---				25.8
Perovskite-Silicon[a]	**---**				**28.1**
Perovskite-CIGS[a]	**---**				**27.5**

[a] Data calculated by coupling our semitransparent perovskite cells with the record-performing silicon and CIGS as rear cells.

Chapter 3 Surface Reconstruction of Halide Perovskites during Post-treatment

The record performance of single-junction halide perovskite solar cells (PSCs) has exceeded 25 %.[1] Important breakthroughs on defect passivation strategies have contributed to the rapid performance improvements in recent years.[2,3] However, achievable voltage losses are still short of the theoretical limit. More importantly, it has become apparent that the migration and redistribution of charged point defects by a potential gradient is known to underly the operational instability of PSCs,[4–6] and this remains one of the major challenges of perovskite photovoltaics.

It has been reported that defect states causing non-radiative losses are dominantly located towards the top surface of halide perovskites.[7,8] This has motivated the development of surface passivation strategies by post-treatment of the perovskite surface.[9] However, understanding of the complex reconstruction processes that can occur during the surface treatment procedures and any resulting changes to the interfacial charge dynamics are still lacking. This is urgently needed for targeted surface treatment strategies to minimize trial-and-error approaches. For this purpose, in situ spectroscopy is suited to monitor occurring changes on relevant time and length scales.[10–13]

In this study, we investigate the mechanistic reconstruction processes occurring at the perovskite surface during post-fabrication treatments. We combined complementary surface-sensitive techniques to observe the generation of defects and a reconstruction towards a more PbI_2-rich surface as isopropyl alcohol (IPA) is spun onto the perovskite. We show that this reconstruction has important implications on the thermodynamics and energetics of the perovskite surface. Importantly, our observations suggest that IPA assists in the anchoring process of organic ammonium salts to the perovskite surface.

3.1 In-situ monitoring the surface evolution

IPA is ubiquitously used as the solvent to dissolve organic ammoniums for surface treatments, but formamidinium iodide (FAI), itself with the amidinium functional group, is also soluble in IPA. It is unclear what effects (if any) IPA has on the perovskite surface, given the short exposure timescales (~ms) at high rotation speeds (>4000 rpm). Conflicting results on the macroscopic bulk device/film properties have been reported. Beneficial improvements to film crystallinity, charge carrier dynamics, morphology, and device performance have been observed,[14,15] while detrimental effects to device stability were also reported.[16] To rationalize these contradictory results, we first attempted to explore the microscale phenomena occurring at the surface. Significantly, IPA remains perhaps a crucial solvent for post-treatment, since the most common surface passivating agents, such as phenylethylammonium iodide (PEAI) and octylammonium iodide (OAI), are essentially insoluble in low polarity solvents such as chloroform (CF) (Supplementary Figure C3.1).

The control perovskite is based on a $FAPbI_3$ composition with 5 mol% of added $MAPbBr_3$. We monitored the photoluminescence (PL) of an as-fabricated perovskite film in situ with a 405 nm excitation wavelength (Figure 3.1a) in a nitrogen glovebox (<0.5 ppm O_2/H_2O). The laser penetration depth was estimated to be ~50 nm (Supplementary Figure C3.2), and therefore sensitive to any potential changes in the surface charge carrier recombination behavior. The PL intensity abruptly decreased with a broadening and redshifting of the PL peak upon dropping IPA (Figure 1b, 1c, Supplementary Figure C3.3a). In general, this is indicative of increased nonradiative carrier recombination, which implies the generation of charge-trapping defect states. Time-resolved PL (Supplementary Figure C3.3b) of the perovskite films further support this, where the carrier lifetime decreased from 1,021 to 793 ns for the control and treated films, respectively. The PL

intensity is observed to gradually recover with time, possibly due to trap-filling by photo-generated carriers,[17] as also seen in the control film without treatment (Supplementary Figure C3.3c, d).

3.2 Defect physics model in post-treated films

We further investigated the distribution and nature of the generated defects using Positron Annihilation Spectroscopy (PAS). Positrons are implanted from the film surface and annihilate with electrons after trapping at negatively charged (or neutral) defects to emit two gamma photons. The incident kinetic energy is controlled to vary the positron implantation depth (Figure 3.1d, Supplementary Figure C3.4), from which the depth-resolved defect density of the film can be investigated. The treated film had a higher Shape parameter within ~40 nm from the film surface, implying the generation of negatively charged (or neutral) defects at the top surface region. We speculate that the formed defect is possibly FA vacancy (V_{FA}'), given the solubility of FAI in IPA.

The implied existence of V_{FA}' suggests that iodine vacancy ($V_I^{\bullet}$) was likely generated concurrently, but PAS is unable to ascertain this due to its insensitivity to positively charged defects (i.e. $V_I^{\bullet}$).[18,19] We therefore further probed the films with high-resolution X-ray Photoelectron Spectroscopy (XPS), with an estimated penetration depth 5–10 nm. The I:Pb ratio, calculated from the integrated areas of the Pb 4f doublet and I $3d_{5/2}$ peak (Figure 2a), was 2.45 for the control film, and decreased to 2.04 for the treated film to approach that of stoichiometric PbI_2. We note that the ultra-high vacuum environment of the XPS instrument (~10^{-7}–10^{-8} torr) may have accelerated the outgassing of the volatile halide,[20,21] and therefore only relative comparisons would be reliable. Closer inspection of the XPS spectra further showed that the Pb $4f_{5/2}$ (143.19 eV to 143.13 eV), Pb $4f_{7/2}$ (138.32 eV to 138.25 eV), and I $3d_{5/2}$ (619.15 eV to 619.08 eV) characteristic peaks shifted to lower binding energies for the treated film when compared to the control, suggesting a change in the surface chemical environment. Together with the observed change in the

I:Pb ratios, the shift direction and final peak positions are consistent with the formation of PbI_2 for the treated film.[22] The existence of PbI_2 was directly detected by Grazing Incidence X-ray Diffraction (XRD) at an incident angle of $\omega = 0.2°$ (penetration depth ~60 nm, see Methods) (Figure 3.2c, 3.2d). Moreover, the PbI_2:$FAPbI_3$ peak intensity ratio was observed to decrease at an incident angle of $\omega = 1.0°$ (penetration depth ~310 nm), suggesting that the PbI_2 is located more towards the top perovskite region. Combining the experimental observations together, we thus propose the following reconstruction of the perovskite film surface during post-treatment, by a dissolution reaction process induced by IPA:

$$FAPbI_3\ (s) \xrightarrow{\text{IPA}} FAI\ (in\ IPA) + PbI_2\ (s) + V'_{FA} + V_I^{\bullet}$$

We now discuss some possible implications of this inferred surface reconstruction. Ultraviolet Photoelectron Spectroscopy (UPS), with a penetration depth 2–5 nm, was used to investigate any band structure changes at the surface. The fermi level was observed to downshift from -4.68 eV for the control film to -4.77 eV for the film treated with IPA (Figure 3.2b), indicating a more p-doped surface for the latter relative to the bare perovskite surface. The overall band structure of the treated surface further downshifted relative to the vacuum level due to the deeper valence band maximum (inset of Figure 3.2b), consistent with a relatively more FAI deficient surface.[23] This possibly creates a beneficial band bending going from the perovskite bulk to the surface contacting a hole-transporting material (Supplementary Figure C3.5a). The surface PbI_2 for the treated film might also contribute to interfacial passivation.[24] In reality, however, we observed that the treated device performance was inferior to the control with a more pronounced current-voltage hysteresis (Supplementary Figure C3.5b, c), likely due to the generated vacancy defects, given that defect migration (due to the bias potential) is known to underly the hysteric behavior.[4]

38

3.3 DFT calculation for the reconstructed surface

First-principles density functional theory (DFT) calculations were performed on slabs based on the deduced reconstruction to compare their thermodynamics and energetics. We note that realistically, the perovskite surface is expected to be a complex amalgamation of exposed atoms, local atomic pairing/reorientation, and defected.[25] However, simplified slab models are necessarily required to reduce computational complexity. Nevertheless, *relative* comparisons can be made based on the predicted results. Experimental investigations have observed that the pristine perovskite surface (without treatment) is terminated mostly by organic halides,[26,27] which is also supported by computational results.[28] Our results imply that IPA reconstructs the surface towards a *relatively more* PbI$_2$-rich surface. Therefore, we chose the two extreme cases of complete FAI termination (Figure 3.3a) and PbI$_2$ termination (Figure 3.3b) to model the pristine (control) and reconstructed (treated) surfaces, respectively, again noting that the slabs are used to predict *relative trends*.

The predicted bandgap decreased while the ionization energy increased for the PbI$_2$ termination surface (Figure 3.3c), matching the in situ PL and UPS observations. The surface energy more than doubled for the PbI$_2$ termination surface, indicating that the surface became more thermodynamically unstable with treatment. This likely contributed to the observed aggravated instability of the treated films (Supplementary Figure C3.6). The generated defects might additionally lower the FAPbI$_3$ cubic-to-hexagonal phase transformation activation energy barrier to also accelerate the degradation.[29] Given the increased surface energy, we postulated that ammonium salts may preferentially adsorb onto the treated surface. We further calculated the formation enthalpy to attach either OAI or PEAI to the surfaces (Figure 3.3d). The adsorption enthalpies for both were significantly more negative on the PbI$_2$ termination surface – for OAI, -

0.78 versus -1.88 eV (141% increase), and -0.9 versus -3.75 eV for PEAI (317% increase), suggesting that the surface reconstruction plays a vital role in the passivation process.

3.4 Perovskite film and devices with modified post-treatment strategy

The theoretical calculations imply that ammonium salts are thermodynamically more favored to adsorb onto the treated surface. We investigated this with a modified 2-step surface post-treatment process (Supplementary Figure C3.7). Initially treating a perovskite film with pure IPA before subsequently depositing octylammonium bromide (OABr) in CF (at the same concentration) further improved the device performance (Figure 3.3e). The champion device surface treated with the modified 2-step approach reached a power conversion efficiency of 22.9 % in reverse bias (Figure 3.3e) with negligible current-voltage hysteresis, relative to the 22.4 % of the conventionally treated device. The improved performance was attributed to increases in the device open-circuit voltage (1.129 V to 1.146 V) and fill factor (79.1 % to 79.6 %), which is indicative of an enhanced defect passivation effect with the modified 2-step treatment. Therefore, the observations support the theoretical predictions that IPA assists in the adsorption process of ammonium salts to the surface and thus the passivation of defects. The surface is first reconstructed by removing FAI to expose the undercoordinated Pb^{2+} (i.e. $V_I^{\bullet}$) for the ammonium groups to bond with by electrostatic coulomb interactions and/or hydrogen bonding.

We speculated that the PL evolution as OAI or PEAI (in IPA) is deposited on the surface may be related to their adsorption enthalpies. Further measurements show that although both treatments led to instantaneous PL enhancements immediately upon deposition (Figure 3f, 3g, Supplementary Figure C3.8), the PL intensity subsequently decayed ~10 s after deposition for the OAI treated film. With the PbI_2 termination surface, the computed adsorption enthalpies imply a significantly weaker interaction of OAI (relative to PEAI) with the perovskite surface, which may

40

possibly be correlated with the differing PL dynamics. On the other hand, the adsorption enthalpies are negligibly different when calculated using the FAI termination surface, which may be challenging to reconcile with the experimental observations. We also monitored the recombination dynamics with further in situ PL measurements during annealing (Supplementary Figure C3.9a, b). A rapid initial exponential decay in PL intensity was observed for both films due to increased phonon scattering at elevated temperatures.[10,12] However, only the OAI treated film counteracted the initial drop to eventually increase its PL intensity due to the activated defect passivation effect. The evolution and emission characteristics of the wide bandgap phases notably differ between the OAI and PEAI treated films, and will be the subject of future investigations (Supplementary Figure C3.9c, d, e).

3.5 Conclusion

In summary, a reconstruction of the perovskite top surface induced by IPA was observed, which is ubiquitously used as the solvent for surface treatment with organic ammonium salts. We discussed several implications of this reconstruction on the perovskite surface energetics and thermodynamics. Importantly, given the profound differences between the reconstructed surface and the perovskite bulk/pristine surface, these results will guide further experimental and theoretical investigations of the perovskite surface and surface passivation strategies.

3.6 References

(1) National Renewable Energy Laboratory. *Best Research-Cell*

Efficiencies.   https://www.nrel.gov/pv/assets/pdfs/best-research-cell-efficiencies.20200104.pdf (accessed 04/16/2021).

(2) Jiang, Q.; Zhao, Y.; Zhang, X.; Yang, X.; Chen, Y.; Chu, Z.; Ye, Q.; Li, X.; Yin, Z.; You, J. Surface Passivation of Perovskite Film for Efficient Solar Cells. Nat. Photonics 2019, 13 (7), 460–466. https://doi.org/10.1038/s41566-019-0398-2.

(3) Kim, G.; Min, H.; Lee, K. S.; Lee, D. Y.; Yoon, S. M.; Seok, S. Il. Impact of Strain Relaxation on Performance of α-Formamidinium Lead Iodide Perovskite Solar Cells. Science 2020, 370 (6512), 108–112. https://doi.org/10.1126/science.abc4417.

(4) Tan, S.; Yavuz, I.; De Marco, N.; Huang, T.; Lee, S.; Choi, C. S.; Wang, M.; Nuryyeva, S.; Wang, R.; Zhao, Y.; Wang, H.-C.; Han, T.-H.; Dunn, B.; Huang, Y.; Lee, J.-W.; Yang, Y. Steric Impediment of Ion Migration Contributes to Improved Operational Stability of Perovskite Solar Cells. Adv. Mater. 2020, 32 (11), 1906995. https://doi.org/10.1002/adma.201906995.

(5) Ball, J. M.; Petrozza, A. Defects in Perovskite-Halides and Their Effects in Solar Cells. Nat. Energy 2016, 1 (16149), 1–13. https://doi.org/10.1038/nenergy.2016.149.

(6) Lee, J.-W.; Kim, S.-G.; Yang, J.-M.; Yang, Y.; Park, N.-G. Verification and Mitigation of Ion Migration in Perovskite Solar Cells. APL Mater. 2019, 7 (041111), 1–12. https://doi.org/10.1063/1.5085643.

(7) Ni, Z.; Bao, C.; Liu, Y.; Jiang, Q.; Wu, W.-Q.; Chen, S.; Dai, X.; Chen, B.; Hartweg, B.; Yu, Z.; Holman, Z.; Huang, J. Resolving Spatial and Energetic Distributions of Trap States in Metal Halide Perovskite Solar Cells. Science 2020, 367 (6484), 1352–1358. https://doi.org/10.1126/science.aba0893.

(8) Yang, Y.; Yang, M.; Moore, D. T.; Yan, Y.; Miller, E. M.; Zhu, K.; Beard, M. C. Top and Bottom Surfaces Limit Carrier Lifetime in Lead Iodide Perovskite Films. Nat. Energy 2017, 2 (2), 16207. https://doi.org/10.1038/nenergy.2016.207.

(9) Han, T.-H.; Tan, S.; Xue, J.; Meng, L.; Lee, J.-W.; Yang, Y. Interface and Defect Engineering for Metal Halide Perovskite Optoelectronic Devices. Adv. Mater. 2019, 31 (47), 1803515. https://doi.org/10.1002/adma.201803515.

(10) Babbe, F.; Sutter‐Fella, C. M. Optical Absorption‐Based In Situ Characterization of Halide Perovskites. Adv. Energy Mater. 2020, 10 (26), 1903587. https://doi.org/10.1002/aenm.201903587.

(11) Song, T.-B.; Yuan, Z.; Babbe, F.; Nenon, D. P.; Aydin, E.; De Wolf, S.; Sutter-Fella, C. M. Dynamics of Antisolvent Processed Hybrid Metal Halide Perovskites Studied by In Situ Photoluminescence and Its Influence on Optoelectronic Properties. ACS Appl. Energy Mater. 2020, 3 (3), 2386–2393. https://doi.org/10.1021/acsaem.9b02052.

(12) Song, T.; Yuan, Z.; Mori, M.; Motiwala, F.; Segev, G.; Masquelier, E.; Stan, C. V.; Slack, J. L.; Tamura, N.; Sutter‐Fella, C. M. Revealing the Dynamics of Hybrid Metal Halide Perovskite Formation via Multimodal In Situ Probes. Adv. Funct. Mater. 2020, 30 (6), 1908337. https://doi.org/10.1002/adfm.201908337.

(13) Lee, J.-W.; Tan, S.; Han, T.-H.; Wang, R.; Zhang, L.; Park, C.; Yoon, M.; Choi, C.; Xu, M.; Liao, M. E.; Lee, S.-J.; Nuryyeva, S.; Zhu, C.; Huynh, K.; Goorsky, M. S.; Huang, Y.; Pan, X.; Yang, Y. Solid-Phase Hetero Epitaxial Growth of α-Phase Formamidinium Perovskite. Nat. Commun. 2020, 11 (1), 5514. https://doi.org/10.1038/s41467-020-19237-3.

(14) Prochowicz, D.; Tavakoli, M. M.; Solanki, A.; Goh, T. W.; Pandey, K.; Sum, T. C.; Saliba, M.; Yadav, P. Understanding the Effect of Chlorobenzene and Isopropanol Anti-Solvent Treatments on the Recombination and Interfacial Charge Accumulation in Efficient Planar Perovskite Solar Cells. J. Mater. Chem. A 2018, 6 (29), 14307–14314. https://doi.org/10.1039/c8ta03782e.

(15) Wang, X.; Li, X.; Tang, G.; Zhao, L.; Zhang, W.; Jiu, T.; Fang, J. Improving Efficiency of Planar Hybrid CH3NH3PbI3-XClx Perovskite Solar Cells by Isopropanol Solvent Treatment. Org. Electron. 2015, 24, 205–211. https://doi.org/10.1016/j.orgel.2015.05.043.

(16) Yoo, J. J.; Wieghold, S.; Sponseller, M. C.; Chua, M. R.; Bertram, S. N.; Putri, T.; Tresback, J. S.; Hansen, E. C.; Correa-Baena, J.-P.; Bulović, V.; Buonassisi, T.; Shin, S. S.; Bawendi, M. G. An Interface Stabilized Perovskite Solar Cell with High Stabilized Efficiency and Low Voltage Loss. Energy Environ. Sci. 2019, 12, 2192–2199. https://doi.org/10.1039/c9ee00751b.

(17) DeQuilettes, D. W.; Zhang, W.; Burlakov, V. M.; Graham, D. J.; Leijtens, T.; Osherov, A.; Bulović, V.; Snaith, H. J.; Ginger, D. S.; Stranks, S. D. Photo-Induced Halide Redistribution in Organic–Inorganic Perovskite Film. Nat. Commun. 2016, 7 (11683), 1–9. https://doi.org/10.1038/ncomms11683.

(18) Barthe, M.-F.; Labrim, H.; Gentils, A.; Desgardin, P.; Corbel, C.; Esnouf, S.; Piron, J. P. Positron Annihilation Characteristics in UO2: For Lattice and Vacancy Defects Induced by Electron Irradiation. Phys. Status Solidi C 2007, 10, 3627–3632. https://doi.org/10.1002/pssc.200675752.

(19) Wiktor, J.; Jomard, G.; Torrent, M.; Bertolus, M. First-Principles Calculations of Momentum Distributions of Annihilating Electron–Positron Pairs in Defects in UO2. J. Phys. Condens. Matter 2017, 29 (035503), 1–9. https://doi.org/10.1088/1361-648X/29/3/035503.

(20) Jiang, Y.; Yang, S.-C.; Jeangros, Q.; Pisoni, S.; Moser, T.; Buecheler, S.; Tiwari, A. N.; Fu, F. Mitigation of Vacuum and Illumination-Induced Degradation in Perovskite Solar Cells by Structure Engineering. Joule 2020, 4 (5), 1087–1103. https://doi.org/10.1016/j.joule.2020.03.017.

(21) Das, C.; Wussler, M.; Hellmann, T.; Mayer, T.; Jaegermann, W. In Situ XPS Study of the Surface Chemistry of MAPI Solar Cells under Operating Conditions in Vacuum. Phys. Chem. Chem. Phys. 2018, 20 (25), 17180–17187. https://doi.org/10.1039/C8CP01259H.

(22) Juarez-Perez, E. J.; Ono, L. K.; Maeda, M.; Jiang, Y.; Hawash, Z.; Qi, Y. Photodecomposition and Thermal Decomposition in Methylammonium Halide Lead Perovskites and Inferred Design

Principles to Increase Photovoltaic Device Stability. J. Mater. Chem. A 2018, 6 (20), 9604–9612. https://doi.org/10.1039/C8TA03501F.

(23) Meggiolaro, D.; Mosconi, E.; Proppe, A. H.; Quintero-Bermudez, R.; Kelley, S. O.; Sargent, E. H.; De Angelis, F. Energy Level Tuning at the MAPbI3 Perovskite/Contact Interface Using Chemical Treatment. ACS Energy Lett. 2019, 4 (9), 2181–2184. https://doi.org/10.1021/acsenergylett.9b01584.

(24) Chen, Q.; Zhou, H.; Song, T. Bin; Luo, S.; Hong, Z.; Duan, H. S.; Dou, L.; Liu, Y.; Yang, Y. Controllable Self-Induced Passivation of Hybrid Lead Iodide Perovskites toward High Performance Solar Cells. Nano Lett. 2014, 14 (7), 4158–4163. https://doi.org/10.1021/nl501838y.

(25) Leblebici, S. Y.; Leppert, L.; Li, Y.; Reyes-Lillo, S. E.; Wickenburg, S.; Wong, E.; Lee, J.; Melli, M.; Ziegler, D.; Angell, D. K.; Ogletree, D. F.; Ashby, P. D.; Toma, F. M.; Neaton, J. B.; Sharp, I. D.; Weber-Bargioni, A. Facet-Dependent Photovoltaic Efficiency Variations in Single Grains of Hybrid Halide Perovskite. Nat. Energy 2016, 1 (16093), 1–7. https://doi.org/10.1038/nenergy.2016.93.

(26) She, L.; Liu, M.; Zhong, D. Atomic Structures of CH3NH3PbI3 (001) Surfaces. ACS Nano 2016, 10 (1), 1126–1131. https://doi.org/10.1021/acsnano.5b06420.

(27) Stecker, C.; Liu, K.; Hieulle, J.; Ohmann, R.; Liu, Z.; Ono, L. K.; Wang, G.; Qi, Y. Surface Defect Dynamics in Organic− Inorganic Hybrid Perovskites: From Mechanism to Interfacial Properties. ACS Nano 2019, 13 (10), 12127–12136. https://doi.org/10.1021/acsnano.9b06585.

(28) Geng, W.; Tong, C.-J.; Tang, Z.-K.; Yam, C.; Zhang, Y.-N.; Lau, W.-M.; Liu, L.-M. Effect of Surface Composition on Electronic Properties of Methylammonium Lead Iodide Perovskite. J. Mater. 2015, 1 (3), 213–220. https://doi.org/10.1016/j.jmat.2015.07.005.

(29) Tan, S.; Yavuz, I.; Weber, M. H.; Huang, T.; Chen, C.-H.; Wang, R.; Wang, H.-C.; Ko, J. H.; Nuryyeva, S.; Xue, J.; Zhao, Y.; Wei, K.-H.; Lee, J.-W.; Yang, Y. Shallow Iodine Defects Accelerate the Degradation of α-Phase Formamidinium Perovskite. Joule 2020, 4 (11), 2426–2442. https://doi.org/10.1016/j.joule.2020.08.016.
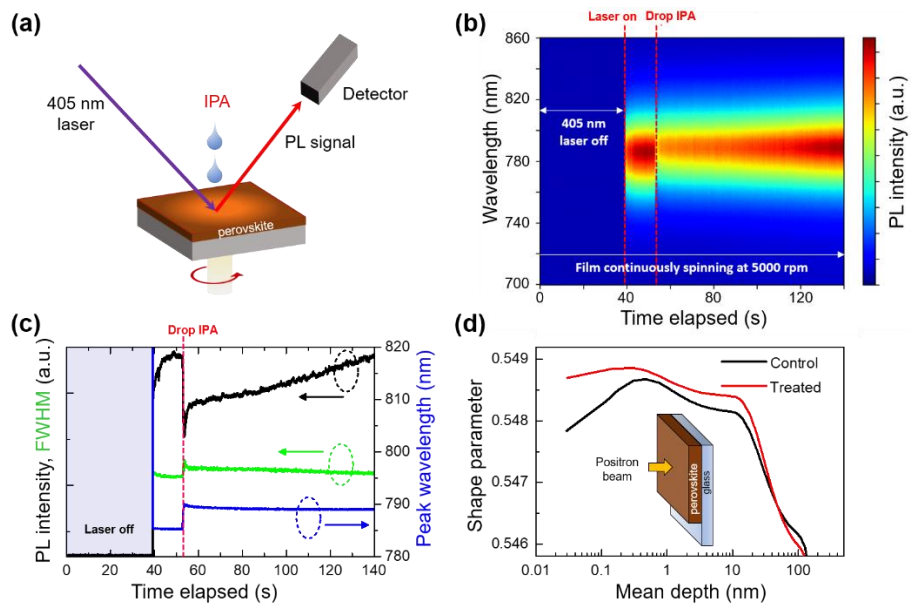
Figure 3.1 Defect generation by IPA treatment. (a) Schematic of the in situ PL measurement during IPA post-treatment. (b) In situ PL contour plot of a perovskite film undergoing surface treatment with IPA dropped at around 53 s. (c) Evolution of the PL parameters extracted from fitting (b). (d) PAS depth-profiling of the perovskite films.
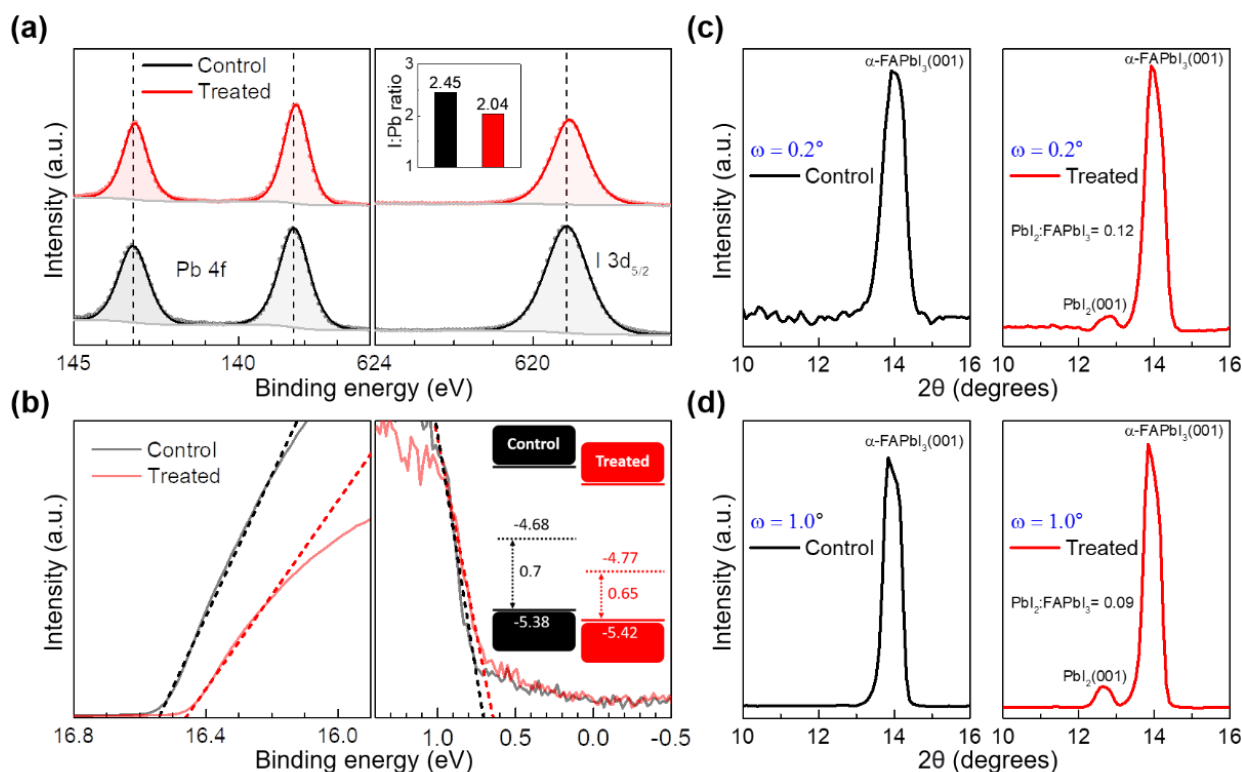
Figure 3.2 Characterizations of the perovskite films. (a) High-resolution XPS spectra of the Pb 4f and I $3d_{5/2}$ peaks of the perovskite films. Inset includes the calculated I:Pb ratios of the films. Solid lines are fitted plots. Dashed vertical lines demarcate the peak positions for the control film. Intensities are normalized to Pb 4f peak. (b) UPS spectra of the perovskite films. Inset includes a schematic band diagram of the energy levels based on the UPS measurements. GIXRD diffraction patterns of the perovskite films measured with an incident angle of (c) $\omega = 0.2°$ or (d) $\omega = 1.0°$.
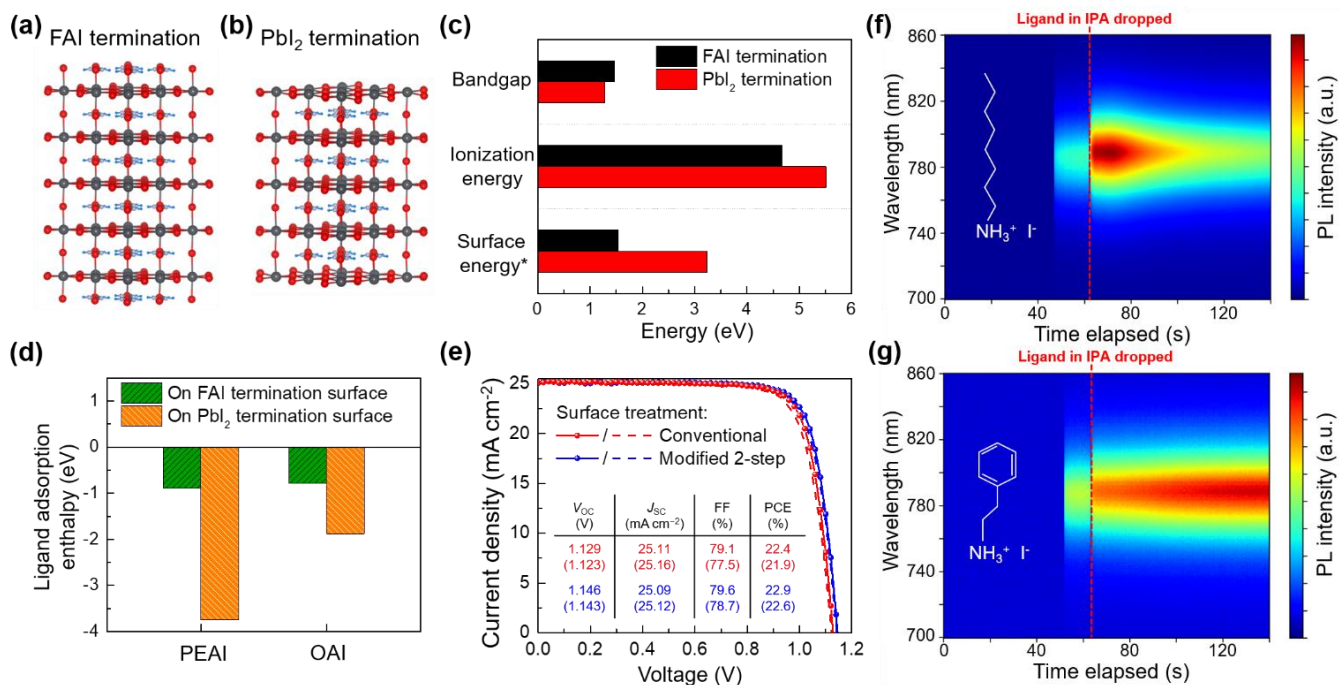
47

Figure 3.3 Surface reconstruction and its implications. (a), (b) Theoretical slab models for first-principles DFT calculations. Atoms are colored black (lead), red (iodine), gray (nitrogen), and blue (hydrogen). (c) Calculated surface physiochemical properties. The asterisk indicates that surface energy is in units of eV nm^{-2}. (d) Enthalpy of adsorption of either PEAI or OAI on the surfaces. (e) Current density-voltage curves of devices treated with 10 mM OABr in CF. Inset includes the measured photovoltaic parameters. Brackets indicate parameters measured in forward bias. In situ PL contour plots of perovskite films undergoing surface treatment with (f) 10 mM OAI or (g) 10 mM PEAI in IPA.

Chapter 4. Performance-Limiting Formation Dynamics in Mixed-Halide Perovskites

Metal halide perovskites with their X-sites of iodine partially substituted with bromine have demonstrated great potential for commercialization of halide perovskite technology for use in tandem photovoltaics (PVs) integrated with conventional PV products such as Si and $CuInGaSe_2$ (CIGS).(*1*) By controlling the I/Br ratio, the optical bandgaps of mixed-halide perovskites can be tuned to be between 1.64-1.70 eV: usually referred to as wide-bandgap (WBG) perovskites in the field, ideal for front-cell applications in two-junction tandem PVs.(*2*) With such WBG mixed-halide perovskites, perovskite-Si and perovskite-CIGS tandem cells have reached remarkable power conversion efficiencies (PCEs) of 29.5% and 24.2%, respectively.(*3*)

Conversely, single-junction PVs based on majority $FAPbI_3$ tri-iodide perovskite compositions ($E_g = 1.48$ eV, $V_{OC, SQ} = 1.21$ V, $V_{OC, reported} = 1.18$ V) have recently exceeded 25% PCE, with voltage deficits, defined as the difference between the optical bandgap and open-circuit voltage (V_{OC}), as low as 0.30 V.(*4*) For WBG mixed-halide perovskites, however, currently even the best reported sub-cell with novel hole transporting materials with negligible energy offsets with the perovskite layer exhibited a voltage deficit up to 0.46 V ($E_g = 1.68$ eV, $V_{OC, SQ} = 1.40$ V, $V_{OC, reported} = 1.22$ V)(*5*). Therefore, the voltage deficits in WBG perovskites continue to significantly lag their corresponding single-junction counterparts. Active debate is ongoing regarding the mechanistic reasons underlying the large voltage deficits in WBG perovskites, which remains an unsolved challenge in the field. Arguably, the voltage deficits remain the largest bottleneck towards further improving the performance of perovskite-based tandem PVs.

Voltage deficits are directly correlated with non-radiative energy losses. Even though halide perovskites are reported to have high defect tolerance,(*6, 7*) deep traps still do exist, especially towards the top surface region(*8*), that may induce trap-mediated recombination losses(*9*). Intrinsic

defects form during the nucleation and growth stages of the perovskite crystals from solution, and their formation is highly dependent on several processing conditions, and especially the precursor stoichiometry and composition. On this note, since the cation itself minimally affects the optical bandgap, ***cation engineering*** has been intensively studied and explored. For example, Lu et al. reported that formulations with Cs^+ dramatically affected the perovskite formation dynamics and processing window,(*10*) which was subsequently found by Fenning et al. to be also essential to achieve homogeneous halide distribution and is critical for highly efficient mixed-halide perovskite PVs.(*11*) These pioneering works have provided many insights of the cations' role in preparing mixed-halide perovskites, and particularly their effects on achieving halide homogeneity and preventing halide-segregation during operation.(*12–15*) However, given that the halide ratio in WBG compositions is mostly preserved to achieve the necessary optical bandgap, ***the role of the anion*** on the perovskite formation dynamics has been largely unexplored. Importantly, the I/Br ratio may potentially alter the nucleation and growth behaviors of WBG perovskites, which may further be related to the defect physics and optoelectronic properties of the films.

In this work, we investigated the role of Br mixing on the formation dynamics of WBG perovskites. Combining systematic experimental studies with first-principle calculations, our observations suggest that the representative $FAMACsPb(I_{0.8}Br_{0.2})_3$ perovskite undergoes a complex crystallization pathway by first nucleating a Br-rich phase from solution during supersaturation, before experiencing a retarded growth stage during perovskite growth. The slow growth stage is associated with a halide homogenization process that brings the lattice composition to the eventual target stoichiometry. This homogenization process inadvertently altered the formation dynamics of mixed-halide perovskites and promoted defect formation, which consequently led to increased non-radiative recombination losses in the final perovskite film. In other words, Br affected the

perovskite formation dynamics, which may have contributed to the large voltage deficits in high Br%-containing compositions.

4.1 Formation dynamics monitoring

We specifically focused on the triple cation mixed-halide WBG perovskite FAMACsPb($I_{0.8}Br_{0.2}$)$_3$, as it is one of the most widely reported compositions with a good resistance against light-induced halide segregation and also high PV performance. The tri-iodide reference with the same triple cations, FAMACsPbI$_3$, will serve as the reference to investigate the effects of Br inclusion on the perovskite formation dynamics. As shown in both the digital photographs (Figure 4.1A) and absorption spectra (Figure 4.1B) of the two perovskites, the as-cast FAMACsPbI$_3$ film already exhibited strong band edge absorption, indicating that the α-phase perovskite has partially formed. In contrast, the as-cast FAMACsPb($I_{0.8}Br_{0.2}$)$_3$ film was more transparent, and showed negligible absorption associated with its perovskite phase near its target bandgap of approximately 1.67 eV (745 nm). After annealing, the band edge absorptions and absorption coefficients for both compositions were similar (but displaced in wavelength), hinting that the formation dynamics *during* crystallization have been altered by the inclusion of Br. We further investigated the films using X-ray diffraction (XRD). Both as-cast films exhibited the α-perovskite (001) peak. Upon annealing, the (001) peak position for FAMACsPb($I_{0.8}Br_{0.2}$)$_3$ underwent a significantly larger shift towards lower 2θ (Figure 4.1C and S1), whereas the peak position for FAMACsPbI$_3$ changed negligibly in comparison. Decreasing Br content in the perovskite lattice would increase the lattice constant (smaller 2θ), and therefore the XRD results perhaps suggest that a Br-rich phase nucleated initially, and the lattice Br ratio is decreasing during the growth stage due to gradual iodide incorporation into the perovskite nuclei during crystallization (the FACs (MA-free) system was also explored in detail, see Supplementary Figure

51

C4.2-4.3). Furthermore, although the cation composition is fixed as a constant for the above discussed perovskite films, we further analyzed the XRD patterns of $MAPb(I_XBr_{1-X})_3$, $FAPb(I_XBr_{1-X})_3$ (with or without MACl additive), $FAMACsPb(I_XBr_{1-X})_3$, and $FACsPb(I_XBr_{1-X})_3$ films to rule out any possible contribution by the cations and the MACl additive (Supplementary Figure C4.5-4.9, detailed discussion in Supplementary Text A4.2), and the observations from these "single cation" as well as the "MACl-free" films were consistent with the triple-cation system with MACl that delivered the champion performance. Therefore, we hypothesized that the initial nucleation was most likely dominated by a Br-rich phase, which is followed by slower iodide incorporation during the growth stage. We also observed that PbI_2 formed more readily in $FAMACsPb(I_{0.8}Br_{0.2})_3$, and the film crystallinity was poorer than $FAMACsPbI_3$ (Supplementary Figure C4.1, detailed discussion in Supplementary Text).

To investigate such a hypothesis, we utilized in-situ PL to monitor the perovskite crystallization process in real-time. In contrast to diffraction methods, in-situ PL provides direct proof of the bandgap evolution during growth, which is dominated mainly by the halide ratio in halide perovskites, and thus, is valuable to probe the formation dynamics related to the halide elements in real time. A 532 nm laser diode, coupled with a visible-range spectrometer, were mounted in a N_2 glove box to track the film photoemission during nucleation and growth. As shown in Figure 4.2A, the experiment was designed to collect the PL signal during the approximately 1 min spin-coating step, followed by annealing at 65 °C for 5 mins. Figure 4.2B and 4.2C depict the PL spectra evolution during the formation of the mixed-halide $FAMACsPb(I_{0.8}Br_{0.2})_3$ and tri-iodide $FAMACsPbI_3$; data displayed on the left initiates from antisolvent dripping during spin coating. Supplementary Figure C4.10 exemplifies the Gaussian fitting of the in-situ PL spectra to extract the PL peak position, intensity, and FWHM, as plotted in

Figure 4.2D-F. It was observed that for both formulations, their respective PL signals initiated at much higher energy levels (1.88 eV for $FAMACsPb(I_{0.8}Br_{0.2})_3$ and 1.67 eV for $FAMACsPbI_3$) compared with the final bandgap of the bulk perovskite films (approximately 1.67 eV and 1.57 eV, respectively, from their PL maxima). For $FAMACsPb(I_{0.8}Br_{0.2})_3$, the energy shifted by 0.115 eV during the spin-coating stage (ΔE_1) and 0.051 eV upon annealing (ΔE_2). The corresponding values were 0.072 eV and 0.011 eV for $FAMACsPbI_3$, much less than the mixed-halide composition. We speculated that the emission peak shifting during the perovskite formation, especially during the early growth period, could be attributed to a combination of two effects: 1. the quantum confinement of the nano-grains, in which case a larger initial crystal size would show smaller energy shifting; 2. a compositional evolution during perovskite formation dominated by an initial higher bandgap species.(*16–18*) Therefore, the larger ΔE in $FAMACsPb(I_{0.8}Br_{0.2})_3$ is most likely due to the formation of an initial Br-rich nuclei, complementing the XRD analysis discussed.

On the other hand, the $FAMACsPbI_3$ film took only ~54 s to reach its *stable emission peak position* during annealing, while for $FAMACsPb(I_{0.8}Br_{0.2})_3$, the emission peak shifting lasted for over 150 s. Therefore, the growth stage has been retarded in $FAMACsPb(I_{0.8}Br_{0.2})_3$, likely associated with an increased activation energy barrier for perovskite growth.(*19*) The emission peak transition during annealing for $FAMACsPb(I_{0.8}Br_{0.2})_3$ underwent two separate stages (denoted as t_1 beginning at 42.3 s, and t_2 beginning at 109.8 s) before its stabilization. We further compared the growth evolution with different amounts of Br incorporation of 20%, 10%, 5%, and 0% (Supplementary Figure C4.11), observing that the growth stage successively retarded further with increasing Br%. The PL intensity (Figure 4.2E) observed during the growth process was a combination of several effects, including the formation of increasing amounts of highly illuminating perovskite-phase crystals, countered by self-absorption as the perovskite amount

increases, especially close to the band edge. As the size and specific area of crystalline perovskite change during growth, trap assisted non-radiative recombination could also play a significant role. Overall, we found that the PL intensity increases during the spin-coating stage, while it continued to increase to a maximum in tens of seconds, then decreases before the signal stabilizes during the annealing stage. We speculate that the formation of illuminating perovskite crystals dominated the PL intensity during spin-coating, while during annealing, the time required to reach the intensity maximum serves as an indicator of the crystal growth rate (i.e. the earlier it reaches the intensity maximum, the faster is the growth rate). For FAMACsPbI$_3$, we observed that the signal quickly "saturated" after 28.1 s upon casting the anti-solvent, while the intensity of FAMACsPb(I$_{0.8}$Br$_{0.2}$)$_3$ continued to increase during spin-coating (Figure 2E left slab). During the annealing stage, these two compositions reached their maximum intensities at 33.5 s and 19.9 s, respectively. Analyzing the full width at half maximum (FWHM, Figure 4.2F), the signal from FAMACsPb(I$_{0.8}$Br$_{0.2}$) achieved a much sharper peak during spin-coating and stabilized significantly slower than that of the FAMACsPbI$_3$. For the fully annealed films shown in Supplementary Figure C4.12, both compositions exhibited clear and mono-peak photoluminescence, indicating that both films eventually reached their target stoichiometry with good phase homogeneity, and matched well with their absorption cutoffs. The bandgaps were determined to be approximately 1.56 eV and 1.67 eV for the as prepared FAMACsPbI$_3$ and FAMACsPb(I$_{0.8}$Br$_{0.2}$)$_3$ films, respectively. This indicates that a *halide homogenization process* must have occurred during the growth stage to achieve the target stoichiometry from the initial Br-rich phase. Such a homogenization process occurs by diffusion of iodide to incorporate into the initial Br-rich phase, which introduces an activation energy barrier and is consistent with a retardation of the perovskite growth.(*20*) We further explored the FACs (MA-free) composition, which has also been reported to be highly resistant to halide segregation

and delivers high PCE. The trends were consistent with the triple-cation system (Supplementary Figure B4.13 and B4.14, detailed discussion see Supplementary Text A4.3), supporting our hypothesis and demonstrating the universal role of Br.

4.2 Origin of the bromide-altered growth pathway

In addition to changing the perovskite lattice constant and bandgap, our above analyses suggest that bromide affected the perovskite formation dynamics. Bromide and iodide have different solubility with the coordinating solvents used for perovskite deposition, such as DMF, DMSO and GBL. We further utilized Density Functional Theory (DFT) to calculate the interaction energies of PbXX' (X and X' denote either I or Br) species with DMSO. DMSO is partially removed by the anti-solvent during spin-coating, but the remaining residuals would form an adduct phase with PbXX' and FAX to assist with the formation of the α-phase perovskite.(*21*, *22*) From the optimized molecular configurations and bond distances shown in Figure 4.3A, and the interaction energies summarized in Figure 4.3B, DMSO bonds most strongly with PbI_2 (0.84 eV), followed by PbIBr (0.79 eV), and has the weakest bond with $PbBr_2$ (0.77 eV), indicating that Br-rich species have lower solubility and therefore potentially nucleate first during supersaturation. Moreover, the formation energies for the PbXX':DMSO adduct crystals were also calculated (Supplementary Figure B16 includes the optimized crystal structures). The formation energies decreased as I was gradually replaced by Br (-0.18 eV for PbI_2:DMSO, -1.10 eV for PbIBr:DMSO and -1.32 eV for $PbBr_2$:DMSO), suggesting that bromide-containing intermediate adduct phases are more thermodynamically favored to form. The surface energies between the tri-iodide perovskites with various A-site cations were also calculated to be much higher than that of the tri-bromide perovskites, regardless of the A-site cation (either PbX_2 or X-site termination, Supplementary Figure B4.17), indicating that Br species preferentially nucleate first, given that surface free energy

increases the total free energy of nucleation. Taking the theoretical results altogether, bromide-containing species are therefore thermodynamically more favored to form compared to iodide-containing species, and therefore complements the experimental observations that bromide-rich species formed first during the initial nucleation stage.

Both the experimental and theoretical results are complementary in showing that bromide drastically altered the perovskite formation dynamics by 1. promoting the initial nucleation of a bromide-rich species, and 2. introducing an anion-exchange-like halide homogenization process, which is necessary to attain the final stoichiometry from the initial bromide-rich phase. The homogenization process is associated with a reconstruction of the PbX_6 polyhedrons, with iodide diffusing towards the nuclei interior while bromide diffusing outwards, or even halide migration across the interfaces. Unlike cation-exchange or "molecular"-exchange processes reported to assist the growth of high quality thin film perovskites,(*23*, *24*) homogenization and self-diffusion of the anions during the nucleation and growth stages have rarely been studied for thin film perovskites. Importantly, such processes have been shown to assist defect formation in other material systems, especially when interstitial diffusion and vacancy-assisted diffusion are the dominant pathways to homogenize the halides.(*25*, *26*) We thus speculated that during the growth stage of $FAMACsPb(I_{0.8}Br_{0.2})_3$, these exchange and diffusion processes during homogenization promoted the formation of intrinsic defects associated with the halides, including vacancies, interstitials, and anti-sites. Our previous reports have shown the detrimental effects of point defects in perovskite materials, including V_I, Pb_I, and I_i.(*9*, *27*, *28*) Complementarily, the strong PbI_2 peak intensity observed by XRD for the fully annealed $FAMACsPb(I_{0.8}Br_{0.2})_3$ films suggests that the organic A-site cations were less stable and decompose more readily with higher Br% incorporation, which is supported by further theoretical calculations that show V_{FA} and FA_i were thermodynamically more

favored to form when the Br% increases from 0% to 20% (Supplementary Figure C4.18).

4.3 Thin film and device characterizations

To investigate the defect density and nature of the films, we first compared the optoelectronic properties of the films using time-resolved photoluminescence (TRPL) measurements shown in Figure 4.3C. A much shorter carrier lifetime of $\tau = 382.8$ ns is observed for the FAMACsPb($I_{0.8}Br_{0.2}$)$_3$ film, compared to the $\tau = 842.6$ ns of FAMACsPbI$_3$. Additionally, we measured the quantified PL of the films and extracted the quasi-Fermi level splitting (qFLs) (Figure 4.3D) based on a method we previously reported(29). The results show that the increasing quasi-fermi level splitting did not track the bandgap increase with higher Br% incorporation. In fact, 20% Br incorporation resulted in the largest V_{OC} losses ($V_{OC,SQ}$ – qFLS at 1 sun, Figure 4.3E), and the voltage loss was reduced as Br% decreased. The large V_{OC} loss for the 0% Br sample is potentially due to α-phase degradation by exposure to high ambient humidity of ~40% RH during sample measurement. Importantly, halide segregation during illumination was negligible for the FAMACsPb($I_{0.8}Br_{0.2}$)$_3$ film due to its highly optimized composition, as seen by its stable emission peak positions retained during continuous PL measurements (Figure 4.3F).

Positron Annihilation Spectroscopy (PAS) utilizes positively-charged positrons that annihilate with negatively charged/neutral defects, capable of non-destructively probing the density and spatial distribution of defects in semiconductor thin films, and has been reported to be compatible with halide perovskite materials.(30, 31) Compared with admittance spectroscopy that also provides information about trap density, PAS could be carried out directly on bare perovskite films and is therefore independent from experimental variables that affect admittance spectroscopy results, such as the bandgap of the materials (which affects the device built-in potential) and the properties of the contacting transport materials.(32) By controlling the kinetic energy of the

incident positron beam and extracting the shape parameter from the gamma-ray annihilation spectra (where a stronger gamma-ray signal from positron annihilation could derive a larger shape parameter, indicating a higher density of negatively charged/neutral defects), a depth-resolved spectrum was obtained in Figure 4.3G for the $FAMACsPb(I_{0.8}Br_{0.2})_3$ and $FAMACsPbI_3$ films. We observed that the shape parameter for $FAMACsPb(I_{0.8}Br_{0.2})_3$ was clearly higher throughout the entire perovskite film, indicating a higher overall trap density. The surface region (shaded in green, 0-50 nm) contained a much higher density of surface defects, which will be detrimental to both the device performance and stability. $FAMACsPb(I_{0.8}Br_{0.2})_3$ had a higher shape parameter in the entire perovskite bulk region (shaded in orange, 150-500 nm), indicating a higher trap density throughout the entire film. Crucially, this indicates that the defects formed through intrinsic processes (i.e. during perovskite formation and growth). In contrast, extrinsic processes (e.g. degradation) would have initiated from the film surface, preserving the bulk trap density of the film.(*33*, *34*) Statistical analysis of the shape parameters comparing the surface and bulk regions are displayed in Figure 4.3H. The eventual performance of the solar cell devices is a reflective consequence of the distinct defect physics and carrier dynamics of the films. As shown in Figure 4.4A, devices based on both compositions exhibited >79% FF, while the J_{SC} of $FAMACsPb(I_{0.8}Br_{0.2})_3$ (23.1 mA/cm^2) was distinctly lower than that of $FAMACsPbI_3$ (25.1 mA/cm^2) due to the larger bandgap of the former. The EQE cutoffs (Figure 4.4B) of the devices also matched well with the bandgaps estimated by the UV-Vis absorption and PL measurements. The *Voc* gain of $FAMACsPb(I_{0.8}Br_{0.2})_3$ over $FAMACsPbI_3$, however, was insufficient to compensate for the bandgap increase, with V_{OC} values of 1.16 V and 1.19 V, ($V_{OC,SQ}$ - V_{OC} of 0.13 V and 0.20 V, qE_g -V_{OC} of 0.40 V and 0.48V) respectively. The solar cell performance results coincided with the film characterization results, where non-radiative recombination losses were more severe for the $FAMACsPb(I_{0.8}Br_{0.2})_3$

perovskite. A stability test was also carried out, from which the FAMACsPbI$_3$ devices exhibited a much better long-term stability under illumination than FAMACsPb(I$_{0.8}$Br$_{0.2}$)$_3$ devices after encapsulation (Supplementary Figure C4.20). However, we found that the non-encapsulated devices of FAMACsPbI$_3$ decayed at a much faster rate, which is consistent with our observation during the PLQY tests regarding the fatal extrinsic instability (most likely due to moisture-induced phase transformation) of the FAMACsPbI$_3$ perovskite. Detailed discussion on stability test available in Supplementary Text.

4.4 Conclusion

Based on all our experimental and theoretical observations and results, we summarize the physical model of the formation dynamics of WBG mixed-halide perovskites in Figure 4.4C. The inclusion of bromide in the composition altered the perovskite crystallization pathway. A bromide-rich phase was more thermodynamically stable and thus nucleates first from solution during supersaturation. In order to attain the final target stoichiometry, during the growth stage, a halide homogenization process by diffusion gradually incorporates iodine into the expanding perovskite lattice. However, intrinsic defects formed readily during the homogenization process, and consequently, the final film had a higher defect density across the entire film depth, compared to the corresponding tri-iodide composition. Consequently, the WBG composition suffered from more severe non-radiative recombination losses, and thus inferior optoelectronic properties and device performance. In this work, we correlated the complex perovskite formation dynamics with the defect physics and charge carrier dynamics of the resulting film. This study will guide the community to rethink the significance of precursor engineering and crystallization control for WBG mixed-halide perovskites towards more efficient and stable PVs based on these materials.

4.5 References

1. M. Green, E. Dunlop, J. Hohl-Ebinger, M. Yoshita, N. Kopidakis, X. Hao, Solar cell efficiency tables (version 57). *Prog. Photovoltaics Res. Appl.* **29**, 3–15 (2021).

2. D. P. Mcmeekin, G. Sadoughi, W. Rehman, G. E. Eperon, M. Saliba, M. T. Hörantner, A. Haghighirad, N. Sakai, L. Korte, B. Rech, M. B. Johnston, L. M. Herz, H. J. Snaith, A mixed-cation lead mixed-halide perovskite absorber for tandem solar cells.

3. B. R.-C. E. Chart, Best Research-Cell Efficiency Chart. *https://www.nrel.gov/pv/cell-efficiency.html* (2021) (available at https://www.nrel.gov/pv/cell-efficiency.html).

4. M. Jeong, I. W. Choi, E. M. Go, Y. Cho, M. Kim, B. Lee, S. Jeong, Y. Jo, H. W. Choi, J. Lee, J.-H. Bae, S. K. Kwak, D. S. Kim, C. Yang, Stable perovskite solar cells with efficiency exceeding 24.8% and 0.3-V voltage loss. *Science.* **369**, 6511, 1615-1620 (2020).

5. A. Al-Ashouri, E. Köhnen, B. Li, A. Magomedov, H. Hempel, P. Caprioglio, J. A. Márquez, A. B. Morales Vilches, E. Kasparavicius, J. A. Smith, N. Phung, D. Menzel, M. Grischek, L. Kegelmann, D. Skroblin, C. Gollwitzer, T. Malinauskas, M. Jošt, G. Matič, B. Rech, R. Schlatmann, M. Topič, L. Korte, A. Abate, B. Stannowski, D. Neher, M. Stolterfoht, T. Unold, V. Getautis, S. Albrecht, Monolithic perovskite/silicon tandem solar cell with >29% efficiency by enhanced hole extraction. *Science*. **370**, 6522, 1300-1309 (2020).

6. G.-W. Kim, A. Petrozza, Defect Tolerance and Intolerance in Metal-Halide Perovskites. *Adv. Energy Mater.* **10**, 2001959 (2020).

7. K. X. Steirer, P. Schulz, G. Teeter, V. Stevanovic, M. Yang, K. Zhu, J. J. Berry, Defect Tolerance in Methylammonium Lead Triiodide Perovskite. *ACS Energy Lett.* **1**, 360–366 (2016).

8. Z. Ni, C. Bao, Y. Liu, Q. Jiang, W.-Q. Wu, S. Chen, X. Dai, B. Chen, B. Hartweg, Z. Yu, Z.

Holman, J. Huang, Resolving spatial and energetic distributions of trap states in metal halide perovskite solar cells. *Science*. **367**, 6484, 1352-1358 (2020).

9. R. Wang, J. Xue, K.-L. Wang, Z.-K. Wang, Y. Luo, D. Fenning, G. Xu, S. Nuryyeva, T. Huang, Y. Zhao, J. L. Yang, J. Zhu, M. Wang, S. Tan, I. Yavuz, K. N. Houk, Y. Yang, Constructive molecular configurations for surface-defect passivation of perovskite photovoltaics. *Science.* **366**, 6472, 1509-1513 (2019).

10. M. Qin, K. Tse, T.-K. Lau, Y. Li, C.-J. Su, G. Yang, J. Chen, J. Zhu, U.-S. Jeng, G. Li, H. Chen, X. Lu, Manipulating the Mixed-Perovskite Crystallization Pathway Unveiled by In Situ GIWAXS. *Adv. Mater.* **31**, 1901284 (2019).

11. J.-P. Correa-Baena, Y. Luo, T. M. Brenner, J. Snaider, S. Sun, X. Li, M. A. Jensen, N. T. P. Hartono, L. Nienhaus, S. Wieghold, J. R. Poindexter, S. Wang, Y. S. Meng, T. Wang, B. Lai, M. V Holt, Z. Cai, M. G. Bawendi, L. Huang, T. Buonassisi, D. P. Fenning, Homogenized halides and alkali cation segregation in alloyed organic-inorganic perovskites. *Science.* **363**, 6427, 627-631 (2019).

12. R. E. Beal, N. Z. Hagström, J. Barrier, A. Gold-Parker, R. Prasanna, K. A. Bush, D. Passarello, L. T. Schelhas, K. Brüning, C. J. Tassone, H.-G. Steinrück, M. D. McGehee, M. F. Toney, A. F. Nogueira, Structural Origins of Light-Induced Phase Segregation in Organic-Inorganic Halide Perovskite Photovoltaic Materials. *Matter*. **2**, 207–219 (2020).

13. S. Mahesh, J. M. Ball, R. D. J. Oliver, D. P. McMeekin, P. K. Nayak, M. B. Johnston, H. J. Snaith, Revealing the origin of voltage loss in mixed-halide perovskite solar cells. *Energy Environ. Sci.* **13**, 258–267 (2020).

14. C. M. Sutter-Fella, Q. P. Ngo, N. Cefarin, K. L. Gardner, N. Tamura, C. V Stan, W. S. Drisdell, A. Javey, F. M. Toma, I. D. Sharp, Cation-Dependent Light-Induced Halide

Demixing in Hybrid Organic–Inorganic Perovskites. *Nano Lett.* **18**, 3473–3480 (2018).

15. E. S. Parrott, J. B. Patel, A.-A. Haghighirad, H. J. Snaith, M. B. Johnston, L. M. Herz, Growth modes and quantum confinement in ultrathin vapour-deposited MAPbI3 films. *Nanoscale*. **11**, 14276–14284 (2019).

16. T.-B. Song, Z. Yuan, F. Babbe, D. P. Nenon, E. Aydin, S. De Wolf, C. M. Sutter-Fella, Dynamics of Antisolvent Processed Hybrid Metal Halide Perovskites Studied by In Situ Photoluminescence and Its Influence on Optoelectronic Properties. *ACS Appl. Energy Mater.* **3**, 2386–2393 (2020).

17. T.-B. Song, Z. Yuan, M. Mori, F. Motiwala, G. Segev, E. Masquelier, C. V Stan, J. L. Slack, N. Tamura, C. M. Sutter-Fella, Revealing the Dynamics of Hybrid Metal Halide Perovskite Formation via Multimodal In Situ Probes. *Adv. Funct. Mater.* **30**, 1908337 (2020).

18. L. Gao, G. Yang, Organic-Inorganic Halide Perovskites: From Crystallization of Polycrystalline Films to Solar Cell Applications. *Sol. RRL*. **4**, 1900200 (2020).

19. J.-W. Lee, S. Tan, T.-H. Han, R. Wang, L. Zhang, C. Park, M. Yoon, C. Choi, M. Xu, M. E. Liao, S.-J. Lee, S. Nuryyeva, C. Zhu, K. Huynh, M. S. Goorsky, Y. Huang, X. Pan, Y. Yang, Solid-phase hetero epitaxial growth of α-phase formamidinium perovskite. *Nat. Commun.* **11**, 5514 (2020).

20. J.-W. Lee, Z. Dai, C. Lee, H. M. Lee, T.-H. Han, N. De Marco, O. Lin, C. S. Choi, B. Dunn, J. Koh, D. Di Carlo, J. H. Ko, H. D. Maynard, Y. Yang, Tuning Molecular Interactions for Highly Reproducible and Efficient Formamidinium Perovskite Solar Cells via Adduct Approach. *J. Am. Chem. Soc.* **140**, 6317–6324 (2018).

21. N. Ahn, D.-Y. Son, I.-H. Jang, S. M. Kang, M. Choi, N.-G. Park, Highly Reproducible Perovskite Solar Cells with Average Efficiency of 18.3% and Best Efficiency of 19.7%

Fabricated via Lewis Base Adduct of Lead(II) Iodide. *J. Am. Chem. Soc.* **137**, 8696–8699 (2015).

22. Y.-M. Xie, B. Yu, C. Ma, X. Xu, Y. Cheng, S. Yuan, Z.-K. Wang, H. T. Chandran, C.-S. Lee, L.-S. Liao, S.-W. Tsang, Direct observation of cation-exchange in liquid-to-solid phase transformation in FA1−xMAxPbI3 based perovskite solar cells. *J. Mater. Chem. A*. **6**, 9081–9088 (2018).

23. W. S. Yang, J. H. Noh, N. J. Jeon, Y. C. Kim, S. Ryu, J. Seo, S. Il Seok, High-performance photovoltaic perovskite layers fabricated through intramolecular exchange. *Science.* **348**, 6240, 1234-1237 (2015).

24. S. Exarhos, E. Palmes, L. Mangolini, Structural homogenization and cation ordering in CZTS films during sulfurization as probed via in-situ Raman. *Thin Solid Films*. **684**, 21–30 (2019).

25. H. P. Ho, I. Harrison, N. Baba-Ali, B. Tuck, Diffusion-induced defects in GaAs by zinc and the effects of post-diffusion anneal. *J. Appl. Phys.* **69**, 3494–3502 (1991).

26. Y. Zhao, P. Zhu, S. Huang, S. Tan, M. Wang, R. Wang, J. Xue, T.-H. Han, S.-J. Lee, A. Zhang, T. Huang, P. Cheng, D. Meng, J.-W. Lee, J. Marian, J. Zhu, Y. Yang, Molecular Interaction Regulates the Performance and Longevity of Defect Passivation for Metal Halide Perovskite Solar Cells. *J. Am. Chem. Soc.* **142**, 20071–20079 (2020).

27. S. Tan, I. Yavuz, M. H. Weber, T. Huang, C.-H. Chen, R. Wang, H.-C. Wang, J. H. Ko, S. Nuryyeva, J. Xue, Y. Zhao, K.-H. Wei, J.-W. Lee, Y. Yang, Shallow Iodine Defects Accelerate the Degradation of α-Phase Formamidinium Perovskite. *Joule*. **4**, 2426–2442 (2020).

28. F. Babbe, L. Choubrac, S. Siebentritt, Quasi Fermi level splitting of Cu-rich and Cu-poor

Cu(In,Ga)Se2 absorber layers. *Appl. Phys. Lett.* **109**, 82105 (2016).

29. S. Tan, T. Huang, I. Yavuz, R. Wang, M. H. Weber, Y. Zhao, M. Abdelsamie, M. E. Liao, H.-C. Wang, K. Huynh, K.-H. Wei, J. Xue, F. Babbe, M. S. Goorsky, J.-W. Lee, C. M. Sutter-Fella, Y. Yang, Surface Reconstruction of Halide Perovskites During Post-treatment. *J. Am. Chem. Soc.* **143**, 6781–6786 (2021).

30. M.-F. Barthe, H. Labrim, A. Gentils, P. Desgardin, C. Corbel, S. Esnouf, J. P. Piron, Positron annihilation characteristics in UO2: for lattice and vacancy defects induced by electron irradiation. *Phys. status solidi c*. **4**, 3627–3632 (2007).

31. S. S. Hegedus, W. N. Shafarman, Thin-film solar cells: device measurements and analysis. *Prog. Photovoltaics Res. Appl.* **12**, 155–176 (2004).

32. B. Chen, P. N. Rudd, S. Yang, Y. Yuan, J. Huang, Imperfections and their passivation in halide perovskite solar cells. *Chem. Soc. Rev.* **48**, 3842–3867 (2019).

33. D. Meggiolaro, E. Mosconi, F. De Angelis, Formation of Surface Defects Dominates Ion Migration in Lead-Halide Perovskites. *ACS Energy Lett.* **4**, 779–785 (2019).

34. M. Abdelsamie, J. Xu, K. Bruening, C. J. Tassone, H.-G. Steinrück, M. F. Toney, Impact of Processing on Structural and Compositional Evolution in Mixed Metal Halide Perovskites during Film Formation. *Adv. Funct. Mater.* **30**, 2001752 (2020).

35. M. Abdelsamie, T. Li, F. Babbe, J. Xu, Q. Han, V. Blum, C. M. Sutter-Fella, D. B. Mitzi, M. F. Toney, Mechanism of Additive-Assisted Room-Temperature Processing of Metal Halide Perovskite Thin Films. *ACS Appl. Mater. Interfaces*. **13**, 13212–13225 (2021).

36. S. Tan, I. Yavuz, M. H. Weber, T. Huang, C.-H. Chen, R. Wang, H.-C. Wang, J. H. Ko, S. Nuryyeva, J. Xue, Y. Zhao, K.-H. Wei, J.-W. Lee, Y. Yang, Shallow Iodine Defects Accelerate the Degradation of α-Phase Formamidinium Perovskite. *Joule*. **4**, 2426–2442

(2020).

37. D. J. Frisch, M. J.; Trucks, G. W.; Schlegel, H. B.; Scuseria, G. E.; Robb, M. A.; Cheeseman, J. R.; Scalmani, G.; Barone, V.; Petersson, G. A.; Nakatsuji, H.; Li, X.; Caricato, M.; Marenich, A. V.; Bloino, J.; Janesko, B. G.; Gomperts, R.; Mennucci, B.; Hratch, Gaussian 16, Revision A.03. *Gaussian, Inc., Wallingford CT* (2016).

38. C. F. Macrae, I. Sovago, S. J. Cottrell, P. T. A. Galek, P. McCabe, E. Pidcock, M. Platings, G. P. Shields, J. S. Stevens, M. Towler, P. A. Wood, Mercury 4.0: from visualization to analysis, design and prediction. *J. Appl. Crystallogr.* **53**, 226–235 (2020).

39. C. F. Macrae, P. R. Edgington, P. McCabe, E. Pidcock, G. P. Shields, R. Taylor, M. Towler, J. van de Streek, Mercury: visualization and analysis of crystal structures. *J. Appl. Crystallogr.* **39**, 453–457 (2006).

40. I. J. Bruno, J. C. Cole, P. R. Edgington, M. Kessler, C. F. Macrae, P. McCabe, J. Pearson, R. Taylor, New software for searching the Cambridge Structural Database and visualizing crystal structures. *Acta Crystallogr. Sect. B.* **58**, 389–397 (2002).

41. G. Kresse, J. Furthmüller, Efficiency of ab-initio total energy calculations for metals and semiconductors using a plane-wave basis set. *Comput. Mater. Sci.* **6**, 15–50 (1996).

42. G. Kresse, J. Furthmüller, Efficient iterative schemes for ab initio total-energy calculations using a plane-wave basis set. *Phys. Rev. B.* **54**, 11169–11186 (1996).

43. J. P. Perdew, A. Ruzsinszky, G. I. Csonka, O. A. Vydrov, G. E. Scuseria, L. A. Constantin, X. Zhou, K. Burke, Restoring the Density-Gradient Expansion for Exchange in Solids and Surfaces. *Phys. Rev. Lett.* **100**, 136406 (2008).

44. J. P. Perdew, K. Burke, M. Ernzerhof, Generalized Gradient Approximation Made Simple. *Phys. Rev. Lett.* **77**, 3865–3868 (1996).

45. S. Grimme, J. Antony, S. Ehrlich, H. Krieg, A consistent and accurate ab initio parametrization of density functional dispersion correction (DFT-D) for the 94 elements H-Pu. *J. Chem. Phys.* **132**, 154104 (2010).

46. S. Grimme, Semiempirical GGA-type density functional constructed with a long-range dispersion correction. *J. Comput. Chem.* **27**, 1787–1799 (2006).

47. P. E. Blöchl, Projector augmented-wave method. *Phys. Rev. B*. **50**, 17953–17979 (1994).

48. G. I. Csonka, J. P. Perdew, A. Ruzsinszky, P. H. T. Philipsen, S. Lebègue, J. Paier, O. A. Vydrov, J. G. Ángyán, Assessing the performance of recent density functionals for bulk solids. *Phys. Rev. B*. **79**, 155107 (2009).

Figure 4.1 Abnormal formation dynamics in wide bandgap mixed-halide perovskites. (A) Photographs of the as-cast (top) and fully annealed (bottom) perovskite films with the stoichiometries of $CsFAMAPb(I_{0.8}Br_{0.2})_3$ (left) and $CsFAMAPbI_3$ (right). (B) Absorption spectra of $FAMACsPbX_3$ films before(as-cast)/after fully annealed. (C) XRD spectra of (001) peak of $FAMACsPbX_3$ films.

Figure 4.2 In-situ photoluminescence measurements monitoring the formation kinetics of perovskite films. (A) Illustration of the in-situ PL measurement during spin-coating and annealing stage of perovskite formation. The contour plot of the captured PL spectra during the growth of (B) CsFAMAPb(I$_{0.8}$Br$_{0.2}$)$_3$ and (C) CsFAMAPbI$_3$ films during spin-coating (left) and annealing (right). The extracted values of emission peak position (D), PL intensity (E), and FWHM (F) from the in-situ PL measurements.

Figure 4.3 First-principle calculations and characterizations of the fully annealed perovskite films. (A) Molecular configuration and interaction distance of coordinating solvent DMSO and PbXX' molecules. (B) Interaction energy between DMSO and PbXX' molecule and formation energy of DMSO:PbXX' adduct phase. (C) Time-resolved PL spectra of the as-prepared CsFAMAPb($I_{0.8}Br_{0.2})_3$ and CsFAMAPbI$_3$ films. (D) Quasi-Fermi level splitting results quantified by a calibrated laser intensity, and (E) the as extracted $V_{OC,loss}$ ($V_{OC,SQ}$ - qFLs) for perovskite films with Br% of 20%, 10%, 5% and 0%. (F) The extracted values of emission peak position from 60 s PL tracking. (G) PAS depth-profiling of CsFAMAPb($I_{0.8}Br_{0.2})_3$ and CsFAMAPbI$_3$ films. Solid lines are fitted plots. Green/orange shaded areas indicate the top surface/bulk region of the films. (H) Shape parameters from PAS extracted for the surface/bulk regions.

69
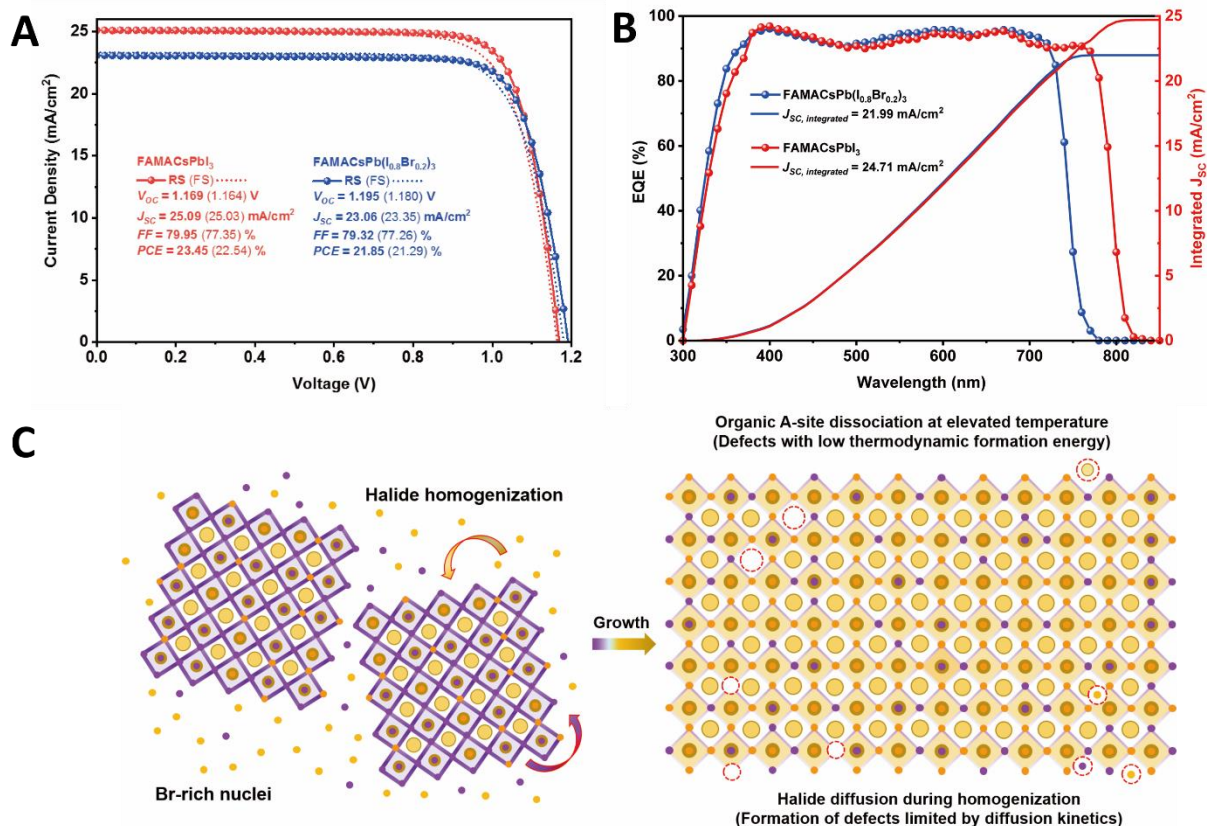
Figure 4.4 Solar cell devices and the proposed physical model. *J-V* **characteristics** (A) and EQE spectrum (B) of perovskite solar cell devices based on CsFAMAPb(I$_{0.8}$Br$_{0.2}$)$_3$ and CsFAMAPbI$_3$. (C) A hypothetic physical model of formation kinetics in mixed-halide perovskite with high Br% (left) and their potential role with defect physics (right). Violet dots stand for bromine, yellow dots stand for iodine. Several but not all possible point defects were illustrated at the surface or in the bulk. For simplification purpose, only the halides were specified for Br as purple dots and I as yellow dots.

Chapter 5. First-principles study of surface defects in FAPbI$_3$ perovskite

Halide perovskite materials have emerged for their potential optoelectronic applications, including as solar cells, light emitting diodes, and piezoelectronics. One of the featured halide perovskite materials, namely formamidinium (NH$_2$CH=NH$_2^+$ or FA$^+$) lead triiodide (FAPbI$_3$), has stood out for photovoltaic applications as it has a close-to-optimum bandgap of 1.48 eV, strong absorption coefficient, long charge carrier lifetime and exceptional defect tolerance.[1,2] With less than 10 years of development since solid-state halide perovskites were firstly adopted for thin film electronics, FAPbI$_3$ has recently achieved exceptional power conversion efficiencies as high as 25.52%, which already exceeds several inorganic counterparts such as polycrystalline silicon and Cu(In,Ga)Se$_2$ solar cells.[3]

Looking back at the history of PCE improvement of halide perovskite solar cells, their development has always been paired with the suppression of non-radiative charge recombination losses.[4,5] Compared with the charge carrier lifetimes in halide perovskite single crystals, photovoltaic perovskite polycrystalline thin films exhibited less ideal charge carrier dynamics, indicating that these materials show distinct defect physics at the interfaces such as the film surface and the grain boundaries.[6,7] Although successful passivation of the surface defects has enabled the recent performance surge, it remains unclear what defects are dominant and in which way they are now passivated that has led to the over 25% halide perovskite solar cells. In addition, defects, even shallow defects that are considered benign for photovoltaic performance, serve as degradation centers that are more sensitive to moisture and oxygen, and limit the long-term stability of perovskite solar cells.[8,9] To unravel the success in over 25% efficiency perovskite solar cells and further push their long-term stability for potential commercialization, in-depth study that identifies the defects existing in halide perovskite is thus essential to assist further developing optimum

fabrication processes, targeted passivating strategies, and understanding their specific role in perovskite degradation.

To investigate the defect physics of halide perovskites, Density Functional Theory (DFT) calculations are exceptionally useful to systematically study the type, nature, and position of intrinsic defects. Over the past years, the intrinsic defect landscape of methylammonium ($CH_3NH_3^+$ or MA^+) lead triiodide ($MAPbI_3$) has been variously investigated and utilized to improve the optoelectronic properties and stability of its PV devices.[10–12] However, these calculations are not yet completely done for $FAPbI_3$.

Substituting the A-site cation MA^+ with FA^+ has demonstrated several advantages for photovoltaic perovskites. For example, the relatively larger size of FA^+ can form a more symmetric perovskite crystal structure, converting the perovskite phase from $MAPbI_3$'s tetragonal phase to $FAPbI_3$'s cubic phase. Secondly, compared with $MAPbI_3$'s bandgap of 1.55 eV, $FAPbI_3$ perovskite has a much smaller bandgap of 1.48 eV, which is closer to the ideal value defined by the single junction solar cell's Shockley-Queisser efficiency limit.[13] Meanwhile, it has been reported that the organic FA decomposes at a higher temperature than MA, while the latter is known to dissociate into ammonia, CH_3I, and iodine at less than 100 ℃ or under strong illumination.[6,14–16] Recent breakthroughs in perovskite photovoltaics that have achieved over 25% power conversion efficiency, all mostly based on pure $FAPbI_3$ or $FAPbI_3$-based compositions rather than $MAPbI_3$.[17,18] However, these different structural and optoelectronic properties in $FAPbI_3$ perovskite could also lead to distinct defect physics. Certain defects could potentially form more readily and introduce deep-level trap states in the bandgap. The deviation from the original lattice (with the presence of defects) may also decrease the steric impedance of the phase transformation from the meta-stable α-phase $FAPbI_3$ to its photo inactive δ-phase.

Back in 2018, Yam et. al. calculated the formation energies and transition levels of intrinsic bulk defects in FAPbI$_3$, which has been a guideline for the community to understand the intrinsic defects in FAPbI$_3$ since.[1] A comprehensive and systematic picture of surface defects in FAPbI$_3$, however, has not yet been fully elucidated. In fact, due to the solution processed nature of thin film halide perovskites, the surface region is known to be the most abundant with defects, as revealed by a series of defect characterization techniques for semiconductors, including drive level capacitance transient profiling (DLCP) and positron annihilation spectroscopy (PAS).[7,19,20] Our previous reports have also studied the interaction of several featured surface defects of FAPbI$_3$ (including V$_I$, Pb$_I$, I$_{int}$, FA$_I$, etc.).[19,21–23] With rational passivation of these surface defects, both the device performance and stability were improved.

5.1 Computational details

In order to investigate the intrinsic defects at the FAPbI$_3$ surface, a 4-layer 3*3 FAPbI$_3$ γ-phase perovskite slab model is established as shown in Fig 5.1. All geometry optimizations and electronic calculations are performed using VASP code with gamma-point-only projector augmented-wave (PAW) method. Previous work has shown that the Heyd-Scuseria-Ernzerhof hybrid functional (HSE), in combination with spin-orbit-coupling (SOC) is more reliable in defect calculations of lead-containing perovskites.[24] However, considering the computation cost, we chose to use the Perdew-Burke-Ernzerhof (PBE) functional instead with extra precautions.[25] The cutoff energy is 400 eV. The criteria for ionic relaxation steps are: total energy difference $< 10^{-3}$ eV, forces on atoms < 0.05 eV/Å. The lattice is fixed. Here we discard the α-phase perovskite for defect calculations, since the α-phase is unstable in static DFT calculations[26] (however, it is dynamically stable), the defected α-phase supercell will turn to a γ-phase-like supercell after relaxation.

The formation energy of a neutral defect D is calculated according to the formula:

$$\Delta E(D) = E(D) - E(surface) \pm \mu(D)$$

where $E(D)$ is the total energy of the defected surface, $E(surface)$ is the total energy of a perfect surface model. $\mu(D)$ is the chemical potential of the defect atom that has been removed or added, and E_{Fermi} is the fermi level, which was set to be the valence band maximum in this study. The chemical potential of atom D can have difference choice in calculations of compounds, corresponding to different synthesis conditions. To simplify, we will use two conditions: I rich and Pb rich. For I rich, $\mu(I)$ is equal to the chemical potential of iodine solid, $\mu(Pb) = \mu(PbI_2) - 2\mu(I)$, and $\mu(FA) = \mu(FAPbI_3) - \mu(Pb) - 3\mu(I)$. For Pb rich condition, $\mu(Pb)$ is equal to the chemical potential of lead solid, and $2\mu(I) = \mu(PbI_2) - \mu(Pb)$, $\mu(FA) = \mu(FAPbI_3) - 3\mu(I) - \mu(Pb)$.

Due to the charge spreading problem in surface models,[24] we will not calculate charged surface defects as well as transition levels in this work, but the Kohn-Sham levels of neutral defects instead. For those Kohn-Sham levels in the bandgap, we can easily identify them as "defect levels", which are apparently caused by defects. We predict defects with defect levels deep in the bandgap as deep acceptors/donors. However, it is noteworthy to mention that defect levels are still an approximation, as accepting/donating electrons may change the geometries of defects, which cannot be captured by the defect levels of neutral defects. Besides, previous works ~~does~~ have shown that the Generalized Gradient Approximation (GGA) may underestimate the transition levels for some defects[24]. However, performing HSE+SOC calculations for defect models are very costly. Our GGA calculations have correctly predicted that FA_I and Pb_I were deep donors, as corroborated by experiments.[23,27] We believe that our calculations of the "defect levels" of neutral defects can be indicative of whether a defect is detrimental or not.

5.2 Defect formation energy and DOS

Based on the as constructed $FAPbI_3$ perovskite slab models, we calculated the density of states and the formation energy of the point defects at the surface. When the crystalline continuity is interrupted at the crystal surface, there are two representative surface terminations in halide perovskites, namely the FA-I termination and PbI_2 termination (also known as the flat termination). While the former terminates with a complete $[PbI_6]^{2-}$ octahedra layer with FA^+ occupying the central void, the latter cuts the octahedra layer in half and leaving a flat surface where only Pb and I atoms could be found at the top atomic layer (in the case of a defect-free scenario). The chemical environment of surface atoms changes completely when the surface configuration changes from the FA-I termination to the PbI_2 termination, and so we studied the surface defects individually for both terminations. The optimized geometries of surface defects were shown in Supplementary Figure C5.1 and B5.2.

For the FA-I termination, we considered the three vacancy defects (V_{FA}, V_{Pb}, V_I), three interstitial defects (FA_{int}, Pb_{int}, I_{int}), and five antisite defects (Pb_{FA}, FA_I, Pb_I, I_{FA}). Antistite substitution of Pb was not considered, because Pb cannot reside on the surface layer in the ideal FA-I termination surface, but lie in the PbX_6 cages, similar to the bulk scenario. The density of states of the perovskite slab with individual point defects present at the surface were calculated. Interestingly, our calculations suggest that under the FA-I termination, most defects did not induce localized states in the bandgap (Supplementary Figure C5.3). As is shown in Figure 5.2, there are three exceptions, which are Pb_I, FA_I, and I_{FA}. It is perhaps because of the fact that in lead halide perovskites, mainly the Pb p orbital contributes to the CBM, and the coupling of the Pb s orbital and I p orbital that consists of the valence band maximum (VBM), such that surface Pb_I introduced deep level states similar to bulk Pb_I, with the highest density of trap states among all surface defects

we studied.[1] The defect level was approximately 0.59 eV above the valence band edge and could be donated as an acceptor defect. The two antisites of FA_I and I_{FA} also facilitated trap states, but closer to the conduction band. The approximate defect levels extracted were 0.42 eV and 0.34 eV, respectively.

To calculate the formation energies of the surface defects for the FA-I termination, we considered two growth conditions for the electrochemical potential of the reservoirs, namely the I-rich and Pb-rich conditions. The formation energies of the surface defects are summarized in Table 5.1. Our results suggest that most point defects form more readily on the surface compared with their reported values in the bulk. For example, in the realistically more commonly encountered Pb-rich condition, the formation energy of the iodide related defects such as I_{int} and I_{FA} dropped from 1.66 eV and 2.45 eV in the bulk, to 1.00 eV and 1.74 eV at the surface, respectively. Under the I-rich condition, V_{FA}, I_{FA}, and I_{int} even showed negative or near zero formation energies, indicating that point defects may even spontaneously form at room temperature.

Similarly, for the PbI_2 termination, we also considered the three vacancy defects (V_{FA}, V_{Pb}, V_I), three interstitial defects (FA_{int}, Pb_{int}, I_{int}), but six antisite defects (Pb_{FA}, FA_{Pb}, FA_I, Pb_I, I_{FA}, I_{Pb}). In this case, since Pb can exist at the surface layer of the PbI_2 termination, we have also included its related antisite. Interestingly, surface defects in the PbI_2 termination contributed more complex electronic physics than the FA-I termination case. From the density of states results shown in Figure 5.3, we found that four surface defects contributed deep level states, namely Pb_{int}, FA_I, Pb_I, and I_{FA}, among which FA_I introduced a deep acceptor state of an approximate defect level of 0.51 eV (the rest of the defects shown in Supplementary Figure C5.4). Pb_{int} and I_{FA} both exhibited to be deep donors with defect levels near 0.30 and 0.25 eV, respectively. The presence of Pb_I

simultaneously generated two states in the bandgap, located at 0.68 eV and 0.19 eV. These results are found to be closer to the results calculated for bulk defects in FAPbI$_3$.

The defect formation energy for the surface defects in PbI$_2$ termination were also calculated based on the Pb-rich and I-rich conditions. As is summarized in Table 5.2, surface defects are much more likely to form compared with the FA-I termination situation. V$_I$ and FA$_{int}$ showed negative formation energy in the Pb-rich condition of -0.084 eV and -0.130 eV, respectively, indicating their formation could be thermally favorable. In the I-rich condition, the thermally favorable surface defects became FA$_{Pb}$ and I$_{Pb}$, whose formation energies were as low as -0.757 eV and -0.073 eV.

These first-principles calculation results provide a comprehensive picture of the intrinsic surface defect physics of FAPbI$_3$ perovskites. We summarized the type and their corresponding formation energy of six featured point defects at the surface of FAPbI$_3$ in Table 3. First, none of the surface vacancy defects become detrimental defects that create deep levels in the bandgap. However, the defect physics are very different when these surface vacancy defects are occupied with guest atoms. For example, the Pb$_I$ antisite is one of the featured surface defects whose energy level is located inside the perovskite bandgap. In the FA-I terminated FAPbI$_3$ surface, Pb$_I$ serves as a deep acceptor trap with a defect level of 0.59 eV, but its formation energy (2.09 eV) is yet considerably high to limit its formation. Under PbI$_2$-termination, Pb$_I$ exhibited two distinct states in the bandgap with defect levels of 0.68 eV and 0.19 eV, respectively, and thus serve as a donor trap. What is worth noticing is that, assisted by the Pb-rich environment, the donor defect Pb$_I$ at the PbI$_2$-terminated surface showed a much lower formation energy compared to the acceptor defect in FA-I termination, potentially due to the steric impedance of extracting Pb from the (PbI$_6$)$^{4-}$ octahedral in the FA-I terminated scenario. Pb$_{int}$ serves as a donor defect in PbI$_2$ termination only, whose defect

77

level is 0.30 eV below the CBM. As the formation of Pb_{int} does not require the displacement of either I or FA, this donor defect has an even lower formation energy than Pb_I (0.339 eV, in PbI_2 termination). Other than Pb, antisites of surface FA and I also generated deep-level trap states. Among the four featured defects associated with FA and I summarized in Table 3, we found only FA_I in the PbI_2 termination serves as an acceptor defect while the other three all show donor defect features. I_{FA} showed the smallest formation energy for all defects that create deep levels in the bandgap, even becoming negative for the FA-I termination (I-rich, -0.23 eV), indicating its spontaneous formation without any external stress such as heat or illumination. However, there are rarely reports associate with the possible detrimental effects to either device performance or perovskite stability induced by I_{FA}. We speculate that this may be due to the volatile nature of iodine, that allows I_{FA} to easily escape from the perovskite surface during annealing, which converts I_{FA} into V_{FA}.

5.3 Gap between theoretical and experimental results

The ultimate goal of investigating the surface defect landscape using DFT calculations is to link them to experimental results to develop possible defect mitigation or passivation strategies. So far, conventional characterizations are still unable to fully unravel the complete defect physics of a material. Capacitance/admittance-based methods such as deep-level capacitance profiling (DLCP), deep-level transient spectroscopy (DLTS), and thermal admittance spectroscopy (TAS) have been employed to perform quantitative analysis of trap density, activation energy, spatial distribution, etc. in perovskite-based devices, while photoluminescence spectroscopy methods may be able to decouple the effects of deep and shallow traps. However, none of these methods are capable of unravelling the specific type of defect present at the $FAPbI_3$ halide perovskite surface, including their preferred location, formation energy, and defect level of the corresponding traps.

Besides, the complex surface structure and mechanically vulnerable nature of halide perovskites make experimentally studying its surface even more challenging. For example, quantitative XPS peak analysis provides firsthand information of the material surface, especially the elemental ratio. With its surface sensitivity, XPS has been used to indirectly determine which termination or chemical condition is more reflective of the actual material surface. Ideally, the $FAPbI_3$ surface has an Pb/I atomic ratio of 1/3. However, as shown in Supplementary Figure C5.5, we noticed that even when the precursor solution was prepared by a stoichiometric ratio (i.e. $FAI:PbI_2 = 1:1$), quantitative XPS suggested that the freshly prepared $FAPbI_3$ thin films are Pb rich (29.87 At% for Pb and 70.13 At% for I). When excess PbI_2 was added to the precursor, the atomic ratio became as close to 1/2 (33.46 At% for Pb and 66.54 At% for I), indicating that there could even be PbI_2 at the perovskite surface. We found that in order to let the surface Pb/I atomic ratio reach approximately 1/3, excess FAI (10 mol% in our case) will be required. These results indicate that the Pb rich surface condition is generally more dominant. However, affected by the measurement itself, such as the high vacuum and strong beam damage to the perovskite by XPS, experimentally characterized surface features can still deviate from the **actual** surface termination.

Over the course of developing stable α-phase $FAPbI_3$ perovskites, additives whose sizes fit into the original crystal lattice matrix are generally incorporated, such as doping with $MAPbBr_3$, occupying the interstitial site, forming 2D/quasi-2D structures, or even modifying the surface termination.[17,28–30] The perovskite defects physics, such as the type and formation energy, could be easily changed. During post-deposition treatments to passivate surface defects, surface reconstruction could also occur to alter the surface from the pristine condition.

5.4 Conclusion

In conclusion, the defect nature, including the formation energy, density of states, estimated trap activation energy, and the corresponding defect type, have been systematically studied for the intrinsic surface defects of the FAPbI$_3$ perovskite via DFT calculations. The calculated results suggested that the intrinsic point defects exhibit very different characteristics when located at the surface compared with when they are in the material bulk. We also discussed the feasibility of directly utilizing these theoretical results to combine with experimental characterizations and correlating with the material properties.

5.5 Reference

[1] N. Liu and C. Yam, Phys. Chem. Chem. Phys. **20**, 6800 (2018).

[2] M. Jeong, I.W. Choi, E.M. Go, Y. Cho, M. Kim, B. Lee, S. Jeong, Y. Jo, H.W. Choi, J. Lee, J.-H. Bae, S.K. Kwak, D.S. Kim, and C. Yang, Science. **369**, 1615 (2020).

[3] NREL, Best Res. Effic. Chart (2021).

[4] B. Chen, P.N. Rudd, S. Yang, Y. Yuan, and J. Huang, Chem. Soc. Rev. **48**, 3842 (2019).

[5] F. Gao, Y. Zhao, X. Zhang, and J. You, Adv. Energy Mater. **10**, 1902650 (2020).

[6] Q. Han, S.-H. Bae, P. Sun, Y.-T. Hsieh, Y. (Michael) Yang, Y.S. Rim, H. Zhao, Q. Chen, W. Shi, G. Li, and Y. Yang, Adv. Mater. **28**, 2253 (2016).

[7] Z. Ni, C. Bao, Y. Liu, Q. Jiang, W.-Q. Wu, S. Chen, X. Dai, B. Chen, B. Hartweg, Z. Yu, Z. Holman, and J. Huang, Science. **367**, 1352 (2020).

[8] R. Wang, J. Xue, L. Meng, J.-W. Lee, Z. Zhao, P. Sun, L. Cai, T. Huang, Z. Wang, Z.-K. Wang, Y. Duan, J.L. Yang, S. Tan, Y. Yuan, Y. Huang, and Y. Yang, Joule **3**, 1464 (2019).

[9] H. Xie, Z. Wang, Z. Chen, C. Pereyra, M. Pols, K. Gałkowski, M. Anaya, S. Fu, X. Jia, P. Tang, D.J. Kubicki, A. Agarwalla, H.-S. Kim, D. Prochowicz, X. Borrisé, M. Bonn, C. Bao, X. Sun, S.M. Zakeeruddin, L. Emsley, J. Arbiol, F. Gao, F. Fu, H.I. Wang, K.-J. Tielrooij, S.D. Stranks, S. Tao, M. Grätzel, A. Hagfeldt, and M. Lira-Cantu, Joule **5**, 1246 (2021).

[10] W.-J. Yin, T. Shi, and Y. Yan, Appl. Phys. Lett. **104**, 63903 (2014).

[11] C. Quarti, F. De Angelis, and D. Beljonne, Chem. Mater. **29**, 958 (2017).

[12] S. Tan, I. Yavuz, N. De Marco, T. Huang, S.-J. Lee, C.S. Choi, M. Wang, S. Nuryyeva, R. Wang, Y. Zhao, H.-C. Wang, T.-H. Han, B. Dunn, Y. Huang, J.-W. Lee, and Y. Yang, Adv. Mater. **32**, 1906995 (2020).

[13] W. Shockley and H.J. Queisser, J. Appl. Phys. **32**, 510 (1961).

[14] S. Chen, X. Zhang, J. Zhao, Y. Zhang, G. Kong, Q. Li, N. Li, Y. Yu, N. Xu, J. Zhang, K. Liu, Q. Zhao, J. Cao, J. Feng, X. Li, J. Qi, D. Yu, J. Li, and P. Gao, Nat. Commun. **9**, 4807 (2018).

[15] E.J. Juarez-Perez, L.K. Ono, M. Maeda, Y. Jiang, Z. Hawash, and Y. Qi, J. Mater. Chem. A **6**, 9604 (2018).

[16] T. Huang, S. Tan, and Y. Yang, J. Phys. Chem. C. Article ASAP (2021).

[17] J.J. Yoo, G. Seo, M.R. Chua, T.G. Park, Y. Lu, F. Rotermund, Y.-K. Kim, C.S. Moon, N.J. Jeon, J.-P. Correa-Baena, V. Bulović, S.S. Shin, M.G. Bawendi, and J. Seo, Nature **590**, 587 (2021).

[18] J. Jeong, M. Kim, J. Seo, H. Lu, P. Ahlawat, A. Mishra, Y. Yang, M.A. Hope, F.T. Eickemeyer, M. Kim, Y.J. Yoon, I.W. Choi, B.P. Darwich, S.J. Choi, Y. Jo, J.H. Lee, B. Walker, S.M. Zakeeruddin, L. Emsley, U. Rothlisberger, A. Hagfeldt, D.S. Kim, M. Grätzel, and J.Y. Kim, Nature **592**, 381 (2021).

[19] S. Tan, I. Yavuz, M.H. Weber, T. Huang, C.-H. Chen, R. Wang, H.-C. Wang, J.H. Ko, S. Nuryyeva, J. Xue, Y. Zhao, K.-H. Wei, J.-W. Lee, and Y. Yang, Joule **4**, 2426 (2020).

[20] S. Tan, T. Huang, I. Yavuz, R. Wang, M.H. Weber, Y. Zhao, M. Abdelsamie, M.E. Liao, H.-C. Wang, K. Huynh, K.-H. Wei, J. Xue, F. Babbe, M.S. Goorsky, J.-W. Lee, C.M. Sutter-Fella, and Y. Yang, J. Am. Chem. Soc. **143**, 6781 (2021).

[21] R. Wang, J. Xue, K.-L. Wang, Z.-K. Wang, Y. Luo, D. Fenning, G. Xu, S. Nuryyeva, T. Huang, Y. Zhao, J.L. Yang, J. Zhu, M. Wang, S. Tan, I. Yavuz, K.N. Houk, and Y. Yang, Science. **366**, 1509 (2019).

[22] Y. Zhao, P. Zhu, S. Huang, S. Tan, M. Wang, R. Wang, J. Xue, T.-H. Han, S.-J. Lee, A. Zhang, T. Huang, P. Cheng, D. Meng, J.-W. Lee, J. Marian, J. Zhu, and Y. Yang, J. Am. Chem. Soc. **142**, 20071 (2020).

[23] R. Wang, J. Xue, X. Chen, C. Yao, Z.-K. Wang, M.H. Weber, A.H. Rose, S. Nuryyeva, J. Zhu,

T. Huang, Y. Zhao, S. Tan, M.C. Beard, Y. Yan, K. Zhu, and Y. Yang, Matter. 4, **7**, 2417-2428 (2021).

[24] M.-H. Du, J. Phys. Chem. Lett. **6**, 1461 (2015).

[25] J.P. Perdew, K. Burke, and M. Ernzerhof, Phys. Rev. Lett. **77**, 3865 (1996).

[26] J. Yang, X. Wen, H. Xia, R. Sheng, Q. Ma, J. Kim, P. Tapping, T. Harada, T.W. Kee, F. Huang, Y.B. Cheng, M. Green, A. Ho-Baillie, S. Huang, S. Shrestha, R. Patterson, and G. Conibeer, Nat. Commun. **8**, (2017).

[27] R. Wang, J. Xue, K.-L. Wang, Z.-K. Wang, Y. Luo, D. Fenning, G. Xu, S. Nuryyeva, T. Huang, Y. Zhao, J.L. Yang, J. Zhu, M. Wang, S. Tan, I. Yavuz, K.N. Houk, and Y. Yang, Science. **366**, 1509 (2019).

[28] H. Min, M. Kim, S.-U. Lee, H. Kim, G. Kim, K. Choi, J.H. Lee, and S. Il Seok, Science. **366**, 749 LP (2019).

[29] Y.-W. Jang, S. Lee, K.M. Yeom, K. Jeong, K. Choi, M. Choi, and J.H. Noh, Nat. Energy **6**, 63 (2021).

[30] J.J. Yoo, S. Wieghold, M.C. Sponseller, M.R. Chua, S.N. Bertram, N.T.P. Hartono, J.S. Tresback, E.C. Hansen, J.-P. Correa-Baena, V. Bulović, T. Buonassisi, S.S. Shin, and M.G. Bawendi, Energy Environ. Sci. **12**, 2192 (2019).
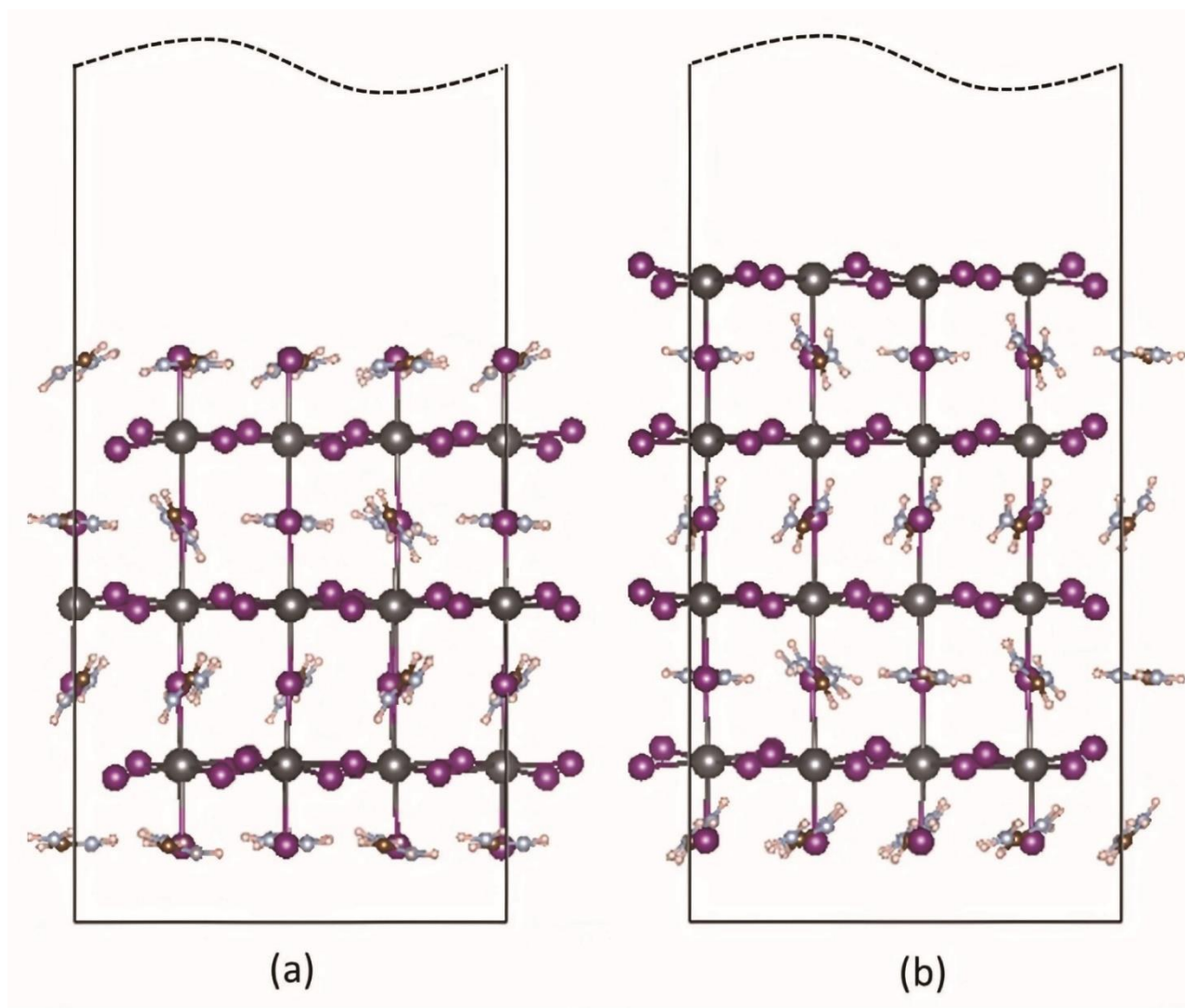
Figure 5.1 Supercell structures of FAPbI$_3$ after geometry optimizations. **(a)** FAI-terminated surface, and **(b)** PbI$_2$-terminated surface for defect calculations.
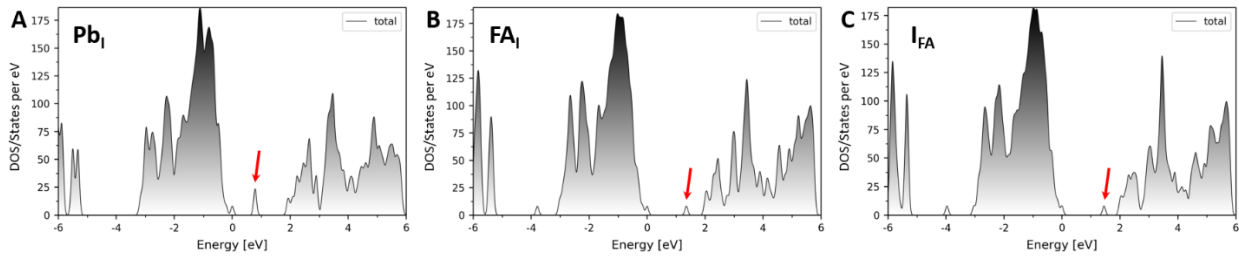
Figure 5.2 Calculated density of states (DOS) of FA-I terminated FAPbI$_3$ perovskite with surface point defects that form deep-level traps.
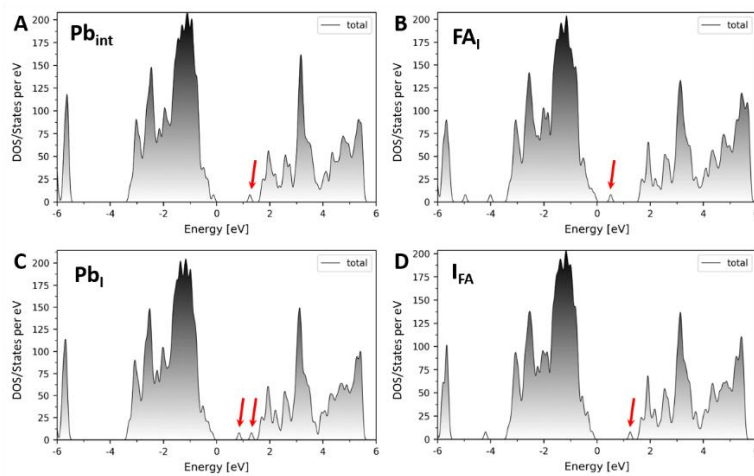
Figure 5.3 Calculated density of states (DOS) of PbI$_2$ terminated FAPbI$_3$ perovskite with surface point defects that form deep-level traps.

Table 5.1 Formation energies of surface defects in FA-I terminated $FAPbI_3$ perovskite using the PBE method (in eV).

Formation energy	V_{FA}	V_{Pb}	V_I	FA_{int}	Pb_{int}	I_{int}	FA_I	Pb_I	Pb_{FA}	I_{FA}
Pb rich	0.82	2.26	1.53	1.77	2.77	1.00	2.22	2.09	0.65	1.74
I rich	-0.17	0.29	2.25	2.75	4.74	0.017	4.19	5.05	1.64	-0.23

Table 5.2 Formation energies of surface defects in PbI_2 terminated $FAPbI_3$ perovskite using the PBE method (in eV).

Formation energy	V_{FA}	V_{Pb}	V_I	FA_{int}	Pb_{int}	I_{int}	FA_I	Pb_I	Pb_{FA}	I_{FA}	FA_{Pb}	I_{Pb}
Pb rich	1.158	2.080	-0.084	-0.130	0.339	1.976	0.260	1.233	0.312	2.028	0.228	2.880
I rich	0.174	0.111	0.900	0.854	2.308	0.992	2.229	4.186	1.296	0.060	-0.757	-0.073

Table 5.3 Type, estimated defect level, and formation energy (at preferred chemical conditions) of the featured surface defects in $FAPbI_3$

		Defect type	Defect Level (eV)	Formation Energy (eV)
	Pb_I	Acceptor	0.59	2.09 (Pb rich)
FA-I termination	FA_I	Donor	0.42	2.22 (Pb rich)
	I_{FA}	Donor	0.34	-0.23 (I rich)
	Pb_{int}	Donor	0.30	0.339 (Pb rich)
	FA_I	Acceptor	0.51	0.26 (Pb rich)
PbI_2 termination	Pb_I	Donor	0.68/0.19	1.233 (Pb rich)
	I_{FA}	Donor	0.25	0.06 (I rich)

Chapter 6. Enabling low voltage losses and high photocurrent in fullerene-free organic photovoltaics

Organic photovoltaics (OPVs) have several advantages such as potential low cost, absorption tunability, mechanical flexibility and roll-to-roll manufacture capability[1-11]. However, the power conversion efficiencies (PCEs) of OPVs are still inferior to their inorganic counterparts. One of the most significant factors, which hinders their device performance, is the relatively large loss in the open-circuit voltage (V_{OC}) with respect to the optical gap[12]. While the V_{OC} loss can be as low as 0.30 eV in GaAs and slightly higher in c-Si and organic-inorganic hybrid perovskite solar cells (from 0.40 to 0.55 eV), the V_{OC} loss for strongly absorbed photons in state-of-the-art OPVs is around 0.6 V or higher[13-15]. In an ideal OPV, maximum V_{OC} can be achieved only when sources of voltage losses are limited to an unavoidable radiative recombination of absorption species above the optical gap[16]. However, for the state-of-the-art OPVs, there are strong non-radiative recombination present leading to significant voltage losses, evidenced by electroluminescence quantum efficiency (EQE_{EL}) measurements[17-19]. Recombination of radiative charge-transfer (CT) states can also be present due to energetic offsets between the donor (D) and the acceptor (A) components[20-22]. In a very recent work[23], two design rules are formulated aiming at reducing the voltage loss and increasing the efficiency of OPVs: 1) Small energy offset between the donor and acceptor materials, and 2) High luminescence yield of the lower-gap single component (and hence the blend). Among the materials candidates meeting these design rules, A-D-A structured non-fullerene acceptors (NFAs) are extremely promising since they exhibit strong intramolecular charge transfer (ICT) effect, superior energy level tunability and good molecular crystallinity[24-27]. These features allow NFAs to become potential candidates for achieving an efficient charge separation and low voltage losses simultaneously as per the design rules.

From the aspect of molecular design, synthesis of donor and acceptor materials with

complementary absorption profiles intended to maximize the coverage of the solar spectrum, has been one of the prerequisites for achieving a high photocurrent. Thus, a variety of narrow optical gap NFAs based on a stronger electron-donating at the central core were carefully designed and synthesized for OPVs[28]. Undoubtedly, it is a successful strategy to elevate the HOMO level reducing the optical gap. Benzotriazole-based conjugated molecules with unique luminescence properties are common building blocks for increasing the photoluminescence quantum yield (PLQY) of the single component[29-32]. The high PLQY indicates efficient radiative recombination pathways, which may result in high electroluminescence yield of the resulting devices. Hence, it is attempting to introduce benzotriazole into the central core to form an electron-deficient-core-based fused structure (DAD) for adjusting the optoelectronic properties of the resulting molecules, aiming for a small voltage loss and high performance in devices. By using DAD fused core one could also adopt a relatively planar structure rather than a twisted one and hence, facilitate the electron transfer from the donor to acceptor since the planarized DAD enhances the delocalization of π-electrons. More importantly, a low perturbation of electrons may occur in DAD fused core, which will result in efficient charge transfer[33]. In other words, π-orbital electrons are less likely to be trapped while passing through the fused π-bridge upon introduction of the triazole in this fused system[34].

In this chapter, a certified high efficiency of single-junction OPVs based on two fused-ring NFA molecules (Y1 and Y2) consisting of dithienothiophen[3,2-b]pyrrolobenzotriazole (BZPT) group with non-halogenated dicyanomethylene derivatives (INIC or INTC) will be introduced. A simple design strategy of covalent nitrogen bridge with adjacent thieno[3,2-b]thiophene and benzotriazole makes it possible to delicately tune the optoelectronic properties of target molecules, resulting in an improvement of optical coverage of near-infrared region (NIR) spectrum. A

commercial donor polymer PBDB-T[35] is selected because of its negligible band offsets with Y1 and Y2. In spite of this small energetic offset, which results in relatively high electroluminescence quantum efficiency (EQE$_{EL}$) (approximately 0.5 $\times 10^{-4}$) and small voltage losses, charge separation is still efficient and offers decent short-circuit current density (over 22 mA cm^{-2}), resulting in PCEs of over 13.4% (13.42 % for Y1 and 13.40 % for Y2). These devices have been certified at the photovoltaic Lab of Newport Corporation, showing a 12.6 % efficiency, which is the high efficiency of current single-junction organic cells meeting the ISO 17025 Standards reported so far. This remarkable feature of the presented fused benzotrizole-based system serves as an inspiration to design next-generation NFAs for high performance organic photovoltaics.

6.1 Characterization of non-fullerene acceptors

To meet the rules mentioned above, our molecule design rational consists of tuning the HOMO levels relatively close to that of the donor and, meanwhile, lowering the LUMO levels to make the absorption spectra of donor material and acceptor materials complementary:

(1) Introducing the nitrogen atoms in the center core unit serve as heteroatomic bridges for covalent planarization[36]: this provides stronger electron-donating character and allow for charge carrier mobility in contrast to cyclopentadiene (the center structural unit of the IDTT)[37, 38], thus increasing the HOMO energy levels;

(2) Adding a weak electron-withdrawing moiety of 2-ethylhexyl-benzo[d]-[1,2,3]-triazoles segment[39] in the middle of the central core to form a fused DAD structure: this helps to improve the efficient radiative recombination pathway and enhance the electroluminescence yield of the single components. Based on such a rationale, we are expecting a minimized voltage loss, which enables a high open-circuit voltage and high short-circuit current at the same time.

From the materials design point of view, in contrast to previous works[39], we increase the

central fused rings from pentacyclic to heptacyclic, and successfully tune the HOMO energy level to match a small band offset with the PBDB-T, meeting the requirement of the first design rule. In addition, we introduce benzotriazole unit in central core to increase the electroluminescence yield of both the single component, meeting the requirement of the second design rule. From the materials synthesis point of view, the central core that must be sterically hindered to prevent over aggregation[19] while maintaining an intramolecular charge transport channel is assumed by the alkyl side chains onto the nitrogen atoms[40]. In contrast to previous designs, it does not need to synthesize spiro-like structures, and this is a good example of non-spiro like molecule that show excellent performance as a non-fullerene acceptor. The chemical structures of Y1 and Y2 are depicted in Figure 6.1(a). Both, Y1 and Y2, can be easily solubilized in common organic solvents, such as chloroform and chlorobenzene at room temperature. Thermogravimetric analysis indicated that Y1 and Y2 exhibit excellent thermal stability with decomposition temperatures at 350 $^{\circ}$C.

Figure 6.1(b) shows the normalized absorption spectra of Y1 and Y2 in solution (chloroform) and in thin films. For the thin films, the absorption peak red-shifts from 738 to 802 nm for Y1 and 758 to 827 nm for Y2. The optical gap of pure the Y2 film estimated from the intersection between absorption and emission is about 1.40 eV, which is lower than that of the pure Y1 (1.44 eV). Cyclic voltammetry (CV) measurements were employed to evaluate the electrochemical properties, showing similar HOMO levels of -5.45 eV for Y1 and -5.43 eV for Y2 due to the identical core center, and a lower LUMO level for Y2 (-4.04 eV compared with -3.95 eV for Y1) due to the stronger electron-withdrawing character of INTC compared with that of INIC. As shown in Figure 6.1 (c), although the ΔHOMO offset between the PBDB-T donor and Y1 or Y2 appears to be small (0.07 eV for PBDB-T:Y1 and 0.05 eV for PBDB-T:Y2), efficient charge separation can still be achieved at the bulk heterojunction (BHJ) interface, meanwhile, with suppressed voltage losses.

This will be discussed in detail in voltage losses section (Chapter 6.3).

6.2 Device performance of OPVs

OPVs were fabricated with an inverted device structure of ITO/ZnO/active layer/MoO$_3$/Ag, where PBDB-T was chosen as the donor material. The donor/acceptor ratios in the active layer were carefully optimized. Figure 6.2(a) shows the current density versus voltage (*J-V*) characteristics under the illumination of AM 1.5 G, 100 mW cm^{-2}. Table 6.1 collects the photovoltaic parameters of these OPV devices based on Y1 and Y2, respectively. Meanwhile, statistical diagram of efficiency of PBDB-T:Y1 and :Y2 in Figure 6.2(c). Both BZPT-based non-fullerene acceptors, Y1 and Y2, exhibited J_{SC} over 22.0 mA cm^{-2} and resulted in PCEs of over 13 % (13.42 % for Y1 and 13.40 % for Y2, respectively). In Figure 6.2(b), the external quantum efficiency (EQE) spectra for Y1-based and Y2-based devices demonstrated similar shapes, while the Y2-based device displayed a 25 nm red-shift photocurrent response compared with that of Y1, which was in agreement with the trend of their absorption spectra. For devices with best *I-V* performance, the integrated J_{SC} values from EQE spectra with AM 1.5 G reference spectrum of PBDB-T:Y1 and PBDB-T:Y2 were calculated to be 22.14 mA cm^{-2} and 23.18 mA cm^{-2}, respectively, consistent with the J_{SC} values obtained from the *J-V* curves. Although some previous reports achieved similarly low voltage losses, none of them could keep 60-70% EQE from almost 400 nm to 860 nm[41, 42], which result in the high J_{sc} and high PCE of Y1-based and Y2-based devices.

In order to carefully evaluate the PCE, OPVs based on the PBDB-T:Y1 blend were sent to the PV calibration Lab of Newport Corporation, accredited by A2LA to ISO 17025 Standards, for certification measurements. With the current-voltage parameters shown in Figure 6.2(d) and Table 6.1, detailed measurements can be found in the section of Methods (Fabrication and measurement

of devices). An efficiency of 12.6% was certified with J_{SC} of 21.55 mAcm^{-2}, a V_{OC} of 0.88 V and an FF of 66.3%. The certification confirmed that OPV devices can indeed endure the standard measurement and achieve results relatively close to our regular testing, indicating a reliable and reproducible high performance of our systems (National Renewable Energy Laboratory "Best Research-Cell Efficiencies" chart, July 2018).

6.3 Voltage losses and charge separation

In order to evaluate the voltage loss in our system and unravel the nature of its high photovoltaic performance, we investigated voltage losses in both solar cells. The calculated results are presented in Table 6.2. The total energy loss (ΔE) was defined as the difference between the optical gap of blend solar cell and the V_{OC}. As shown in Table 6.2, ΔE is 0.57 eV for both systems. Specification of the three sources of V_{OC} loss follows the equations below:

$$\Delta E = E_g - qV_{OC} = \left(E_g - qV_{OC}^{SQ}\right) + \left(qV_{OC}^{SQ} - qV_{OC}^{rad}\right) + \left(qV_{OC}^{rad} - qV_{OC}\right)$$

$$= \left(E_g - qV_{OC}^{SQ}\right) + q\Delta V_{OC}^{rad,below\,gap} + q\Delta V_{OC}^{non-rad}$$

$$= \Delta E_1 + \Delta E_2 + \Delta E_3$$

The ΔE_1 is the difference between optical gap and maximum voltage based on the Shockley-Queisser limit (SQ limit), caused by radiative recombination originating from the absorption above the optical gap, typically 0.25 eV or above, unavoidable for any kind of solar cells. Here, qV_{OC}^{SQ} is the maximum voltage based on the SQ limit, where the EQE is assumed to be 1 above the gap and 0 below the optical gap[43] and the only loss is from the mismatch between radiation received in a narrow solid angle from the sun and omnidirectoinal radiative recombination. Radiative-recombination loss (ΔE_2) is due to absorption below the optical gap. Here, V_{OC}^{rad} is the open-circuit voltage when there is only radiative recombination, including both the radiative loss mentioned in ΔE_1 and the additional radiative recombination from the absorption below the optical gap due to the

92

non-step function absorption. For solar cells with steep absorption edges, like inorganic or perovskite solar cells, this term is negligible. However, this part can be very high for OPVs, especially for those with obvious charge-transfer-state absorption. While in our case, the absorption onset of BHJ devices is sharp (Figure 6.3(a)), leading to $q\Delta V_{OC}^{rad,below\ gap}$ estimated as low as 0.04 eV and 0.05 eV, significantly smaller than that observed in typical OPVs and even most small-offset OPVs (Supplementary Table B3). The final part of energy loss stem from the non-radiative recombination (ΔE_3) and could be directly obtained from the equation: $\Delta V_{OC}^{non-rad} = \frac{kT}{q} \ln \left(\frac{1}{EQE_{EL}} \right)$. EQE_{EL} results are shown in Figure 6.3(b). It is notable that both systems shown low non-radiative losses of 0.25 eV and 0.26 eV respectively, which is very low among OPVs reported with such high efficiency.

We also investigated the PLQY and PL quenching for the blend films. Following our previous publication, we blend the insulating polymer polystyrene (PS) with the acceptor materials, to mimic the dispersed morphology in the active layer of the devices[23]. The PLQY values of PS:Y1 and PS:Y2 blends are 5.8% and 3.4% respectively; while those of the PBDB-T:Y1 and PBDB-T:Y2 are 0.1% and 0.3%, indicating efficient PL quenching. The corresponding PLQY data are summarized in Supplementary Table B4. Although efficient PL quenching indicates efficient charge separation, it also implies additional non-radiative recombination losses, which are to be further decreased. In an ideal case, the PL quenching is expected to happen at the short-circuit conditions, rather than the open-circuit conditions. Efficient PL quenching is further confirmed by the PL decay measurements (Figure 6.3(c, d)), which show shortening of the PL lifetime in the active layers for both Y1 and Y2 blends. Consistent with our and other's previous reports[23, 44], the timescale on which the PL quenching occurs is very slow compared with traditional fullerene-based devices (those with large energetic offset between the donor and acceptor materials).

6.4 Film morphologies

The molecular packing characteristics of Y1 and Y2 in thin film blend with polymer PBDB-T were investigated using grazing incidence wide-angle X-ray scattering (GIWAXS) [45]. PBDB-T:Y1 and PBDB-T:Y2 blends show similar molecular packing shown in Figure 6.4(a, b). In both blends, a broad peak corresponding to the π-π stacking was observed along the out-of-plane direction at $q=1.7$ Å^{-1}, which benefit efficient photon absorption and charge transport.

The morphologies were further investigated by atomic force microscopy (AFM, Figure 6.4 (c, d)) and transmission electron microscopy (TEM, Figure 6.4 (e, f)). The formation of obvious ordered nano-fibrillar structures of active layer films were observed using AFM, accompanied with a smooth root-mean-square roughness (R_q) of 1.22 nm and 1.60 nm on a scan area of 1 μm × 1 μm for Y1- and Y2-based blends, respectively. The phase separation was further visualized using TEM with suitable domain sizes in both blends, indicating an ideal phase separation for the optimized balance between charge transportation pathway and interface recombination. As a consequence of the orientation, both polymer and non-fullerene molecules in the active layer are observed to closely stack. The lateral charge transportation was also proven to be efficient with space charge limited current (SCLC) method[46], with the average hole and electron mobilities calculated. Hole mobilities of the PBDB-T:Y1 and PBDB-T:Y2 blend films were measured to be $1.56×10^{-3}$ cm^2·V^{-1}·s^{-1} and $2.59×10^{-3}$ cm^2·V^{-1}·s^{-1}, respectively, and electron mobilities were measured to be $3.04×10^{-4}$ cm^2·V^{-1}·s^{-1} and $2.08×10^{-4}$ cm^2·V^{-1}·s^{-1}, respectively. These results reflect that the morphology of this system is efficient for charge transport.

6.5 Conclusion

In summary, two NIR-absorbing multifused benzotrizole-based NFAs, Y1 and Y2 were introduced. By blending with a commercialized donor PBDB-T, they can achieve a high PCE of

13.42 % and 13.40 %, respectively. The high performance was enabled by the relatively high EQE$_{EL}$ of approximately 0.5×10^{-4}, which indicates low non-radiative recombination loss of the blend. In addition, despite small donor-acceptor energy offsets, highly efficient charge generation efficiencies have been shown for both PBDB-T:Y1 and PBDB-T:Y2 blend films. Moreover, a homogeneous and nanophase-segregated structure with an optimized size and preferred orientation are also observed in blend films, which contributed to the efficient charge separation and transport. These results are achieved using a simple design strategy by incorporation of nitrogen acting as a bridging atom between adjacent electron-donor (thieno[3,2-*b*]thiophene) segment and weak electron-deficient segment (benzotriazole) (DAD fused core), leading to strong absorption in *vis*−NIR region. A certified high efficiency of single-junction OPVs meeting the ISO 17025 Standards was achieved at 12.6% based on PBDB-T:Y1 devices. This work provides a rational route to a delicate design with relatively tight spacing using the benzotrizole-based DAD structure as central core towards high performance NFAs.

6.6 Reference

1.   Yu, G., Gao, J., Hummelen, J.C., Wudl, F. & Heeger, A.J. Polymer photovoltaic cells: enhanced efficiencies via a network of internal donor-acceptor heterojunctions. *Science* **270**, 1789-1791 (1995).

2.   Halls, J.J.M., Pichler, K., Friend, R.H., Moratti, S.C. & Holmes, A.B. Exciton diffusion and dissociation in a poly(*p*- phenylenevinylene)/C60 heterojunction photovoltaic cell. *Appl. Phys. Lett.* **68**, 3120-3122 (1996).

3.   Li, G., Zhu, R. & Yang, Y. Polymer solar cells. *Nat. Photon.* **6**, 153-161 (2012).

4.   Lu, L. et al. Recent Advances in Bulk Heterojunction Polymer Solar Cells. *Chem. Rev.* **115**, 12666-12731 (2015).

5.   Vohra, V. et al. Efficient inverted polymer solar cells employing favourable molecular orientation. *Nat.Photon.* **9**, 403-408 (2015).

6.   Li, Y. Molecular design of photovoltaic materials for polymer solar cells: toward suitable electronic energy levels and broad absorption. *Accounts Chem. Res.* **45**, 723-733 (2012).

7.   Kaltenbrunner, M. et al. Ultrathin and lightweight organic solar cells with high flexibility. *Nat. comm.* **3**, 770 (2012).

8.   Li, G. et al. High-efficiency solution processable polymer photovoltaic cells by self-organization of polymer blends. *Nat. Mater.* **4**, 864-868 (2005).

9.   Brabec, C.J., Heeney, M., McCulloch, I. & Nelson, J. Influence of blend microstructure on bulk heterojunction organic photovoltaic performance. *Chem. Soc. Rev.* **40**, 1185-1199 (2011).

10.   Peet, J., Heeger, A.J. & Bazan, G.C. "Plastic" solar cells: self-assembly of bulk heterojunction nanomaterials by spontaneous phase separation. *Accounts Chem. Res.* **42**, 1700-1708 (2009).

11.   Svensson, M. et al. High performance polymer solar cells of an alternating polyfluorene copolymer and a fullerene derivative. *Adv. Mater.* **15**, 988-991 (2003).

12.   Liu, J. et al. Fast charge separation in a non-fullerene organic solar cell with a small driving force. *Nat. Energy* **1**, 16089 (2016).

13.   Yao, J. et al. Quantifying Losses in Open-Circuit Voltage in Solution-Processable Solar Cells. *Phys. Rev. Appl.* **4**, 014020 (2015).

14.   Dang, M.T., Hirsch, L. & Wantz, G. P3HT:PCBM, Best Seller in Polymer Photovoltaic Research. *Adv. Mater.* **23**, 3597-3602 (2011).

15.   Linderl, T. et al. Energy Losses in Small-Molecule Organic Photovoltaics. *Adv. Energy Mater.* **7**, 1700237 (2017).

16.   Benduhn, J. et al. Intrinsic non-radiative voltage losses in fullerene-based organic solar cells. *Nat. Energy* **2**, 17053 (2017).

17.   Vandewal, K., Tvingstedt, K., Gadisa, A., Inganäs, O. & Manca, J.V. Relating the open-circuit voltage to interface molecular properties of donor:acceptor bulk heterojunction solar cells. *Phys. Rev. B* **81**, 125204 (2010).

18.   Würfel, P. & Würfel, U. Physics of solar cells: from basic principles to advanced concepts. (John Wiley & Sons, 2009).

19.   Zhang, G. et al. Nonfullerene Acceptor Molecules for Bulk Heterojunction Organic Solar Cells. *Chem. Rev.* **118**, 3447-3507 (2018).

20. Vandewal, K. et al. Efficient charge generation by relaxed charge-transfer states at organic interfaces. *Nat. Mater.***13**, 63-68 (2014).

21. Vandewal, K., Tvingstedt, K., Gadisa, A., Inganäs, O. & Manca, J.V. On the origin of the open-circuit voltage of polymer–fullerene solar cells. *Nat. Mater.* **8**, 904-909 (2009).

22. Burke, T.M., Sweetnam, S., Vandewal, K. & McGehee, M.D. Beyond Langevin Recombination: How Equilibrium Between Free Carriers and Charge Transfer States Determines the Open-Circuit Voltage of Organic Solar Cells. *Adv. Energy Mater.* **5**, 1500123 (2015).

23. Qian, D. et al. Design rules for minimizing voltage losses in high-efficiency organic solar cells. *Nat. Mater.* **17**, 703 (2018).

24. Yan, C. et al. Non-fullerene acceptors for organic solar cells. *Nat. Rev. Mater.* **3**, 18003 (2018).

25. Cheng, P., Li, G., Zhan, X. & Yang, Y. Next-generation organic photovoltaics based on non-fullerene acceptors. *Nat.e Photon.* **12**, 131-142 (2018).

26. Fei, Z. et al. An Alkylated Indacenodithieno[3,2-b]thiophene-Based Nonfullerene Acceptor with High Crystallinity Exhibiting Single Junction Solar Cell Efficiencies Greater than 13% with Low Voltage Losses. *Adv. Mater.* **30**, 1705209 (2018).

27. Jiang, W. et al. Ternary Nonfullerene Polymer Solar Cells with 12.16% Efficiency by Introducing One Acceptor with Cascading Energy Level and Complementary Absorption. *Adv. Mater.* **30,** 1703005 (2017).

28. Li, T. et al. Fused Tris(thienothiophene)-Based Electron Acceptor with Strong Near-Infrared Absorption for High-Performance As-Cast Solar Cells. *Adv. Mater.* **30**, 1705969 (2018).

29. Kaya, E., Balan, A., Baran, D., Cirpan, A. & Toppare, L. Electrochromic and optical studies of solution processable benzotriazole and fluorene containing copolymers. *Org. Electron.* **12**, 202-209 (2011).

30. Chen, X., Jin, Q., Wu, L., Tung, C. & Tang, X. Synthesis and unique photoluminescence properties of nitrogen-rich quantum dots and their applications. *Angew. Chem. Int. Edit.* **53**, 12542-12547 (2014).

31. Banal, J.L. et al. Electron deficient conjugated polymers based on benzotriazole. *Polym. Chem.* **4**, 1077-1083 (2013).

32. Ghosh, S., Bedi, A. & Zade, S.S. Thienopyrrole and selenophenopyrrole donor fused with benzotriazole acceptor: microwave assisted synthesis and electrochemical polymerization. *RSC Adv.* **5**, 5312-5320 (2015).

33. Li, P., Wang, Z., Song, C. & Zhang, H. Rigid fused π-spacers in D–π–A type molecules for dye-sensitized solar cells: a computational investigation. *J. Mater. Chem. C* **5**, 11454-11465 (2017).

34. Hosseinzadeh, E. & Hadipour, N.L. The influence of the structural variations of the fused electron rich-electron deficient unit in the π-spacer of A-D-π-D-A organic dyes on the efficiency of dye-sensitized solar cells: A computational study. *Org. Electron.* **62**, 43-55 (2018).

35. Zhao, W.; Qian, D.; Zhang, S.; Li, S.; Inganas, O.; Gao, F.; Hou, J., Fullerene-Free Polymer Solar Cells with over 11% Efficiency and Excellent Thermal Stability. *Adv. Mater.* **28**, 4734-9 (2016).

36. Cheng, Y.J. et al. Thieno[3,2-b]pyrrolo donor fused with benzothiadiazolo, benzoselenadiazolo and quinoxalino acceptors: synthesis, characterization, and molecular properties. *Org. Lett.* **13**, 5484-5487 (2011).

37. Lin, Y. et al. An electron acceptor challenging fullerenes for efficient polymer solar cells. *Adv. Mater.* **27**, 1170-1174 (2015).

38. Zhang, Y. et al. Conjugated polymers based on C, Si and N-bridged dithiophene and thienopyrroledione units: synthesis, field-effect transistors and bulk heterojunction polymer solar cells. *J. Mater. Chem.* **21**, 3895 (2011).

39. Feng, L. et al. Thieno[3,2-b]pyrrolo-Fused Pentacyclic Benzotriazole-Based Acceptor for Efficient Organic Photovoltaics. *Acs Appl. Mater. Interfaces* **9**, 31985-31992 (2017).

40. Hou, J.; Inganas, O.; Friend, R. H.; Gao, F., Organic solar cells based on non-fullerene acceptors. *Nat. Mater.* **17**, 119-128 (2018).

41. Liu, X. et al. Efficient Organic Solar Cells with Extremely High Open-Circuit Voltages and Low Voltage Losses by Suppressing Nonradiative Recombination Losses. *Adv. Energy Mater.* **8**, 1801699 (2018).

42. Nikolis, V.C. et al. Reducing Voltage Losses in Cascade Organic Solar Cells while Maintaining High External Quantum Efficiencies. *Adv. Energy Mater.* **7**, 1700855 (2017).

43. Clarke, T.M. & Durrant, J.R. Charge photogeneration in organic solar cells. *Chem. Rev.* **110**, 6736-6767 (2010).

44. Shockley, W. & Queisser, H.J. Detailed balance limit of efficiency of p-n junction solar cells. *J. Appl. Phys.* **32**, 510-519 (1961).

45.   Rivnay, J., Mannsfeld, S.C., Miller, C.E., Salleo, A. & Toney, M.F. Quantitative determination of organic semiconductor microstructure from the molecular to device scale. *Chem. Rev.* **112**, 5488-5519 (2012).

46.   Malliaras, G., Salem, J., Brock, P. & Scott, C. Electrical characteristics and efficiency of single-layer organic light-emitting diodes. *Phys. Rev. B* **58**, R13411 (1998).

47.   Wang, Y., et al. Optical gaps of organic solar cells as a reference for comparing voltage losses. *Adv. Energy Mater.* **8,** 1901352 (2018)

Figure 6.1 Molecular structure and properties. (a) Chemical structure of the acceptor molecules. **(b)** Normalized absorption spectra of the acceptors Y1 and Y2. **(c)** energy diagrams of the materials used in OPVs.

Figure 6.2 Photovoltaic performance. (**a**) The J-V curves of PBDB-T:Y1 and :Y2 blend solar cells. (**b**) The EQE curves of PBDB-T:Y1 and :Y2 blend solar cells. (**c**) Statistical diagram of efficiency of PBDB-T:Y1 and :Y2. (**d**) Current-voltage parameters of PBDB-T:Y1 device certified (0.0548 cm2 device area) by Newport Corp.

Figure 6.3 Optical and electrical characterizations. (a) Fourier-transform photocurrent spectroscopy (FTPS) of PBDB-T:Y1 and Y2 blend solar cell. **(b)** The electroluminescence quantum efficiency of PBDB-T:Y1 and PBDB-T:Y2 blend solar cells at different injected currents. **(c, d)** Time-resolved PL for D:A blends and polystyrene (PS) blends. Black solid curves are fitting curves for extracting the lifetime ($\tau_{av} = \frac{\Sigma A_i \tau_i^2}{\Sigma A_i \tau_i}$).

Figure 6.4 Film morphology of blend films. **(a-c)** PBDB-T:Y1 films (a) Two-dimensional GIWAXS image (b), AFM image, and (c) TEM image; **(d-f)** PBDB-T:Y1 films (d) Two-dimensional GIWAXS image (e), AFM image, and (f) TEM image.

Table 6.1 Photovoltaic performances of PBDB-T:Y1 and PBDB-T:Y2 based OPV devices

Devices[a]	V_{OC} (V)	J_{SC} (mA cm^{-2})	FF (%)	PCE (%)
PBDB-T:Y1	0.87 (0.87 ± 0.01)	22.44 (21.68 ± 1.07)	69.1 (70.12 ± 0.82)	13.42 (13.22 ± 0.35)
PBDB-T:Y2	0.82 (0.81 ± 0.01)	23.56 (23.12 ± 0.78)	69.4 (70.80 ± 0.70)	13.40 (13.25 ± 0.39)
PBDB-T:Y1[*]	0.88 ± 0.01	21.55 ± 0.46	66.3 ± 0.80	12.56 ± 0.33

a, Certification measurement results are marked with "*".

Table 6.2 V_{OC} loss profile of PBDB-T:Y1- and PBDB-T:Y2-based OPV devices

Devices[a]	E_g (eV)	qV_{OC}^{SQ} (eV)	qV_{OC}^{rad} (eV)	ΔE (eV)	ΔE_1 $E_{gap} - qV_{OC}^{SQ}$ (eV)	ΔE_2 $q\Delta V_{OC}^{rad, below\ gap}$ (eV)	ΔE_3 $q\Delta V_{OC}^{non-rad}$ (eV)
PBDB-T:Y1	1.44	1.17	1.12	0.57	0.27	0.05	0.25
PBDB-T:Y2	1.40	1.13	1.09	0.57	0.27	0.04	0.26

Appendix A. Supplementary Texts

Supplementary Text A2.1 Density functional theory (DFT) Calculations

Density functional theory calculations were performed using Vienna ab-initio simulation package (VASP) code[1]. The revised Perdew-Burke-Ernzerhof generalized gradient approximation (PBEsol)[2,3] method was used for exchange-correlation functional including the dispersion corrections to the total energies using Grimme's DFT-D3 scheme[4,5]. The core-valence interactions were treated by the projected augmented wave (PAW) pseudopotentials[6]. Plane-wave energy cut-off was set to 400 eV and 4×4×1 Γ-centered k-point mesh was used for Brillouin-zone sampling. During the optimization, the positions of the atoms and the volume of the unit cell were allowed to relax using a conjugate gradient algorithm until all Hellman-Feynman forces on all atoms were less than 0.08 eV/Å with an energy convergence of 1×10^{-4} eV. The surfaces were modeled by a slab consisting of 2×2 periodicity in the a-b plane and four atomic layers along the c axis, separated by 11-18 Å of vacuum in the surface normal direction. The interaction energies are calculated using the following equation:

$$\Delta E_{int}^q = E_{comp.} - [E_d^q + \sum n_i\mu_i + \Delta q(\epsilon_F + E_{vbm})] \tag{1}$$

which includes possible "charged" defect and anion (cation) interactions. Here, $E_{comp.}$ is the energy of the slab complex, E_d^q is the energy of the defective "d" surface with charge-state "q". n_i is the number of the ith anion (cation) added to the surface and μ_i is the corresponding chemical potential. Δq is the number of charges exchanged (with fermi energy ϵ_F measured from E_{vbm}) exchanged between system and reservoir in order to form the charged defect. Here, the chemical potential can be explicitly written as $\mu_i = \mu_{0i} + \Delta\mu_i$, where $\Delta\mu_i$ is the shift in the chemical potential depending on the growth conditions and $\mu_{0i} = E(i)$ is the intrinsic chemical potential (i.e., free of the growth conditions). We define fluoride (F) or PEA attachment to a neutral defect as:

$$\Delta E_{int}^0 = E_{comp.} - [E_d^0 + \mu_x] \tag{2}$$

where, $x = \{F, PEA\}$, and attachment of both F and PEA as:

$$\Delta E_{int}^0 = E_{comp.} - [E_d^0 + \mu_{PEA} + \mu_F] . \tag{3}$$

For the calculation of chemical potential of F and PEA, we used conditions that are more relevant to the systems we studied. First, to calculate the intrinsic chemical potential μ_{0F}, we used the reported orthorhombic crystal structure (see Supplementary Table B2.1) and then relaxed it using DFT and for μ_{0PEA}, we manually constructed a unit-cell and similarly relaxed using DFT. To calculate $\Delta\mu_F$ and $\Delta\mu_{PEA}$, as to be consistent with our experimental conditions, we considered that the former is the source of potassium fluoride (KF) and the latter is that of PEAI (I: iodide). Therefore, the following two relations should be satisfied:

$$\Delta\mu_K + \Delta\mu_F = \Delta H(KF) \tag{4}$$

$$\Delta\mu_{PEA} + \Delta\mu_I = \Delta H(PEAI) \tag{5}$$

We also tested the formation energy of the reported KF_2 phase and found that KF is more stable by roughly 0.5 eV. Here, the formation enthalpy of cubic KF and PEAI crystals are

calculated with respect to units of potassium (K), fluoride (F), PEA and iodide (I) in their crystal phases, as shown in Supplementary Table B2.1. In our study, we manually constructed and tested different possible crystal structure cases for PEA and PEAI. The resulting optimized crystal structures were either unstable, less-stable or the ammonium groups got deprotonated, except for the structures reported in Supplementary Table B2.1. Hence, we used those structure for further calculations, while other crystal structure arrangements did not significantly differ energetically (~0.2 eV).

Our computational results showed that $\Delta H(KF) = -5.49\ eV$ and $\Delta H(PEAI) = -3.32\ eV$. Here, $\Delta H(KF)$ value we found computationally is reasonably close to the solid-state value (-5.89 eV) of KF reported in NIST Webbook.[7] Next, in order to be consistent with experimental conditions in our study, we assumed an equipartition in the chemical potentials for both cases. Therefore, using Eq. (4)-(5) $\Delta\mu_F$ and $\Delta\mu_{PEA}$ were calculated to be -2.75 eV and -1.66 eV, respectively.

We found that the interaction energy of PEA attachment to neutral iodine-vacancy (V_I) is -1.07 eV and to neutral iodine-lead replacement (Pb_I) is -1.32 eV. Both F and PEA attachments to neutral V_I is -3.23 eV and to neutral Pb_I is -2.83 eV. We then calculated the ΔE_{int}^q in the case of charged defect cases (V_I^+ and Pb_I^+) and obtained the following plots for PEA, F and F/PEA attachments.

For each case, the stronger interaction energy between defects d^0, d^+ as a function of Fermi energy is shown. Thus, we found that for both V_I and Pb_I defects the fluoride binds relatively strongly, and attachment of PEA further increases interaction energy roughly by 2 eV. For low Fermi energy values (p-type region) F and PEA binds strongly to neutral defects, whereas they bind to positively charge defect more strongly in the high Fermi energy values (n-type region).

Supplementary Text A2.2 Bi-exponential model fitting of the TRPL results

The carrier lifetimes were obtained by fitting the TRPL data with a bi-exponential decay model:

$$I(t) = A_1 \exp(-\frac{x}{\tau_1}) + A_2 \exp(-\frac{x}{\tau_2}) \tag{S1}$$

$$\tau_{average} = A_1\tau_1 + A_2\tau_2 \tag{S2}$$

Supplementary Text A2.3 Measurements and analysis of the trap density of states

The trap density of states (tDOS) could be calculated based on the angular frequency dependent capacitance with the equation:

$$N_T(E_\omega) = -\frac{V_{bi}}{qW}\frac{dC}{d\omega}\frac{\omega}{kT} \tag{S3}$$

where C is the capacitance, ω is the angular frequency, q is the elementary charge, k is the Boltzmann constant, V_{bi} is the built-in potential, W is the depletion width, and T is the temperature.

The angular frequency needs to be further defined by:

$$E_\omega = kT \ln \frac{\omega}{\omega_0} \tag{S4}$$

where ω_0 is the attempt-to-escape frequency. The tDOS level could be calculated when combining both equations.

Supplementary Text A2.4 Determination of rear cells EQE and estimation of tandem efficiencies pared with record silicon/CIGS cells

We used an experimentally numerical estimation reported by Brabec et. al.[8] to assess the EQE responses of the rear cells. The method was to use the rear cell's own EQE spectrum and the transmission spectrum of the filtering front cell based on the equation:

$$EQE_{rear}^{filtered}(E) = T_{front}(E)EQE_{rear}(E) \qquad (S5)$$

Thus, the J_{SC} of the filtered rear cell could be obtained by solving:

$$J_{SC,rear}^{filtered} = q\int_0^\infty EQE_{rear}^{filtered}(E)\phi_{AM1.5G}(E)dE \qquad (S6)$$

In addition, due to the reduced light intensity exposed to the rear cell, which led to a reduced photocurrent, the splitting of quasi-fermi level of the rear cell would also be suppressed. As a result, its V_{OC} could be written as:

$$V_{OC,rear}^{filtered} = V_{OC,rear} + \frac{n_{id}kT}{q}\ln(\frac{J_{SC,rear}^{filtered}}{J_{SC,rear}}) \qquad (S7)$$

where $V_{OC, rear}$ is the original V_{OC} of the rear cell (either silicon or CIGS), n_{id} is the ideality factor of the photodiode, assumed to be unit in our calculation. The fill factor of the filtered cell was assumed to remain unaffected for these record PV cells. With the calculated parameters, one could easily obtain the estimated power conversion efficiency when any cell wanted to be used as a rear cell for four-terminal tandem devices. The overall tandem efficiency could thus be obtained by numerically adding up the measured semitransparent front cell efficiency and the calculated rear cell efficiency with filtration.

Supplementary Text A2.5 Calculation of efficiency loss and tandem efficiency with subcells with various V_{OC}

The efficiency loss was denoted by subtracting the SQ efficiency with the calculated efficiency when V_{OC} loss ($V_{OC, SQ}$ - V_{OC}) varies. The parasitic loss in fill factor was neglected in this calculation, which would always worsen the device performance in our calculation and not necessarily affect the concept we are delivering this in figure. Similarly, the FF was assumed to be identical as it's ideal value and the V_{OC} of subcells were assumed to be the only variables for both subcells.

Supplementary Text A2.6 Supplementary References

[1]   G. Kresse, J. Furthmüller, Comput. Mater. Sci. 1996, 6, 15.

[2]   J. P. Perdew, K. Burke, M. Ernzerhof, Phys. Rev. Lett. 1996, 77, 3865.

[3]   J. P. Perdew, A. Ruzsinszky, G. I. Csonka, O. A. Vydrov, G. E. Scuseria, L. A. Constantin, X. Zhou, K. Burke, Phys. Rev. Lett. 2008, 100, 136406.

[4]   S. Grimme, J. Antony, S. Ehrlich, H. Krieg, J. Chem. Phys. 2010, 132, 154104.

[5]   S. Grimme, J. Comput. Chem. 2006, 27, 1787.

[6]   P. E. Blöchl, Phys. Rev. B 1994, 50, 17953.

[7]   W. G. M. Sharon G. Lias, John E. Bartmess, Joel F. Liebman, John L. Holmes, Rhoda D. Levin, In National Institute of Standards and Technology, Gaithersburg MD 20899, 2018.

[8]   T. Kirchartz, S. Korgitzsch, J. Hüpkes, C. O. R. Quiroz, C. J. Brabec, ACS Energy Lett. 2018, 3, 1861.

[9]   K. Yoshikawa, H. Kawasaki, W. Yoshida, T. Irie, K. Konishi, K. Nakano, T. Uto, D. Adachi, M. Kanematsu, H. Uzu, K. Yamamoto, Nat. Energy 2017, 2, 17032.

[10]   M. A. Green, E. D. Dunlop, D. H. Levi, J. Hohl-Ebinger, M. Yoshita, A. W. Y. Ho-Baillie, Prog. Photovoltaics Res. Appl. 2019, 27, 565.

Supplementary Text A3.1 Grazing Incidence X-ray Diffraction penetration depth estimation

The penetration depths were estimated based on the equation:[1]

$$G = \frac{\int_{x=0}^{x=x} dI_D}{\int_{x=0}^{x=\infty} dI_D} = 1 - exp\left\{-\mu x\left(\frac{1}{sin\gamma} + \frac{1}{sin\beta}\right)\right\}$$

where x is the penetration depth, γ is the incident beam angle, β is the exit beam angle, μ is the mass absorption coefficient (207 $cm^2\,g^{-1}$ for $FAPbI_3$) and G is a constant with value 0.95. The above equation is solved to give the penetration depth x.

Supplementary Text A3.2 Supplementary References

1. Cullity, B.D., and Stock, S.R. (2001). Elements of X-Ray Diffraction, 3rd Edition, Ch. 4-10, Ch. 14-5.

2. Kato, M., Fujiseki, T., Miyadera, T., Sugita, T., Fujimoto, S., Tamakoshi, M., Chikamatsu, M., and Fujiwara, H. (2017). Universal rules for visible-light absorption in hybrid perovskite materials. J. Appl. Phys. *121*, 115501.

Supplementary Text A4.1 Discussion on XRD results for FAMACs and FACs-based perovskites

High-resolution XRD measurements were carried out for both the FAMACs and FACs-based perovskites. The as-cast and fully annealed films with both tri-iodide and mixed-halide compositions were measured and shown in **Figure C4.1** and **C4.2**. The diffraction intensity was also extracted for the (001) perovskite peak and the PbI_2 peak. In both the FAMACs and FACs systems, the mixed-halide films exhibited larger 2θ peak positions compared with the tri-iodide ones, which correspond to smaller lattice constants. Meanwhile, the film crystallinity of the mixed-halide films was apparently weaker, potentially due to the homogenization process, because the pure tri-bromide films exhibited superior crystallinity by itself (see discussions below). The PbI_2 characteristic peak (or more accurately, the PbX_2 peak in the mixed-halide case) was only detected in the fully annealed films and was much stronger in the mixed-halide case. From the SEM images of the fully annealed films in **Figure C4.4**, we also observed large amounts of plate-like crystalline PbI_2 at the surface of $FAMACsPb(I_{0.8}Br_{0.2})_3$. Considering that all films were prepared by the exact same deposition process, we speculate that the organic A-site cations were less stable and decomposed to form the residual lead halide binaries during thermal annealing for the mixed-halide films.

Supplementary Text A4.2 Discussion on XRD results for $MAPb(I_XBr_{1-X})_3$, $FAPb(I_XBr_{1-X})_3$, $FAPb(I_XBr_{1-X})_3$ with MACl, $FAMACsPb(I_XBr_{1-X})_3$, and $FACsPb(I_XBr_{1-X})_3$.

High-resolution XRD measurements were carried out for $MAPb(I_XBr_{1-X})_3$ perovskites (where X= 1, 0, 0.9, 0.8 or 0.5 for $MAPbI_3$, $MAPbBr_3$, $MAPb(I_{0.9}Br_{0.1})_3$, $MAPb(I_{0.8}Br_{0.2})_3$, and $MAPb(I_{0.5}Br_{0.5})_3$, respectively) in order to completely exclude any effects by the cations and MACl, even though MA-based perovskites are not the optimum composition to achieve high performance

WBG mixed-perovskite PVs. The MA-based films are deposited following the same solvent combination (DMF/DMSO = 80/20) and antisolvent deposition methods as the FAMACs perovskites. It should also be noted that the cation could tremendously affect the growth pathway also, for example, $MAPbI_3$ will form a robust $MAI-DMSO-PbI_2$ intermediate phase before annealing, but the perovskite phase remains dominant in the as-cast films of the FAMACs and FACs systems (especially for tri-iodide perovskites). The diffraction peaks at the 2θ range of $13.5°$ to $15.5°$ was extracted and shown in **Figure C4.8** for the as-cast films, pre-annealed films ($65°C$ for 1 min), and fully annealed films ($100°C$ for 10 min).

The (110) peak for $MAPbI_3$ and the (100) peak for $MAPbBr_3$ are easily identified in **Figure C4.5A** and **C4.5B** at $14.2°$ and $14.9°$, respectively. The peak intensity is extremely low for the as-cast $MAPbI_3$ film because of the dominant $MAI-DMSO-PbI_2$ intermediate phase at this stage. The diffraction peaks for $MAPbI_3$ shifted negligibly during their perovskite growth when comparing the as-cast film, pre-annealed film, and the fully annealed film. In contrast, $MAPbBr_3$ showed very strong crystallinity even without any heat treatment, consistent with our DFT results that their formation is thermodynamically favored. In all mixed-halide cases, we observed dramatic shifting of their 2θ peak positions towards lower values, indicating that there is a clear Br% change during perovskite growth.

Similar to $MAPb(I_XBr_{1-X})_3$, we have also characterized $FAPb(I_XBr_{1-X})_3$ (in the case with or without MACl additive, **Figure C4.6** and **C4.7**) to show these observations were not limited to MA systems. However, we found except for FAPbBr3, MACl is essential for $FAPbX_3$-based compositions to form their a-phase at lower temperature as no diffraction signals from the (100) perovskite peak of $FAPbX_3$ could be observed before annealing at $150 °C$. Interestingly, adding MACl directly assisted the formation of the α-phase perovskite, but a segregated growth feature

was still observed and more severe than the MA system such as $FAPb(I_{0.8}Br_{0.2})_3$, in which homogeneous halide merely formed after full annealing.

MACl is another factor that need to be excluded to confirm the existence of homogenization process. We further characterized $FAMACsPb(I_XBr_{1-X})_3$ and $FACsPb(I_XBr_{1-X})_3$ (without MACl, additive, **Figure C4.8** and **C4.9**) films, where only two halides were involved. Similarly, the shifting of perovskite (100) peak from a higher 2θ to a lower 2θ was again observed, which suggested the existence of the halide homogenization process without MACl. Segregated phases were observed for fully annealed $FAMACsPb(I_{0.5}Br_{0.5})_3$ and $FAMACsPb(I_{0.5}Br_{0.5})_3$ films here, indicating MACl could be helpful assist the formation of homogeneous films during annealing.

Supplementary Text A4.3 Discussion on in-situ PL results for FACs-based perovskites

The in-situ PL measurements were carried out for the FACs-based perovskites. The complete contour plots during both the spin-coating and annealing periods are shown in **Figure C4.13**, and the extracted parameters (peak position, intensity, FWHM) in **Figure C4.14**.

Both the peak position shifts and the time elapsed before the peak intensity and FWHM stabilize showed consistent trends with the $FAMACsPbX_3$ perovskites. For $FA_{0.8}Cs_{0.2}Pb(I_{0.83}Br_{0.17})_3$, the peak shift was observed to be $\Delta E_1 = 0.246$ eV during spin-coating and $\Delta E_2 = 0.095$ eV during annealing. For $FA_{0.8}Cs_{0.2}PbI_3$, these values were as low as $\Delta E_1 = 0.176$ eV and $\Delta E_2 = 0.054$ eV. Similar to the results for the $FAMACsPbX_3$ perovskites, the energy shift is larger with Br inclusion. The excess growth stage is still observed and can be quantified by a biexponential decay model ($t_1 = 11.81$s, $t_2 = 35.70$s for $FA_{0.8}Cs_{0.2}Pb(I_{0.83}Br_{0.17})_3$, and $t_1 = t_2 = 20.20$ s for $FA_{0.8}Cs_{0.2}PbI_3$). That it is less apparent than the $FAMACsPbX_3$ perovskites might be attributed the incorporation of MA to further assist the process originated from Br% addition.
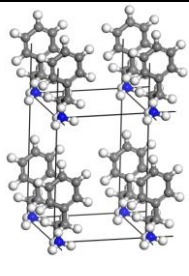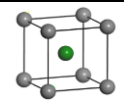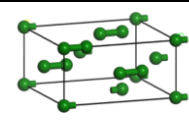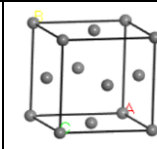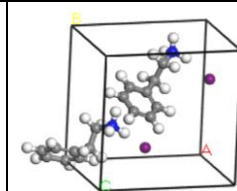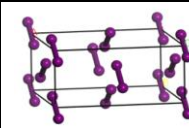
Supplementary Text A4.4 Discussion on the stability test of the perovskite devices

Considering the extrinsic instability (mainly from moisture induced α-to-δ phase transformation, especially for FAMACsPbI$_3$) and the intrinsic instability (mainly from the defects and ion migration, for both compositions), a set of stability test of non-encapsulated and encapsulated devices were carried out (shown in **Figure C4.20**). We found without encapsulation, FAMACsPbI$_3$ went through a rapid decay after the first 24h, and quickly lost all PV performance as the photo-active α-phase easily degraded to δ phase. In comparison, the FAMACsPb(I$_{0.8}$Br$_{0.2}$)$_3$ still retained ~30% of its original PCE after 300h aging even without encapsulation, indicating relatively good phase stability due to the lowered tolerance factor from the excess MAPbBr$_3$ incorporated.

Encapsulating the device prevent the penetration of oxygen and moisture that induces the degradation of perovskite devices via many pathways. In contrasting with the devices without encapsulation, FAMACsPbI$_3$ devices showed a much better stability improvement. After ~300h, it retained approximately 77% of their original performance, while encapsulated FAMACsPb(I$_{0.8}$Br$_{0.2}$)$_3$ devices went through a much faster decay rate where ~50% of their initial performance were lost at the end of the stability test. These results again indicated the better intrinsic stability of tri-iodide perovskite than the mixed-halide WBG perovskite potentially due to their distinct formation dynamics and defect physics.

Appendix B. Supplementary Tables

Supplementary Table B2.1 The DFT relaxed crystal structures of the solid-state phases considered in chemical potential calculations

PEA	KF cubic	F_2 orthorombic	K cubic	PEAI	I_2 orthorombic

Supplementary Table B2.2 PV performance of semitransparent perovskite solar cells

	V_{OC} (V)	J_{SC} (mA/cm^2)	FF (%)	Eff. (%)
Control	1.13	18.2	75.0	15.4
w/ PEAI	1.16	18.3	76.1	16.2
w/ F-PEAI	1.13	18.2	79.6	16.4
Target	1.17	18.6	81.1	17.7
Target (Opaque, Ag electrode)	1.20	22.1	77.3	20.4

Supplementary Table B2.3 PV performance of record efficiency silicon and CIGS solar cells used for numerical efficiency estimation

	V_{OC} (V)	J_{SC} (mA/cm^2)	FF (%)	Eff. (%)
Silicon[9]	0.74	42.3	83.8	26.3
Silicon[9] as rear cell (calculated)	0.72	17.3	83.8	10.4
CIGS[10]	0.73	39.6	80.4	23.4
CIGS[10] as rear cell (calculated)	0.71	17.2	80.4	9.9
Perovskite-Silicon	--			**28.1**
Perovskite-CIGS	--			**27.5**

Supplementary Table B6.1 Optical and electrochemical properties of Y1 and Y2

| | Absorption spectra | | | | Cyclic voltammetry | | |
| | Sol[a] | | Film[b] | | p-doping | n-doping | |
	λ_{max} (nm)	λ_{max} (nm)	λ_{onset} (nm)	E_g^{opt} [c] (eV)	E_{on}^{ox} /HOMO[d] (V)/(eV)	E_{on}^{red} /LUMO[d] (V)/(eV)	E_g^{EC} (eV)
Y1	738	802	905	1.37	1.05 /-5.45	-0.45/-3.95	1.50
Y2	758	827	925	1.34	1.03/-5.43	-0.36/-4.04	1.39

a. Measured in chloroform solution.
b. Cast from chloroform solution.
c. Bandgap estimated from the onset wavelength of the optical absorption.
d. d.HOMO= -e (E_{on}^{ox} +4.4) (eV); LUMO= -e (E_{on}^{red} +4.4) (eV) using (eV) using Ag/AgCl as the reference electrode.

Supplementary Table B6.2 PLQY of Y1 or Y2 blend and pure films

PBDB-T:Y1	Polystyrene:Y1	Pure Y1	PBDB-T:Y2	Polystyrene:Y2	Pure Y2
3.6 %	4.1 %	0.3 %	2.4 %	1.7 %	0.5 %

Supplementary Table B6.3 Photovoltaic performances of different donor/acceptor ratio of PBDB-T:Y1 and PBDB-T:Y2 based PSCs devices with 18 mg mL-1 under 0.8% CN.

Devices	D/A ratio (*w/w*)	V_{oc} (V)	J_{sc} (mA cm^{-2})	FF (%)	PCE (%)
PBDB-T:Y1	1.2:1	0.90	19.62	67.6	12.1
	1:1	0.87	21.69	70.5	13.3
	1:1.2	0.86	19.38	68.6	11.5
	1:1.5	0.81	19.97	64.4	10.1
PBDB-T:Y2	1.2:1	0.85	18.92	66.5	10.7
	1:1	0.81	22.89	71.1	13.2
	1:1.2	0.79	21.78	69.7	12.0
	1:1.5	0.76	20.46	65.5	10.2

Supplementary Table B6.4 The mobilities data and EQE$_{max}$ of PSCs based on Y1 and Y2 blended with PBDB-T.

Active layer [a]	μ_h 10^{-3} cm$^2 \cdot$v$^{-1} \cdot$s^{-1}	μ_e 10^{-4} cm$^2 \cdot$v$^{-1} \cdot$s^{-1}	EQE$_{max}$ (%)
PBDB-T:Y1	1.56	3.04	72
PBDB-T:Y2	2.59	2.08	73

Appendix C. Supplementary Figures

Supplementary Figure C2.1 Fermi level dependence of interaction energies. Neutral and charge defect cases are both considered.
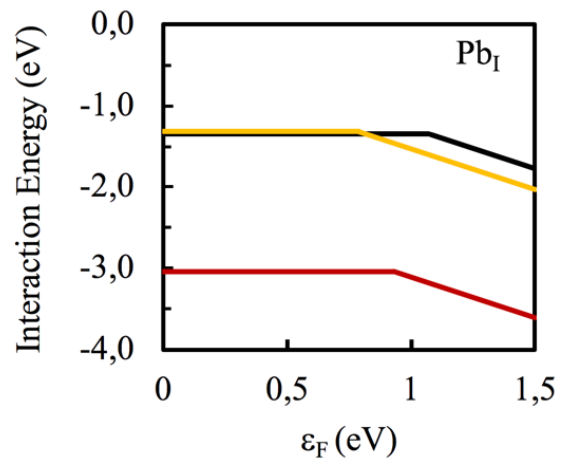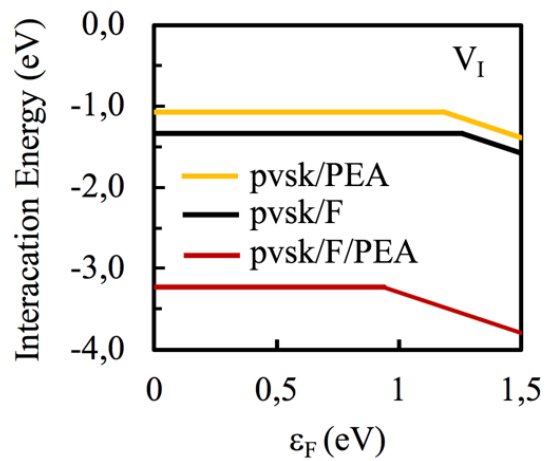
Supplementary Figure C2.2 Energy levels of the WBG perovskite surface with the various treatments. Bandgap of the perovskite was assumed to remain unchanged to obtain the CBM.
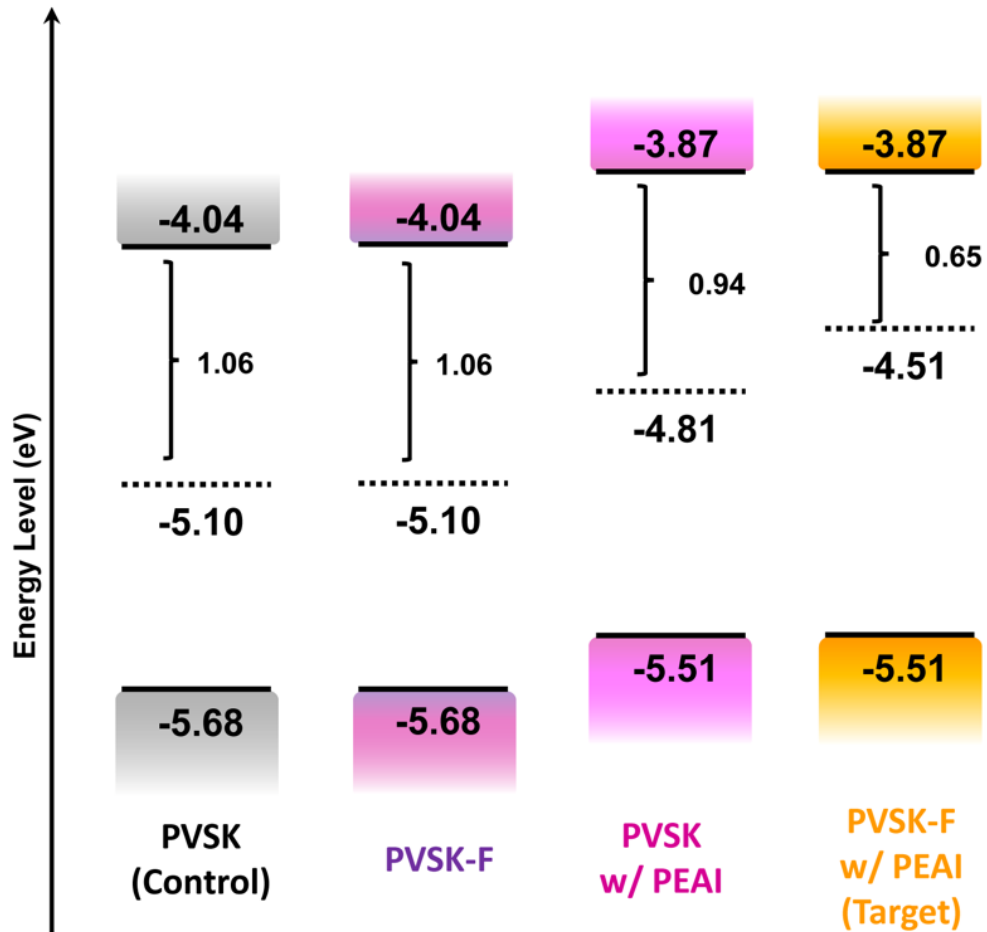
Supplementary Figure C2.3 PL spectrum for the fluoride and OAI treated WBG perovskite films.
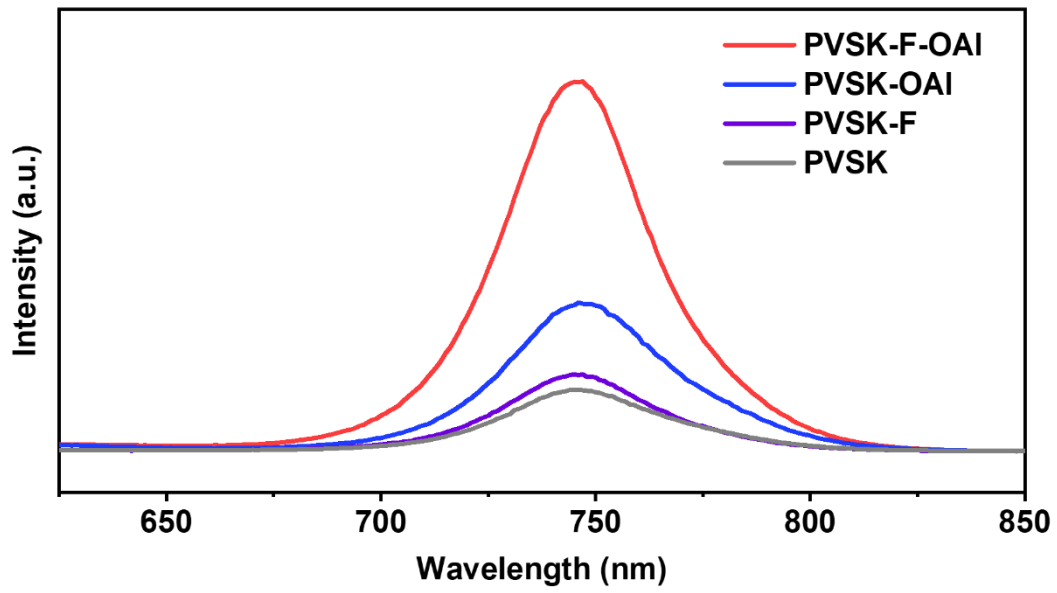
Supplementary Figure C2.4 Side and top views of theoretical models used for V_I (two upper rows) and Pb_I (two lower rows) defects complexation with fluoride present nearby. Refer to Figure C2.1 for their corresponding interaction energies. The Pb, I, C, N, H and F atoms are depicted as dark gray, purple, light gray, blue, white and cyan spheres, respectively.

A — Fluoride present near V_I
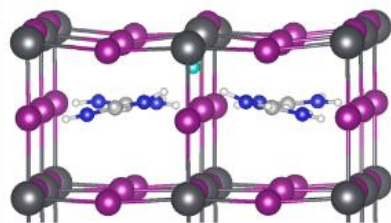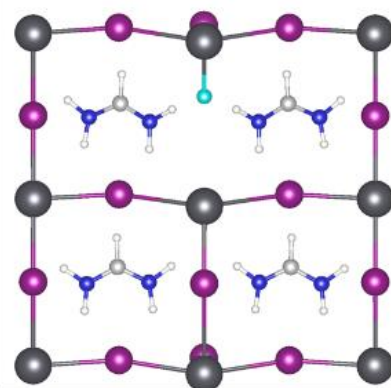
Side view

Top view

B — Fluoride present near Pb_I
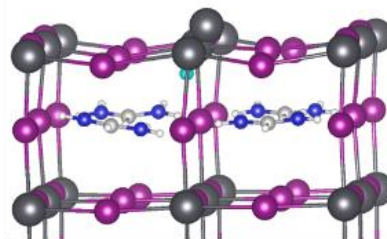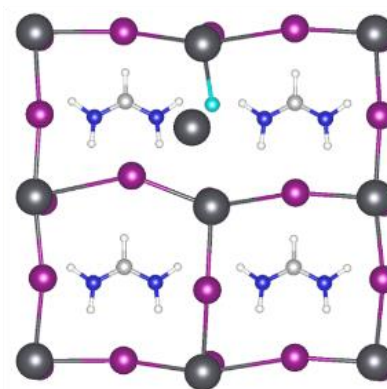
Side view

Top view

Supplementary Figure C2.5 Top and side views of theoretical models used for V_I and Pb_I charged defects interacting with bare PEA (a and b), PEA with fluoride presents nearby (c and d), and their corresponding interaction energies at the CBM. The Pb, I, C, N, H and F atoms are depicted as dark gray, purple, light gray, blue, white and cyan spheres, respectively.

A   Fluoride present near V_I
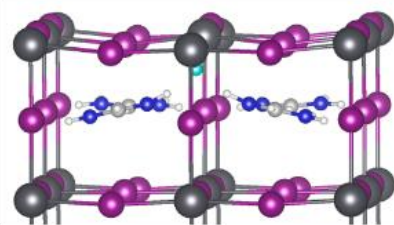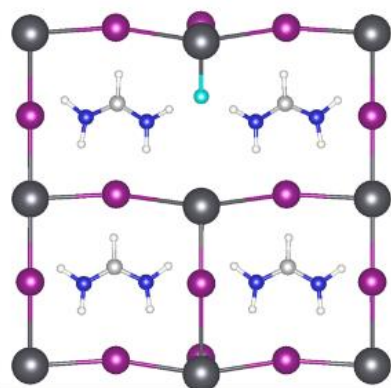
Side view

Top view

B   Fluoride present near Pb_I
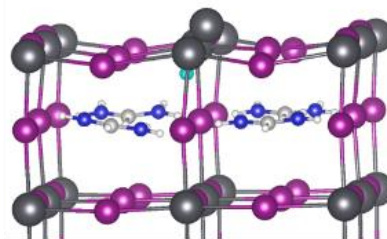
Side view
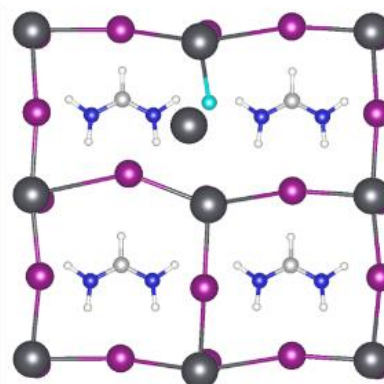
Top view

Supplementary Figure C2.6 The device geometry of the semitransparent perovskite cells.
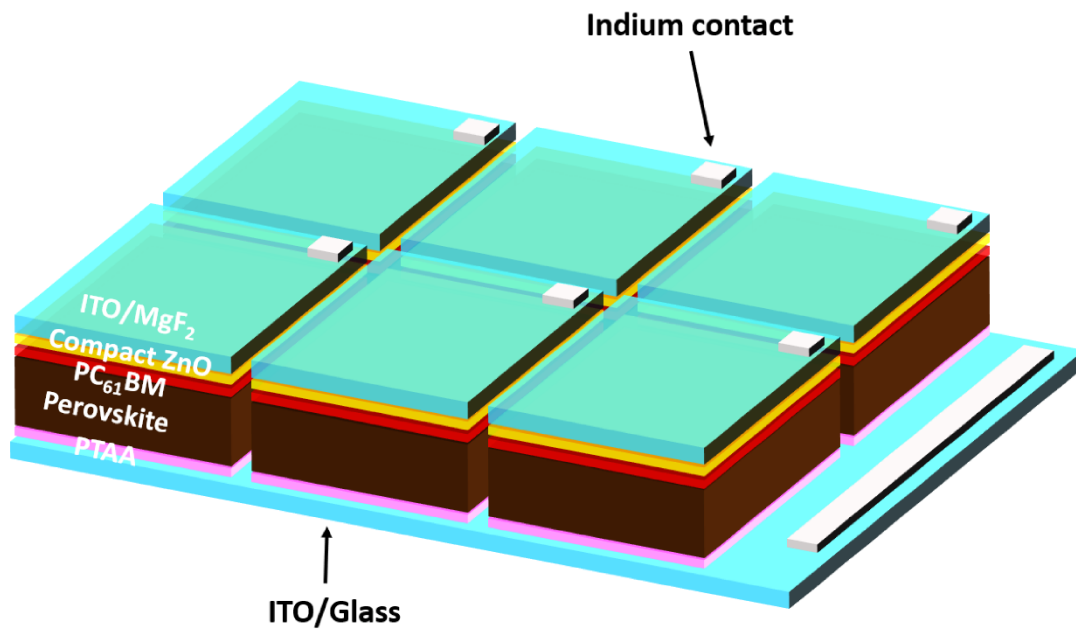
Supplementary Figure C2.7 PCE distribution of the semitransparent perovskite cells with the targeted synergistic passivation treatment (target) and without any treatment (control).
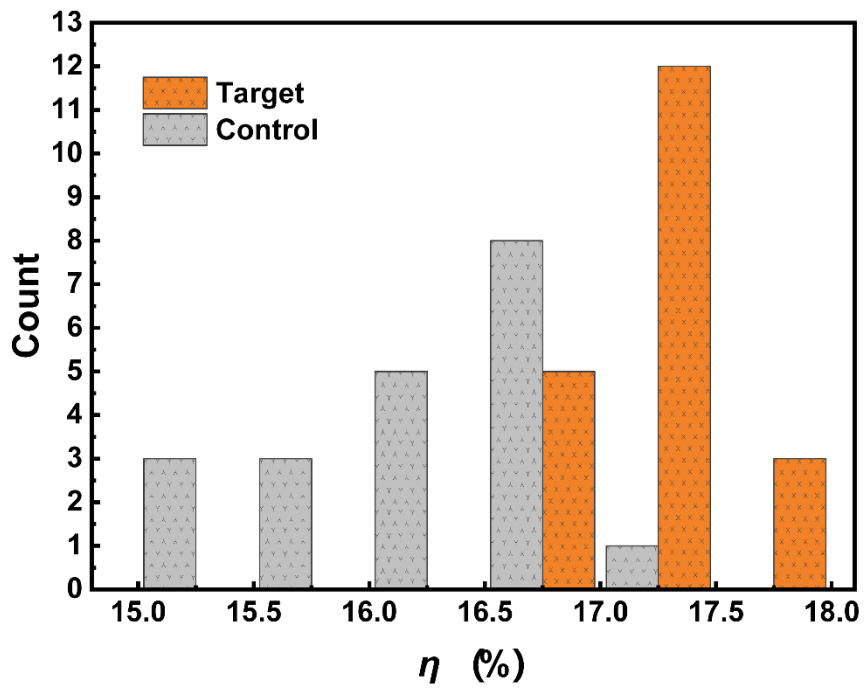
Supplementary Figure C2.8 EQE and the integrated JSC of the opaque perovskite cells with target treatment.
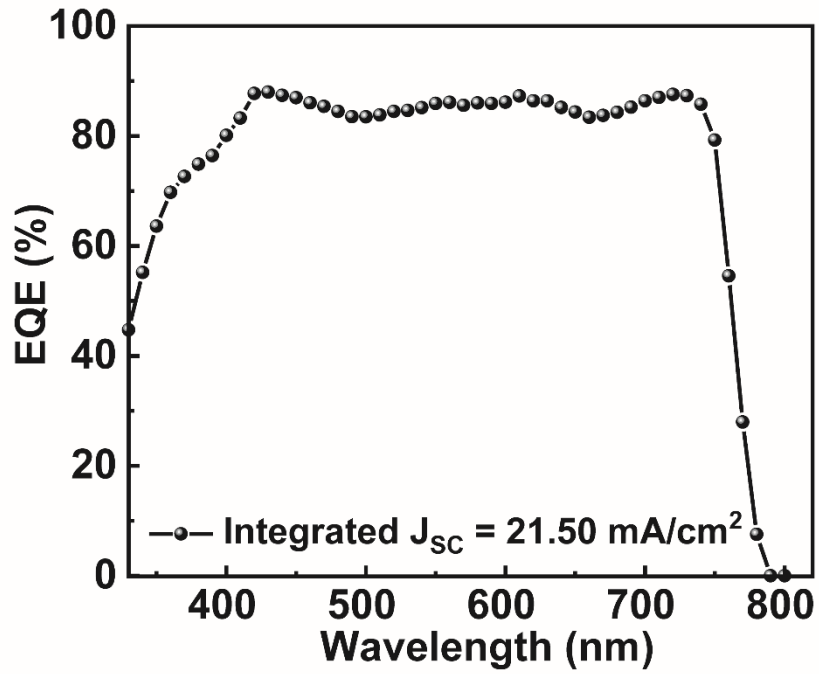
Supplementary Figure C2.9 tDOS extracted from the admitance spectroscopy measurement for perovskite cells with or without treatment.
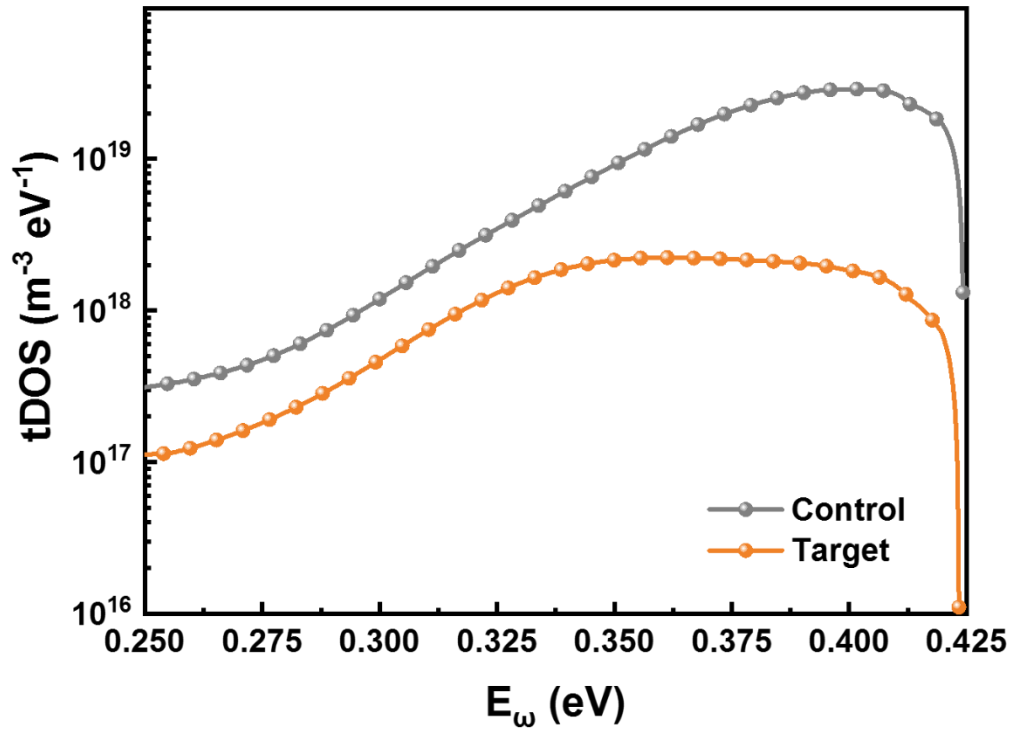
Supplementary Figure C2.10 Transient photocurent current (A) and transient photovoltage (B) measured for perovskite cells with or without treatment.
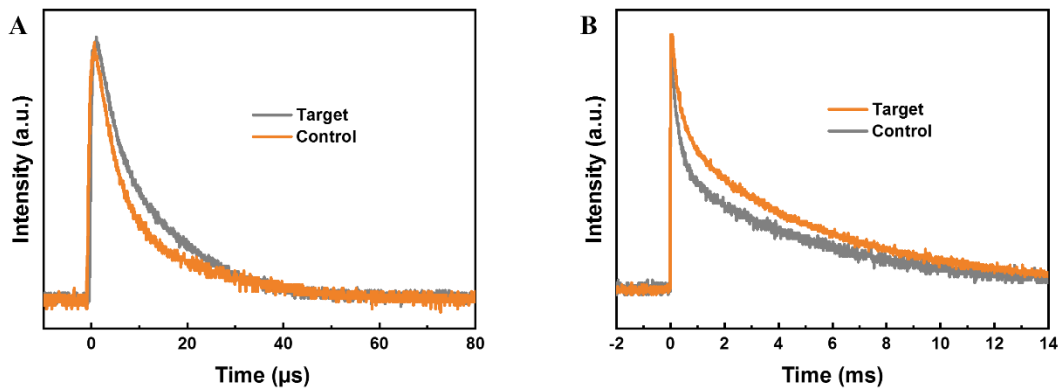
Supplementary Figure C3.1 Photographs of ammonium salts in CF. Photographs of (a) 30 mmol OAI in CF, (b) pure CF, and (c) 30 mmol PEAI in CF. OAI formed a suspension in CF while PEAI remained undissolved at the bottom of the vial in (c).
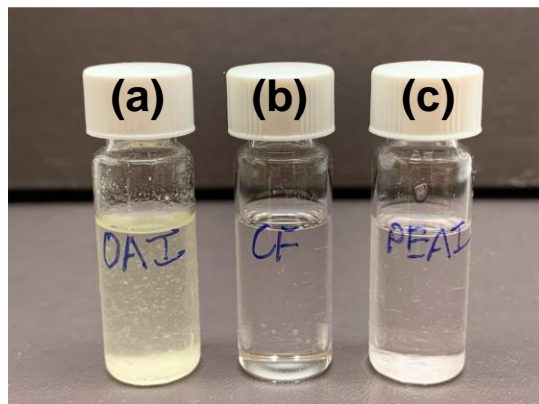
Supplementary Figure C3.2 PL penetration depth estimation. Intensity decay calculated using the Beer-Lambert law. The absorption coefficient is assumed to be 2 x 10^5 cm^{-1} as was reported for α-FAPbI$_3$ thin films.[2] The penetration depth is defined as the depth by which the intensity decays to $\frac{1}{e}$ of its initial value.
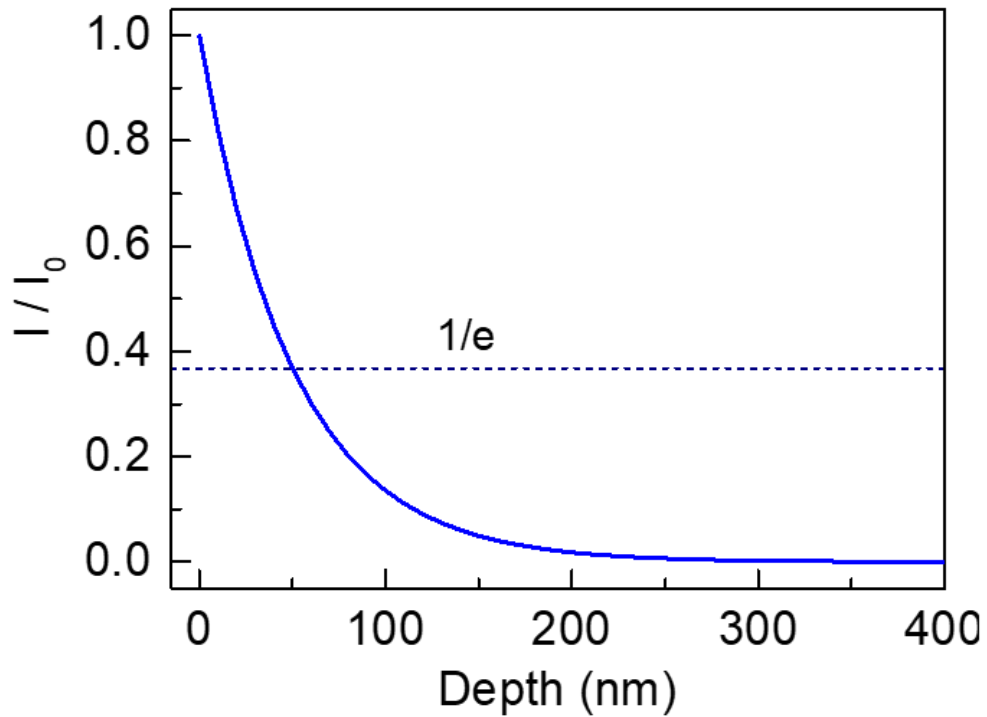
Supplementary Figure C3.3 In situ and time-resolved PL spectra of the perovskite films. (a) Evolution of the raw PL spectra of the perovskite film undergoing treatment with IPA. (b) Normalized time-resolved PL spectra of the perovskite films on glass. Solid white lines are the fitted profiles using a mono-exponential decay function. (c) Contour plot and (d) evolution of the PL intensity of a perovskite film with time.
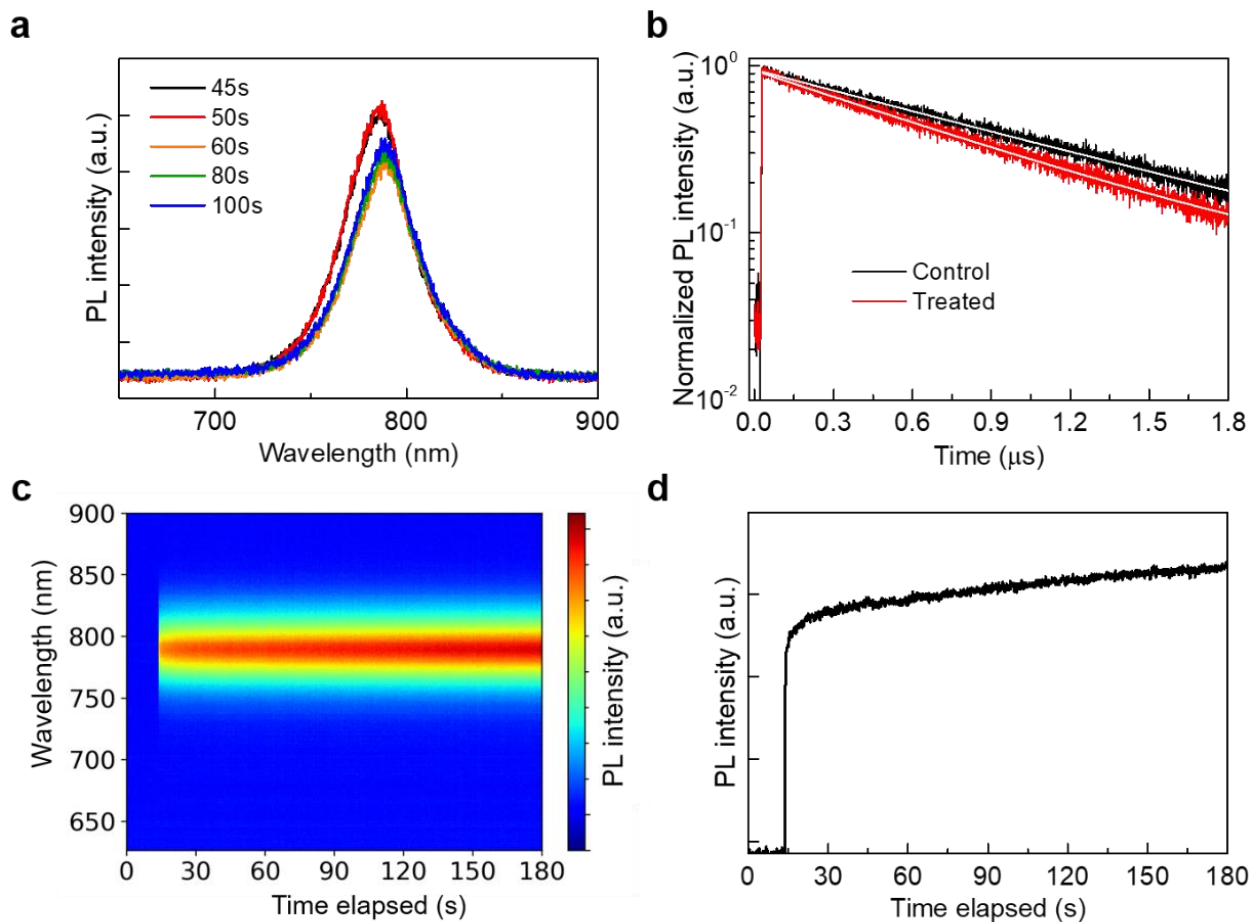
Supplementary Figure C3.4 PAS profile of the perovskite films. PAS depth-profiling of the (a) control and (b) treated perovskite films.
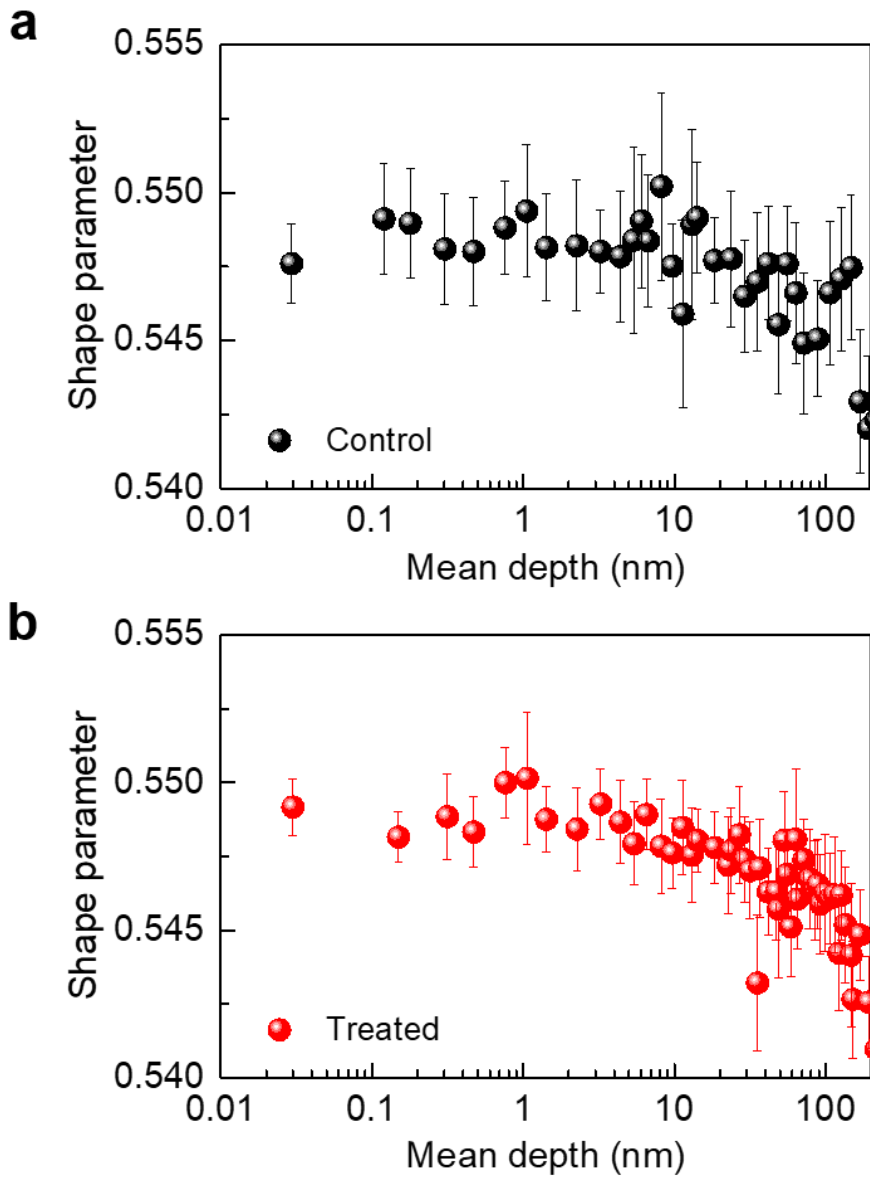
Supplementary Figure C3.5 Device energy alignment and performance. (a) Schematic band diagram of the energy levels of the IPA treated perovskite film relative to the fermi level. Current density-voltage curves of the (b) control and (c) treated devices in reverse (in black) and forward (in blue) scans.
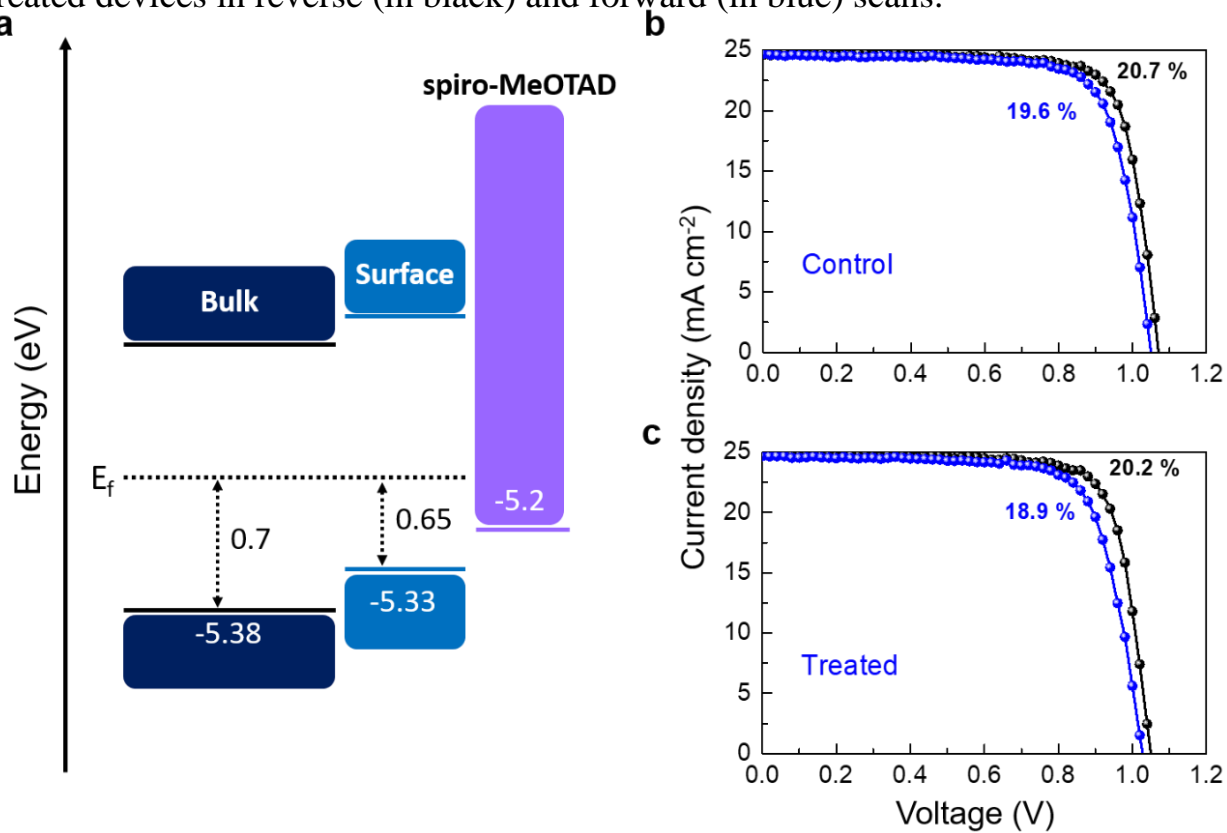
Supplementary Figure C3.6 Humidity stability testing on the perovskite films.
Absorbance at 600 nm of the perovskite films exposed to RH 75 ± 10% with time.
Inset shows photographs of the films.
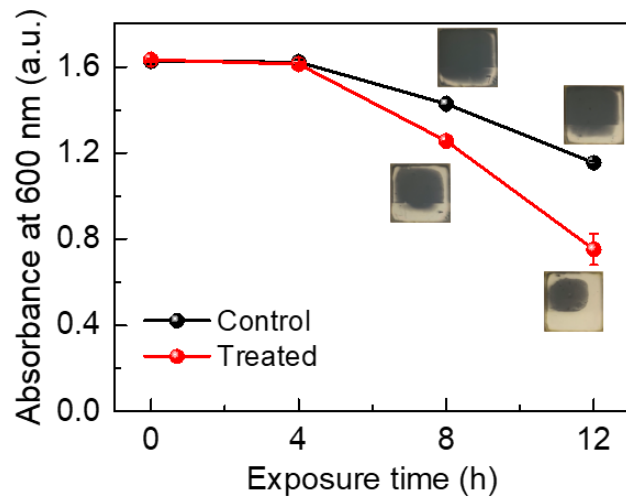
Supplementary Figure C3.7 Modified surface treatment process. Schematic performance for the (a) conventional and (b) modified surface treatments procedures. (c) Enthalpy of adsorption of OABr on the surfaces.
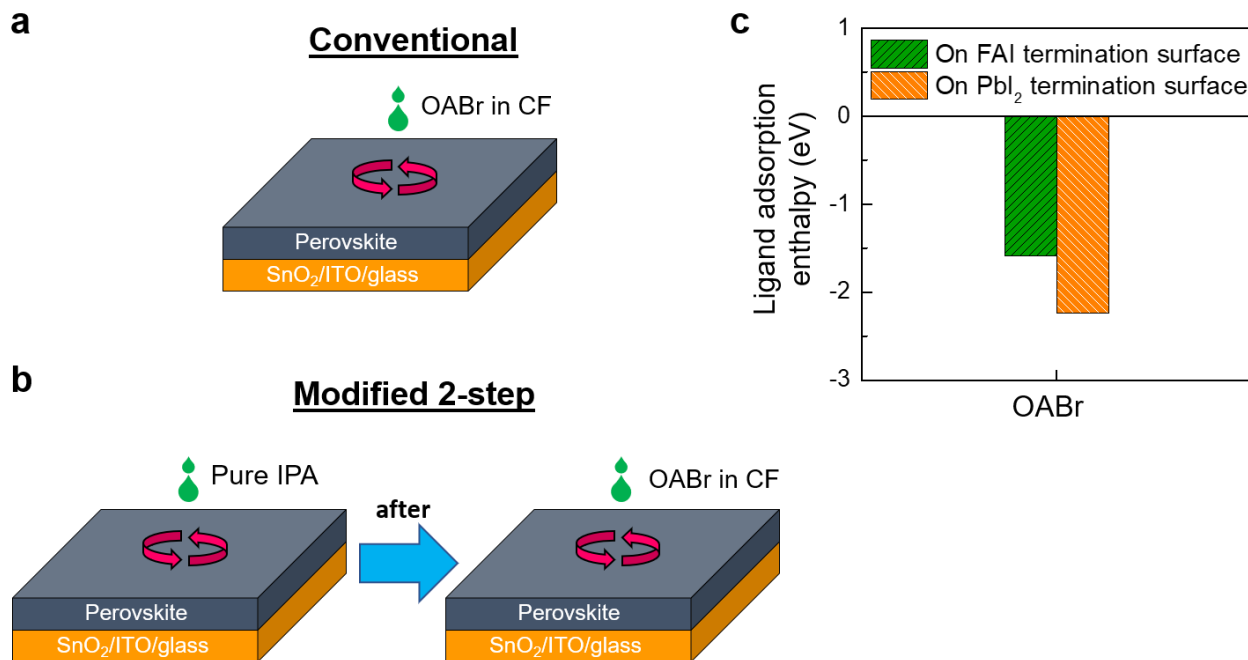
Supplementary Figure C3.8 In situ PL of films undergoing surface treatment. Evolution of the PL intensity of films treated with (a) 10 mM OAI or (b) 10 mM PEAI as a function of time.

138
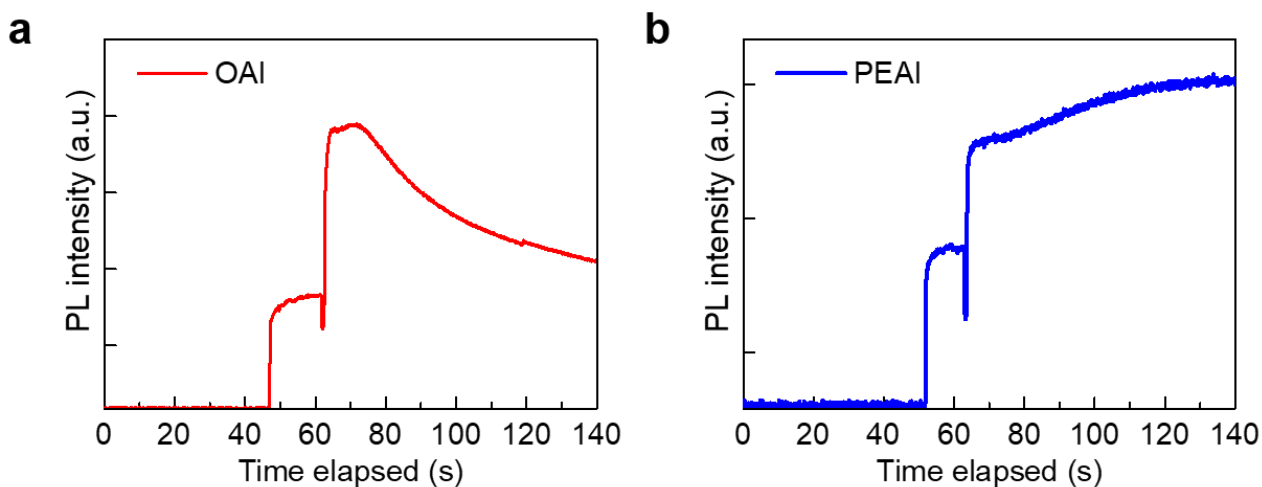
Supplementary Figure C3.9 In situ PL of films undergoing post-annealing.
Contour plots of perovskite films treated with (a) 25 mM OAI or (b) 25 mM PEAI in
IPA undergoing post-annealing. Evolution with time of the raw PL spectra of the
films treated with (c) 25 mM OAI or (d) 25 mM PEAI during post-annealing. (E)
Deconvoluted peaks of the PL spectra at 300s for the OAI treated film.
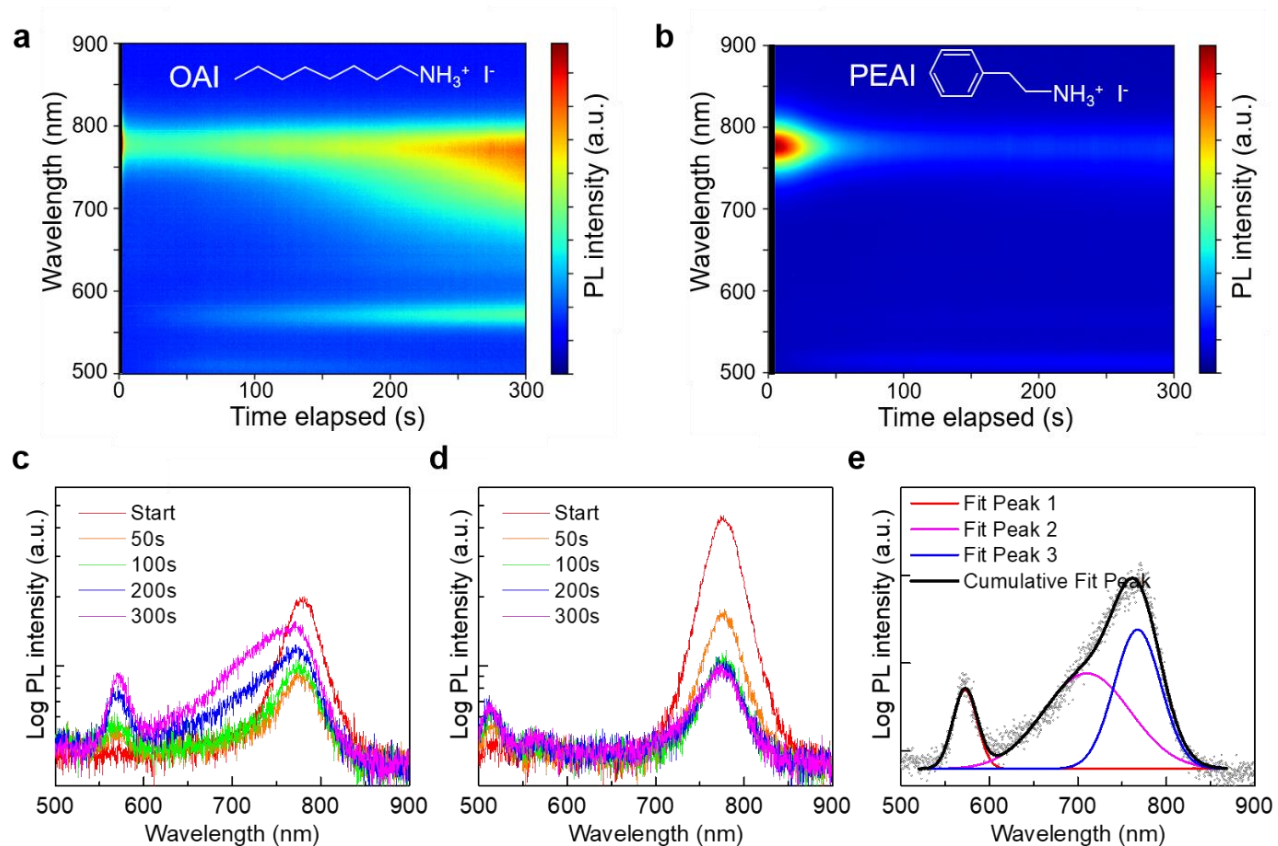
Supplementary Figure C4.1 XRD results of the as-cast and fully annealed perovskite films of FAMACsPbX$_3$. (A) The XRD patterns of the as-cast and fully annealed perovskite films of FAMACsPbX3. (B) The extracted peak intensities of the (001) peak of perovskite and the PbI2 peak.
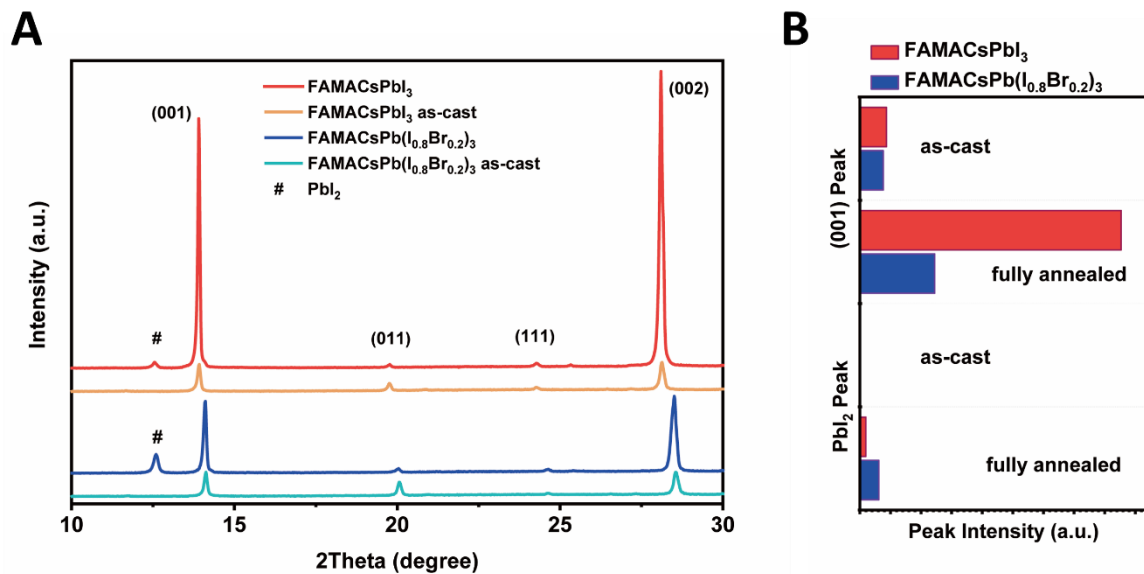
Supplementary Figure C4.2 XRD results of the as-cast and fully annealed perovskite films of FACsPbX$_3$. (A) The XRD patterns of the as-cast and fully annealed perovskite films of FACsPbX$_3$. (B) The extracted peak intensities of the (001) peak of perovskite and the PbI$_2$ peak.
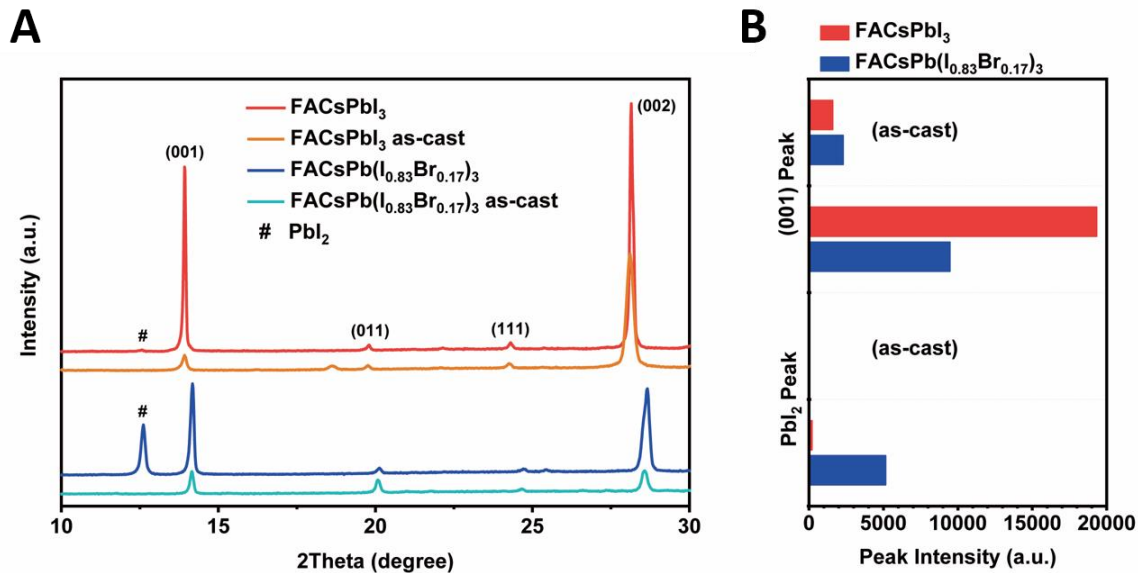
Supplementary Figure C4.3 XRD spectra of (001) peak of FACsPbX$_3$ films.
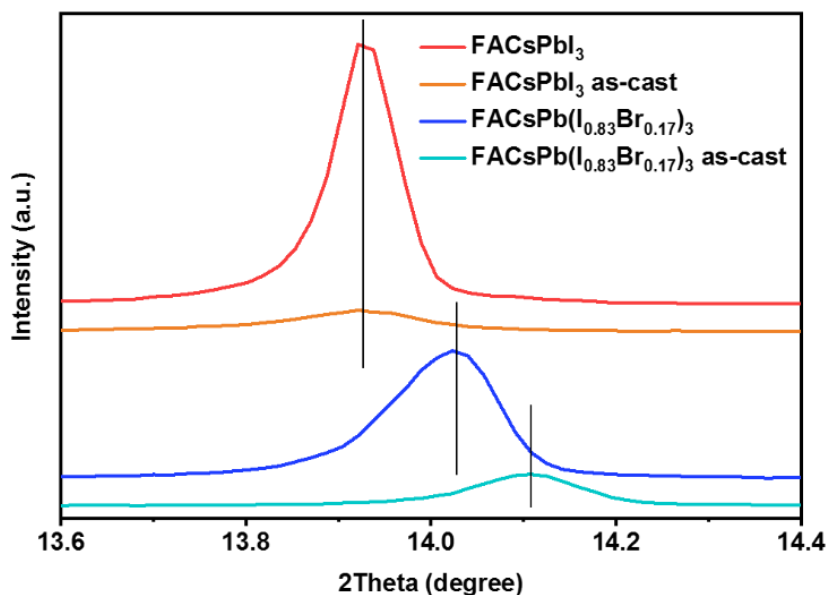
Supplementary Figure C4.4 SEM image of CsFAMAPb(I$_{0.8}$Br$_{0.2}$)$_3$ and CsFAMAPbI$_3$. Flakes-shape PbI$_2$ can be observed on the CsFAMAPb(I$_{0.8}$Br$_{0.2}$)$_3$ surface. For CsFAMAPbI$_3$ prepared as exact same annealing condition, surface PbI$_2$ can be hardly observed.
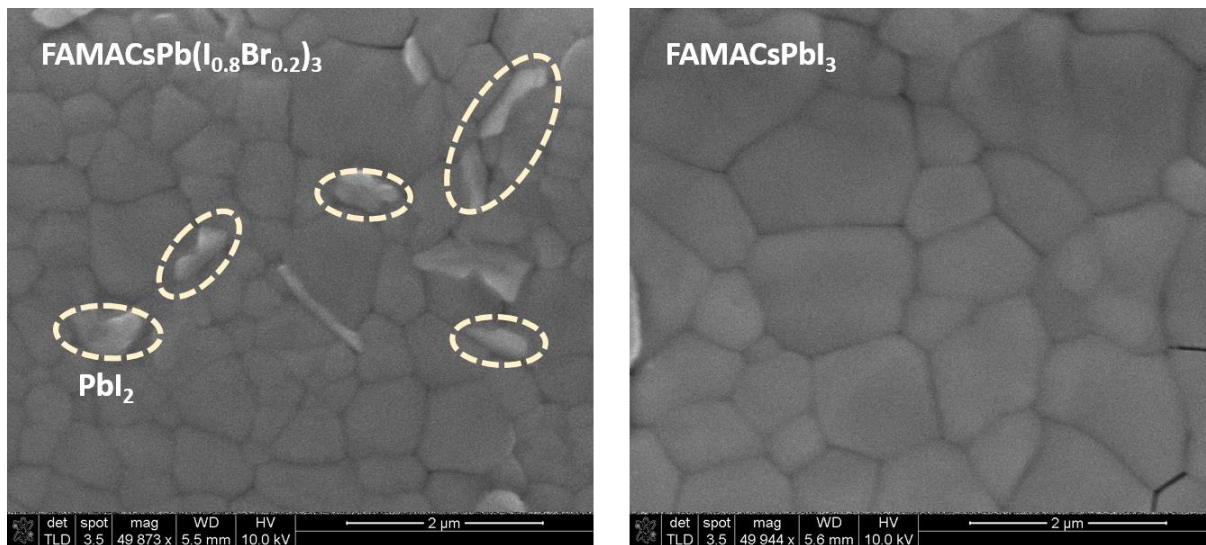
Supplementary Figure C4.5 XRD results of MAPb(I$_X$Br$_{1-X}$)$_3$ films. High resolution diffraction patters at the 2θ range of 13.5◦ to 15.5◦ of the as-cast, pre-annealed (65°C for 1 min), and fully annealed (100◦C for 10 min) MAPb(I$_X$Br$_{1-X}$)$_3$ films (without MACl additive). From A-E are X=1, 0, 0.9, 0.8 and 0.5, respectively.
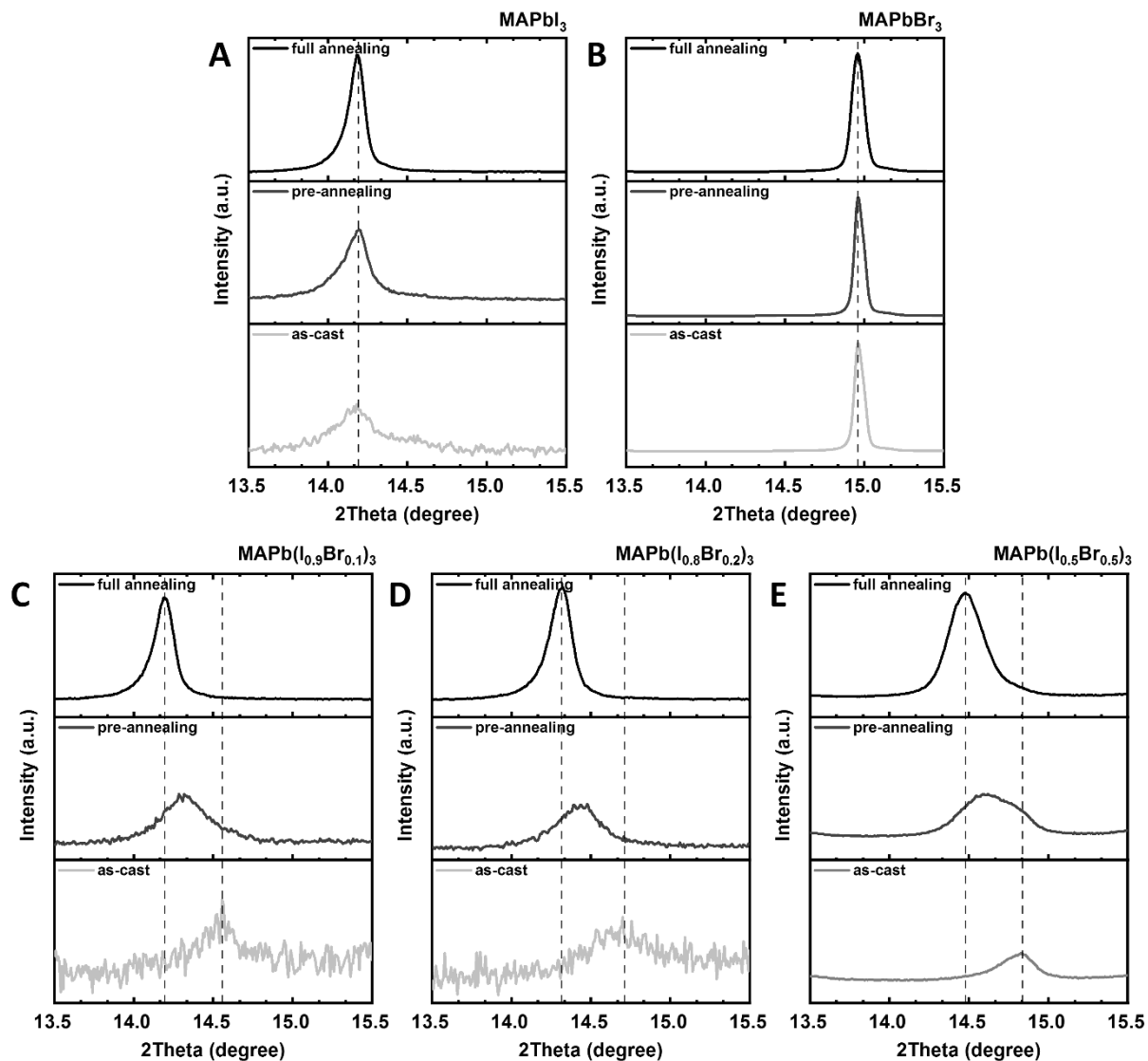
Supplementary Figure C4.6 XRD results of FAPb(I$_X$Br$_{1-X}$)$_3$ films. High resolution diffraction patters at the 2θ range of 13.5∘ to 15.5∘ of the as-cast, pre-annealed (65°C for 1 min), and fully annealed (100∘C for 10 min) FAPb(I$_X$Br$_{1-X}$)$_3$ films (without MACl additive). From A-E are X=1, 0, 0.9, 0.8 and 0.5, respectively.
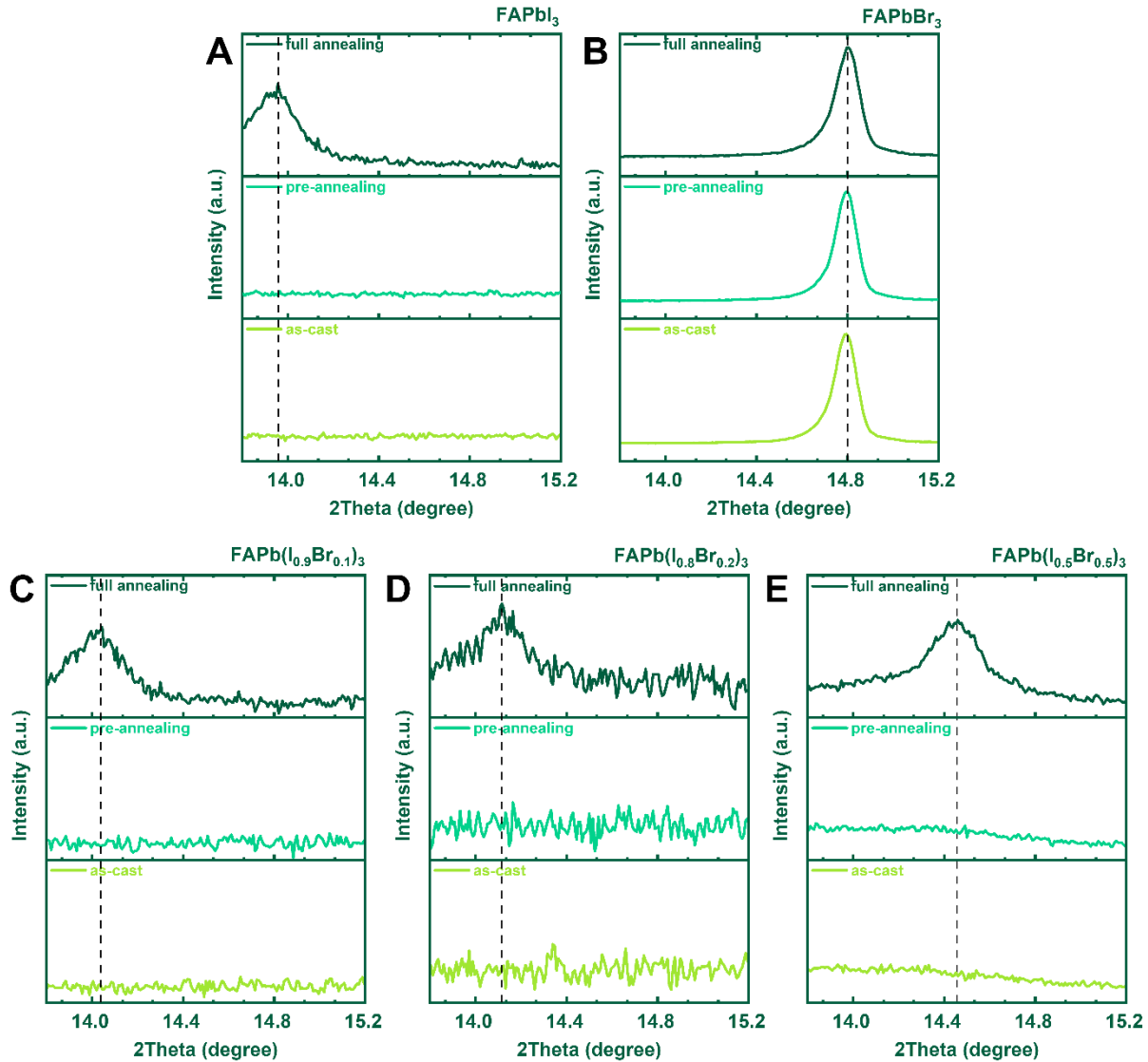
Supplementary Figure C4.7 XRD results of FAPb($I_X Br_{1-X}$)$_3$ films with MACl additive. High resolution diffraction patters at the 2θ range of 13.5◦ to 15.5◦ of the as-cast, pre-annealed (65°C for 1 min), and fully annealed (100◦C for 10 min) FAPb($I_X Br_{1-X}$)$_3$ films (with MACl additive). From A-E are X=1, 0, 0.9, 0.8 and 0.5, respectively.
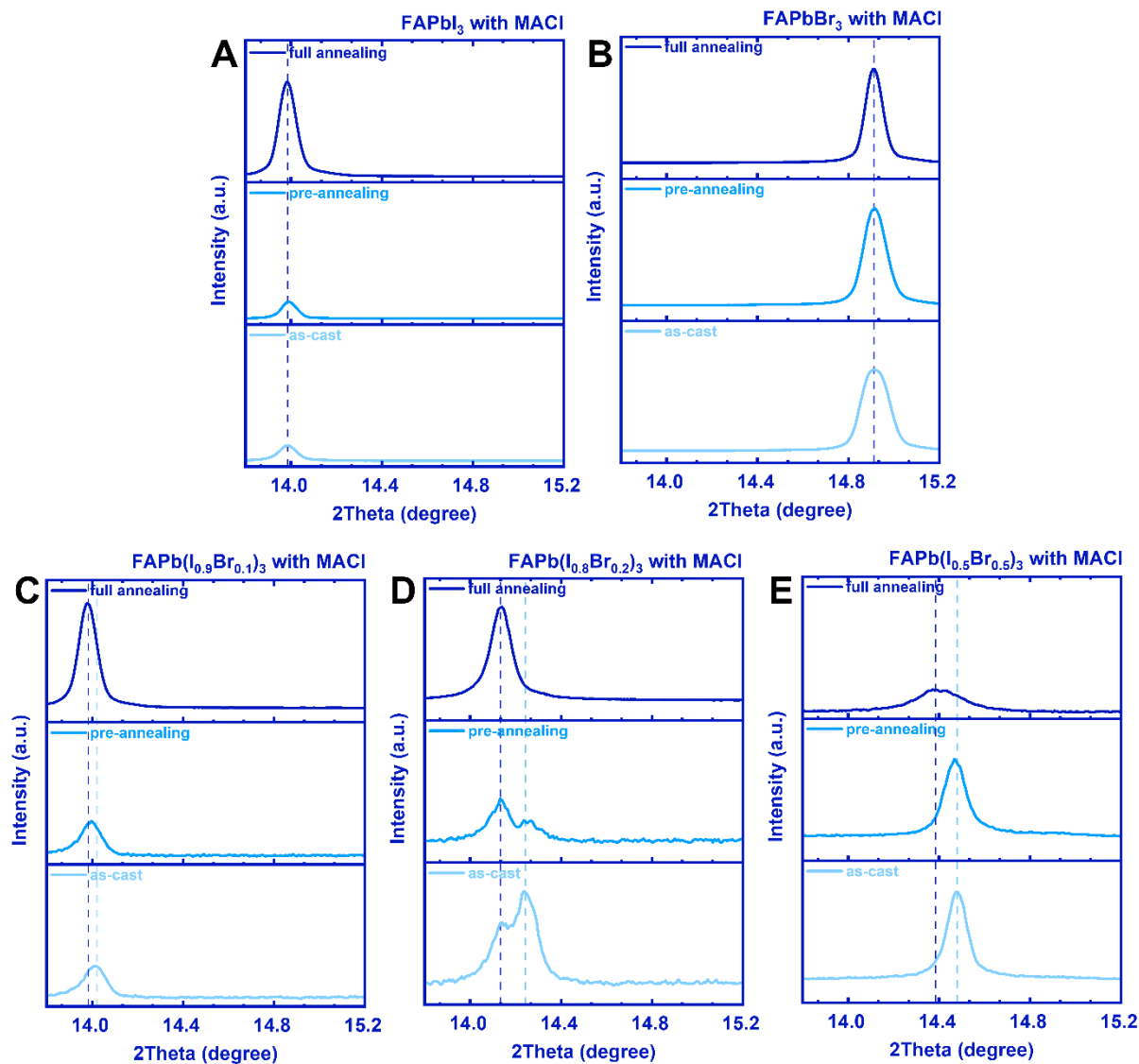
Supplementary Figure C4.8 XRD results of FAMACsPb($I_X Br_{1-X}$)$_3$ films. High resolution diffraction patters at the 2θ range of 13.5◦ to 15.5◦ of the as-cast, pre-annealed (65°C for 1 min), and fully annealed (100◦C for 10 min) FAMACsPb($I_X Br_{1-X}$)$_3$ films (without MACl additive). From A-E are X=1, 0, 0.9, 0.8 and 0.5, respectively.
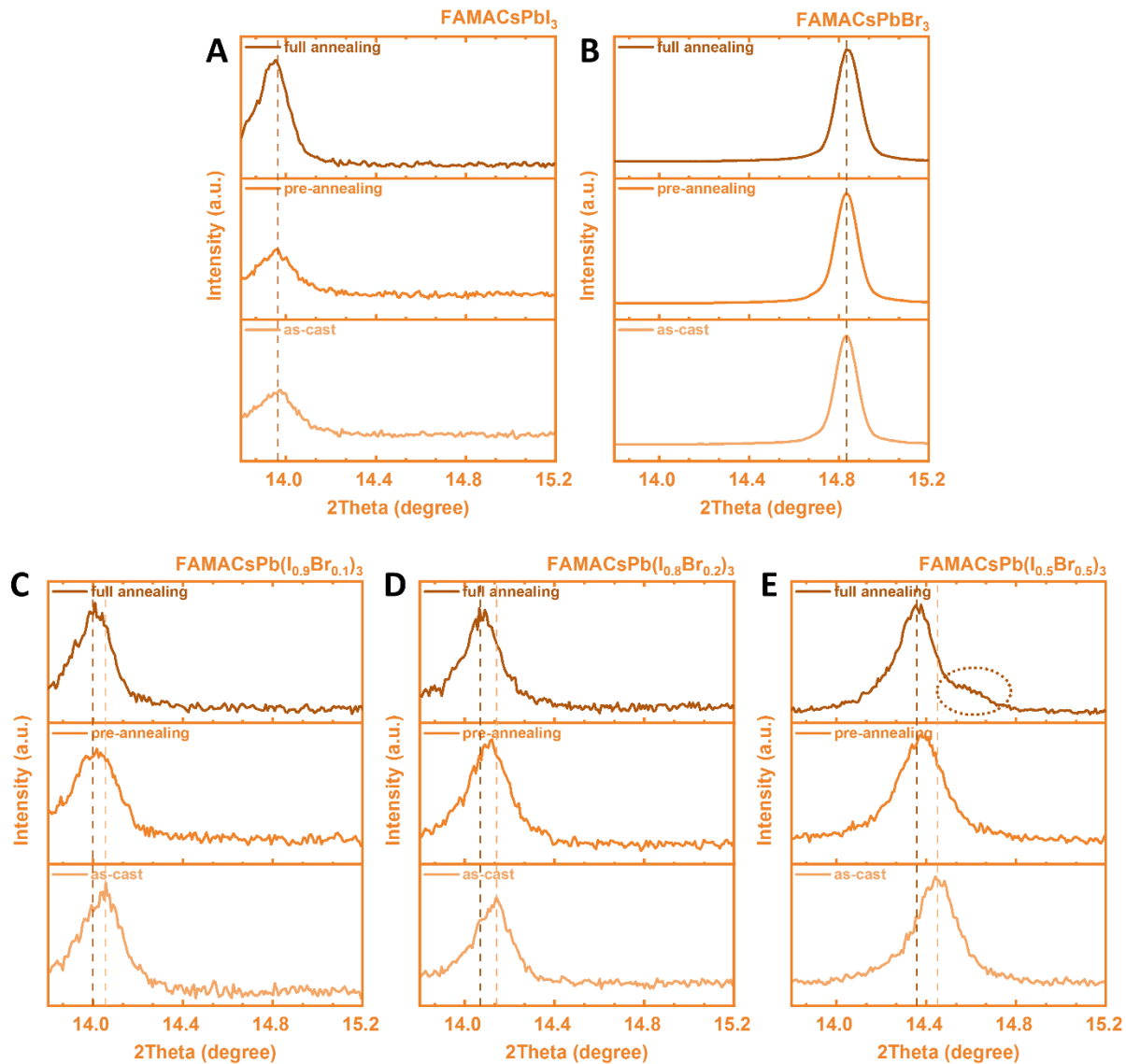
Supplementary Figure C4.9 XRD results of FACsPb(I$_X$Br$_{1-X}$)$_3$ films. High resolution diffraction patters at the 2θ range of 13.5° to 15.5° of the as-cast, pre-annealed (65°C for 1 min), and fully annealed (100°C for 10 min) FACsPb(I$_X$Br$_{1-X}$)$_3$ films (without MACl additive). From A-E are X=1, 0, 0.9, 0.8 and 0.5, respectively.
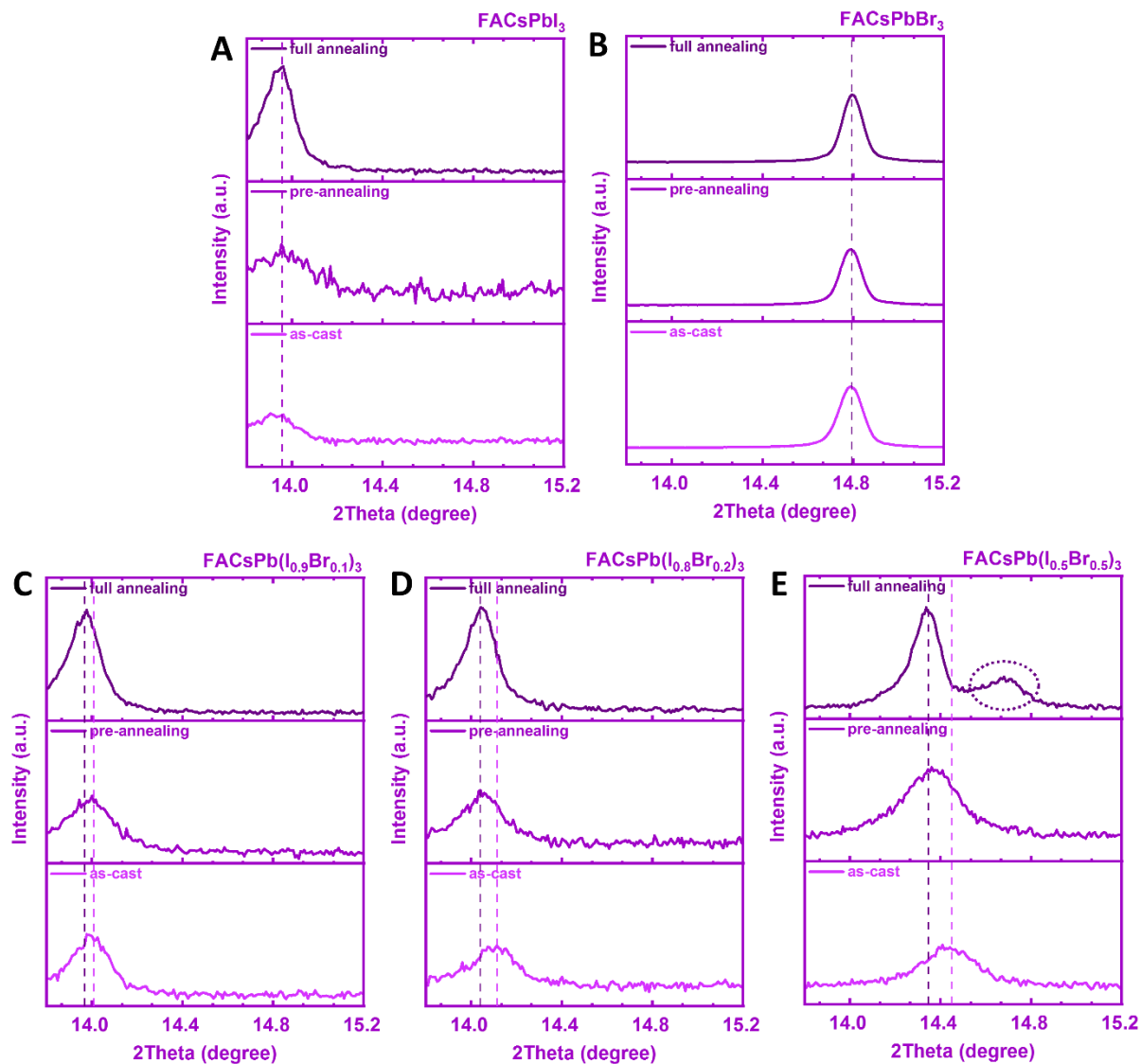
Supplementary Figure C4.10 Selected spectra from in-situ PL measurements.
During spin-coating (A and C) and annealing (B and D) for FAMACsPbI$_3$ and
FAMACsPb(I$_{0.8}$Br$_{0.2}$)$_3$. Gaussian fitting results shown in grey lines.
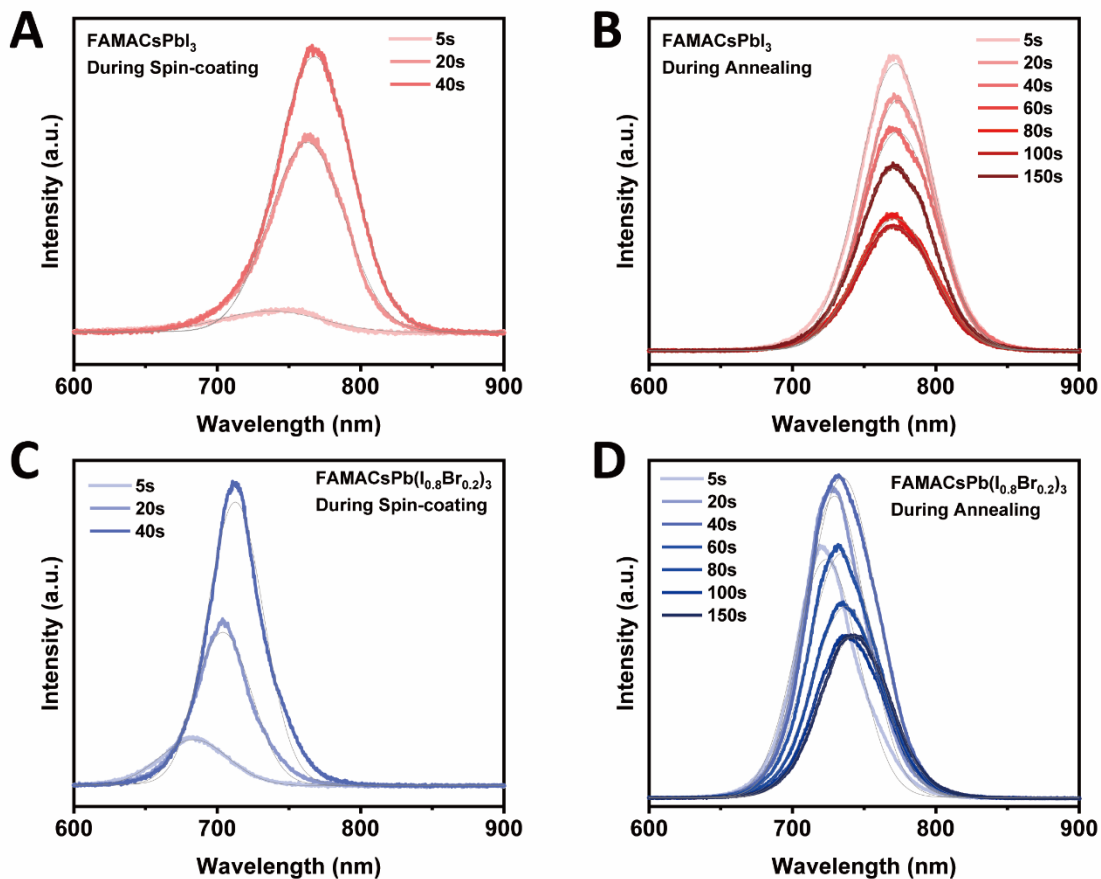
Supplementary Figure C4.11 The extracted values of emission peak position for FAMACsPb(I,Br)₃ perovskite with Br% of 20%, 10%, 5% and 0%. A slight rise in peak position observed before ~50 s is result from the enhance and broadening of the PL signal (details disccued in Figure C4.13).
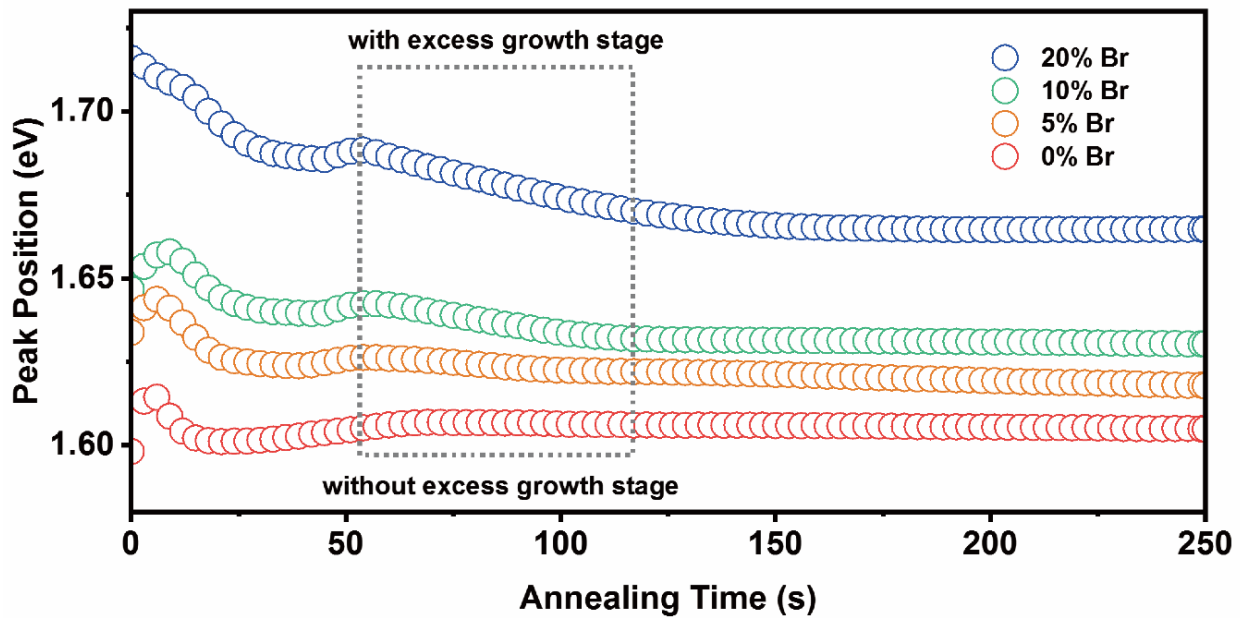
Supplementary Figure C4.12 UV-Absorption curve (in Tauc plot) and static PL spectra of the fully annealed perovskite films.
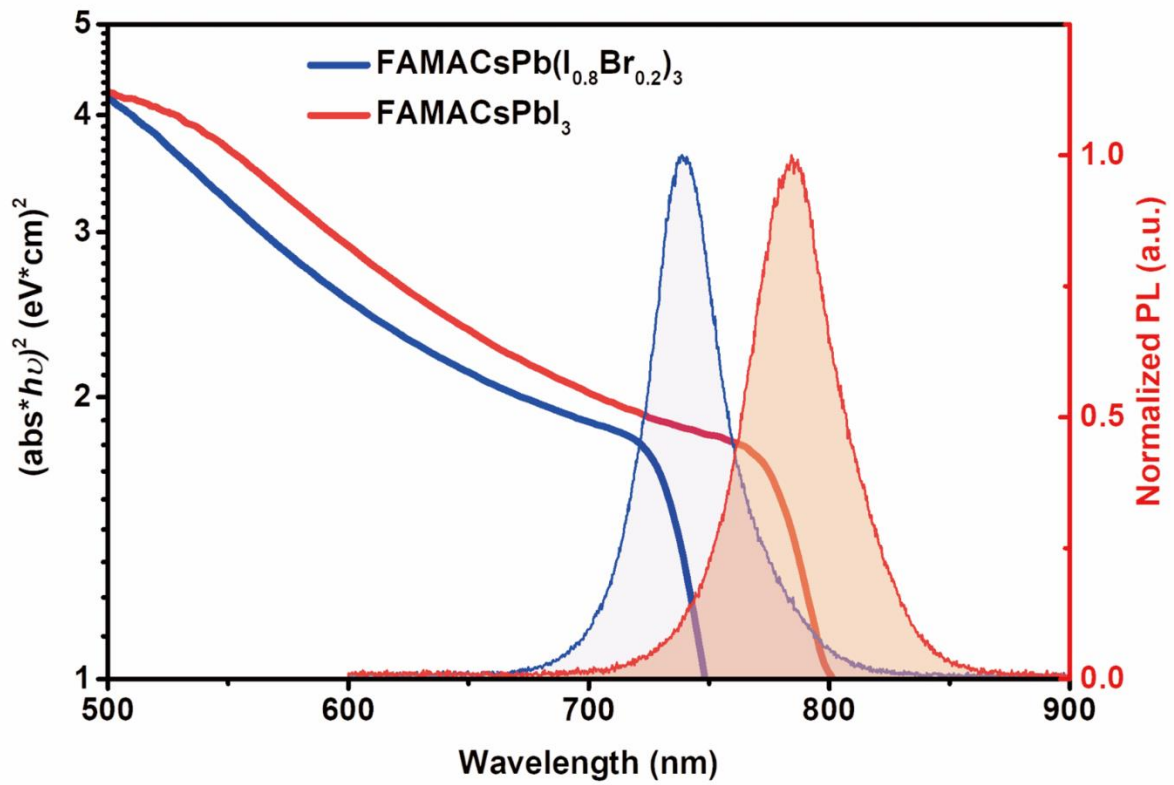
Supplementary Figure C4.13 The contour plot of the captured PL spectra during the growth of FACsPbX₃ perovskites. (A) FACsPb(I$_{0.83}$Br$_{0.17}$)$_3$ and (B) FACsPbI$_3$ films during spin-coating (left) and annealing (right).
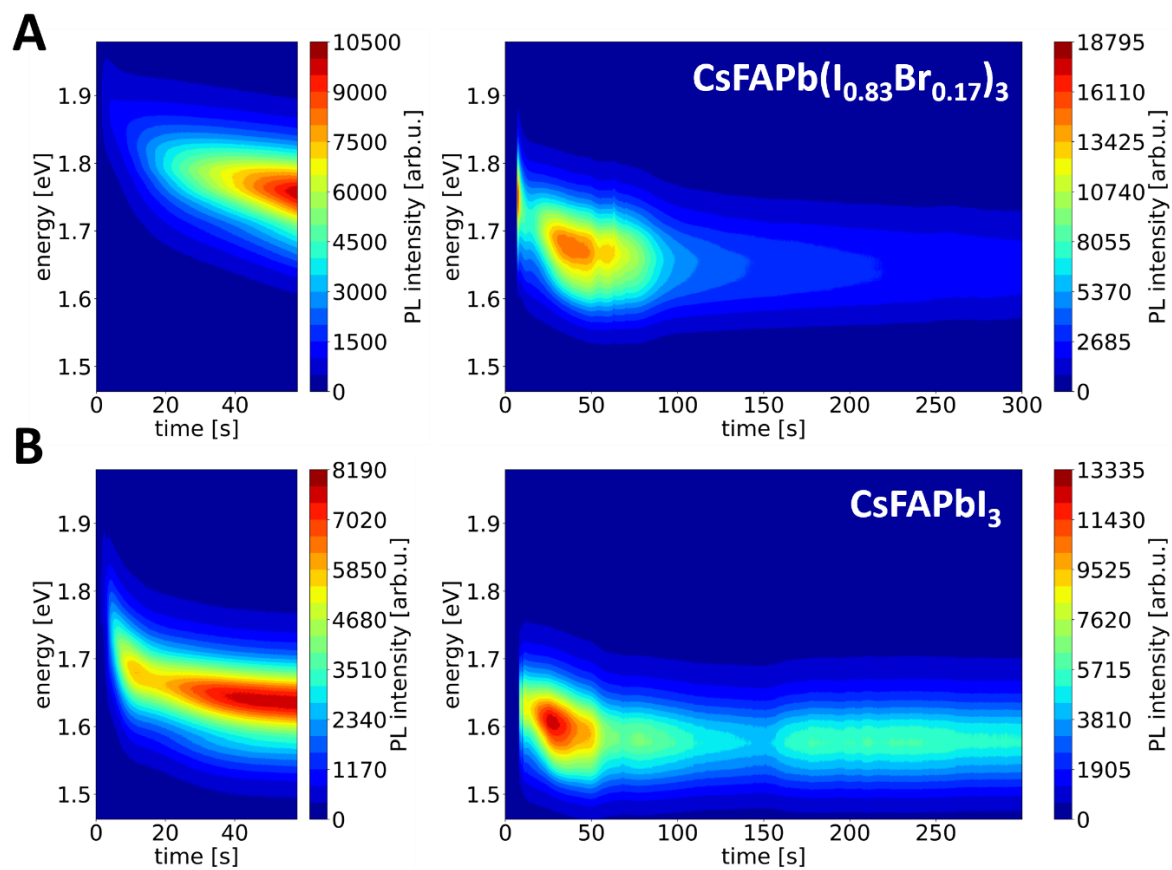
Supplementary Figure C4.14 The extracted values of emission peak position (A), PL intensity (B), and FWHM (C) from the in-situ PL measurements for FACsPbX$_3$ perovskites. By fitting the peak position signals during annealing with a biexponential decay model, it was found that the FACsPb(I$_{0.83}$Br$_{0.17}$)$_3$ film also exhibited an excess growth stage (two-stage transition) while the FACsPbI$_3$ film still had a one-stage transition.
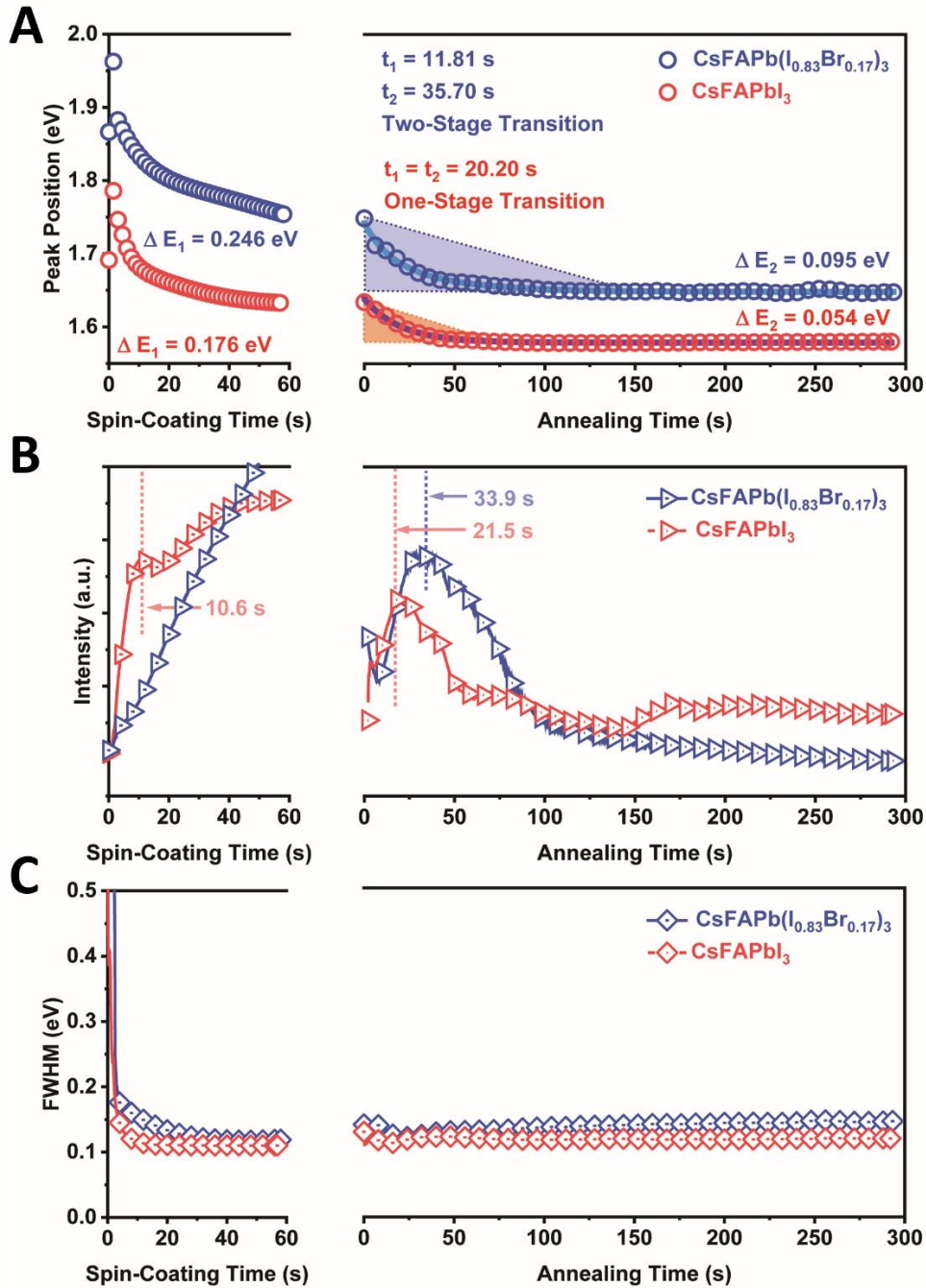
**Supplementary Figure C4.15 PL signals at *absolute* time scale near CB casting.** By fitting the peak position signals during annealing with a biexponential decay model, it was found that the $FACsPb(I_{0.83}Br_{0.17})_3$ film also exhibited an excess growth stage (two-stage transition) while the $FACsPbI_3$ film still had a one-stage transition. The extracted values of emission peak position (A) at the absolute time elapsed and the corresponding raw PL spectra (B) near the moment of CB (anti-solvent) casting replotted from the original dataset of Figure 2D (left slab). The PL transition near CB dripping could be rationally divided into three stages: (I). Before CB dripping that no PL could be observed (refer to the spectrum of 125s). At this stage, the "Peak Position" values were simply extracted from gaussian fitting of the background spectra. (II). CB with boiling point as high as 132°C will take seconds to fully spin-off and evaporate from the film surface after dripping. At this "CB drying" stage, quasi-stable nanoscale surface perovskite nuclei with strong quantum confinement effect could form but could also re-dissolve into the residual solvent in the wet precursor film bulk (even though the overall thermodynamics would move to the direction of nuclei growth). The composition of these nuclei can far deviate from the precursor and with much higher Br%. As a result, the actual PL signal started to form from extremely lower intensity and at much higher energy level (also refer to Figure 2E), while the fitted PL peak position value also rose from that of the background spectra. (III). After the CB and residual solvent being mostly removed, and PL signal starts to form as perovskite grows initiated from the surface. An obvious rising and broadening of PL was observed at this stage, and with the rapid increase in PL intensity and FWHM, peak position naturally went through slight increased (blue shift) as an increase in charge carrier density populating in the excited states. These electronic dynamics upon nucleation occurs much faster than the bandgap change due to halide migration and homogenization, thus dominated the peak position changes at this stage.
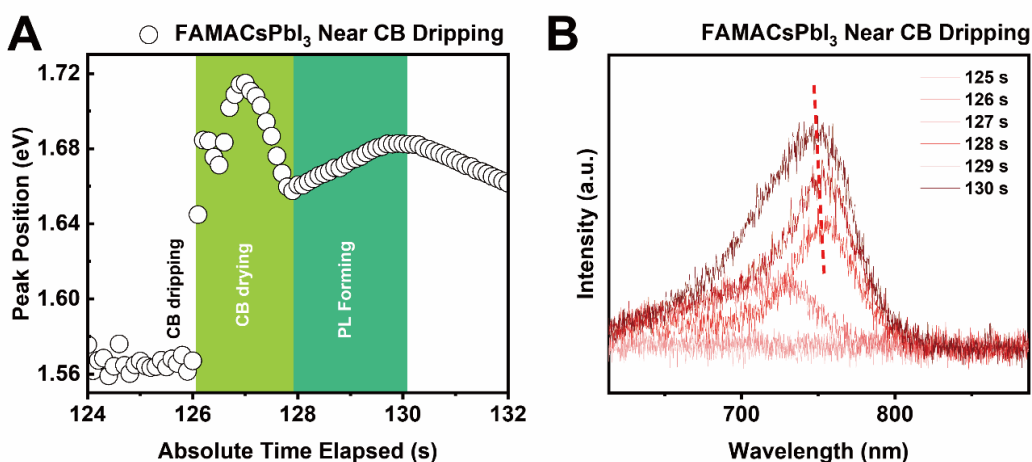
Supplementary Figure C4.16 Side (A) and top (B) view of the optimum crystal structure of DMSO:PbXX' adduct. X sites were assumed to be I in the structure.
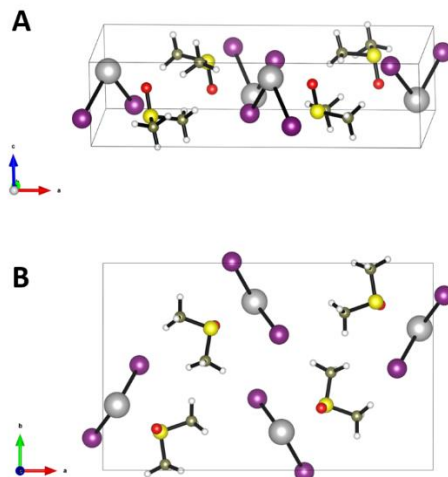
Supplementary Figure C4.17 The calculated results of surface energy difference in tri-iodide perovskites and tri-bromide perovskites with cations to be Cs, MA, or FA.
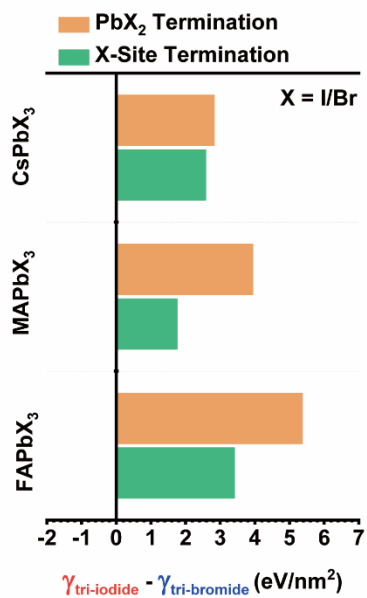
Supplementary Figure C4.18 Fermi energy (E_F) dependence of the defect formation energy of FA vacancy and FA interstitial point defects. FAPbI$_3$ (orange line), FAPb(I$_{0.8}$Br$_{0.2}$)$_3$ (black line) and FAPbBr$_3$ (green line). $E_F = 0$ was set at VBM.
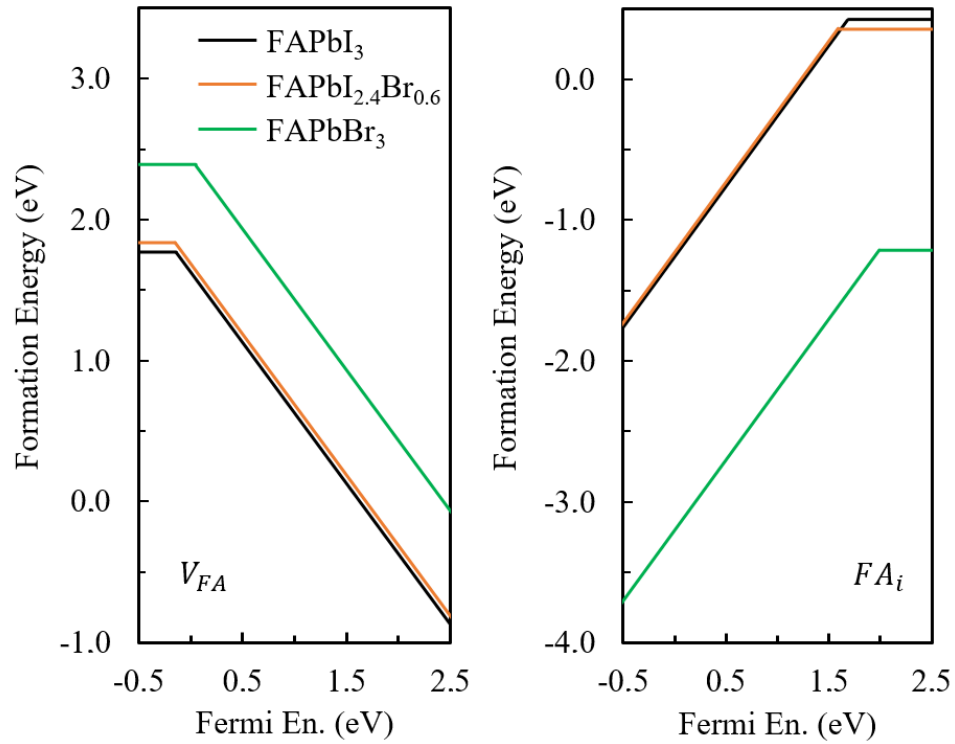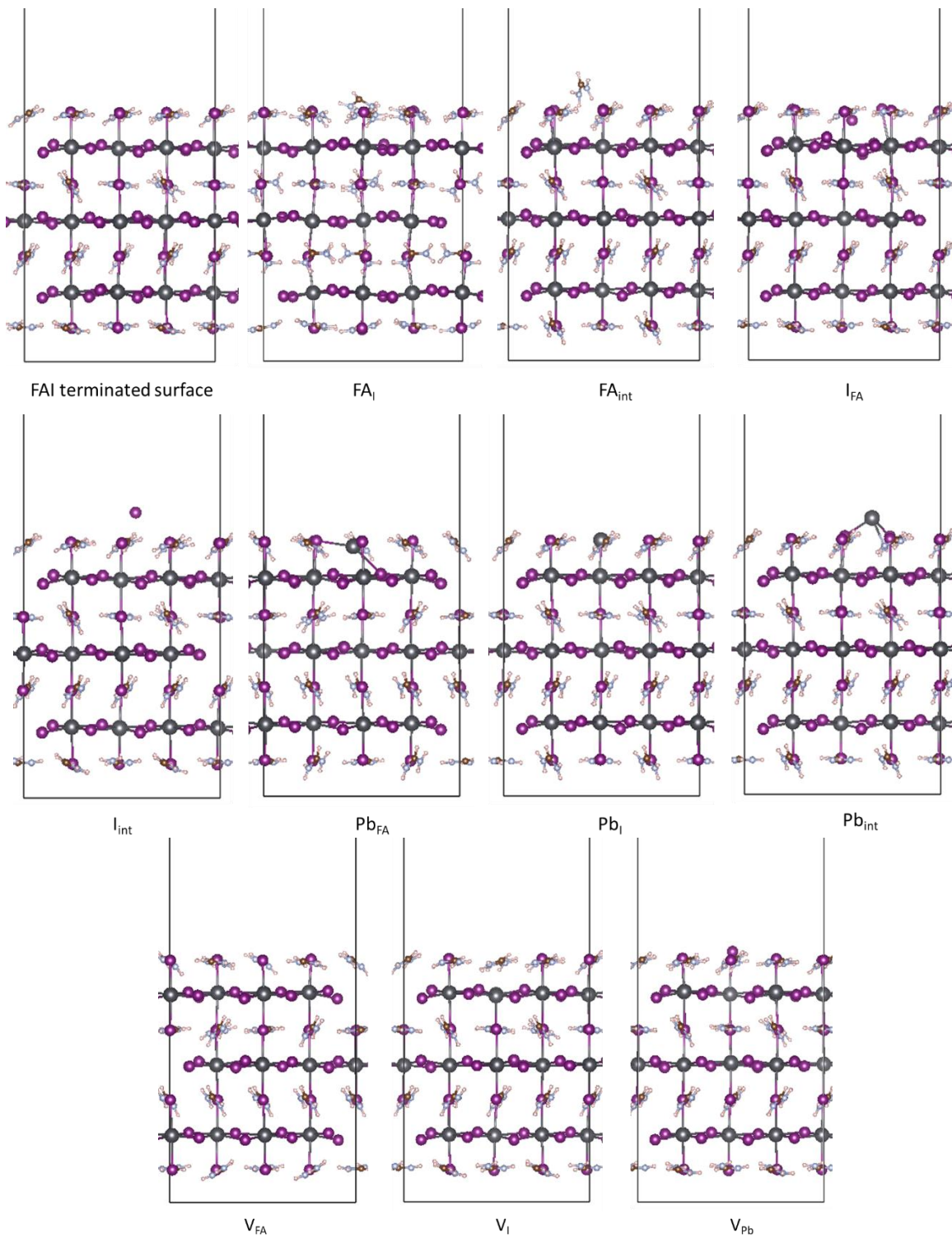
Supplementary Figure C4.19 Supplementary *J-V* characteristics of perovskite solar cell devices. (A) CsFAMAPb($I_{0.8}Br_{0.2}$)$_3$ and CsFAMAPbI$_3$ without OAI surface treatment; (B) CsFAMAPb($I_{0.95}Br_{0.05}$)$_3$.
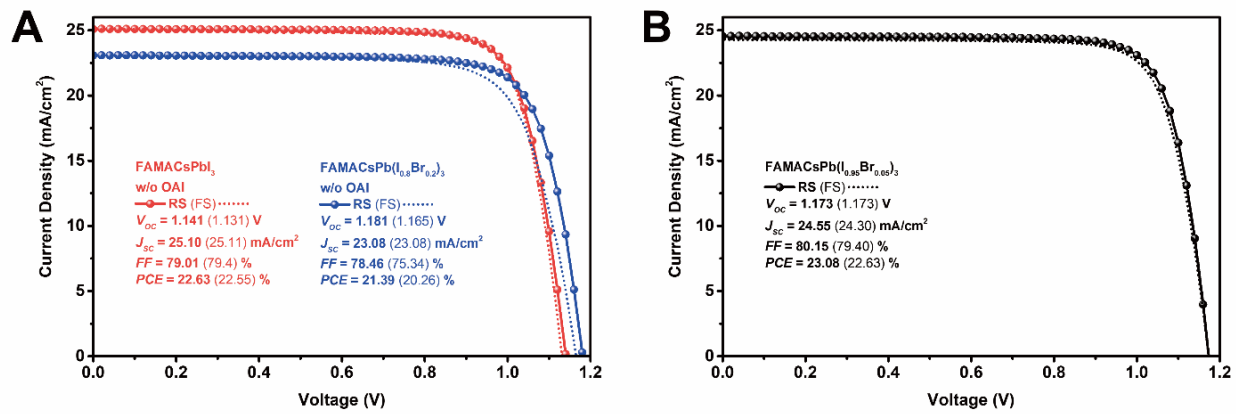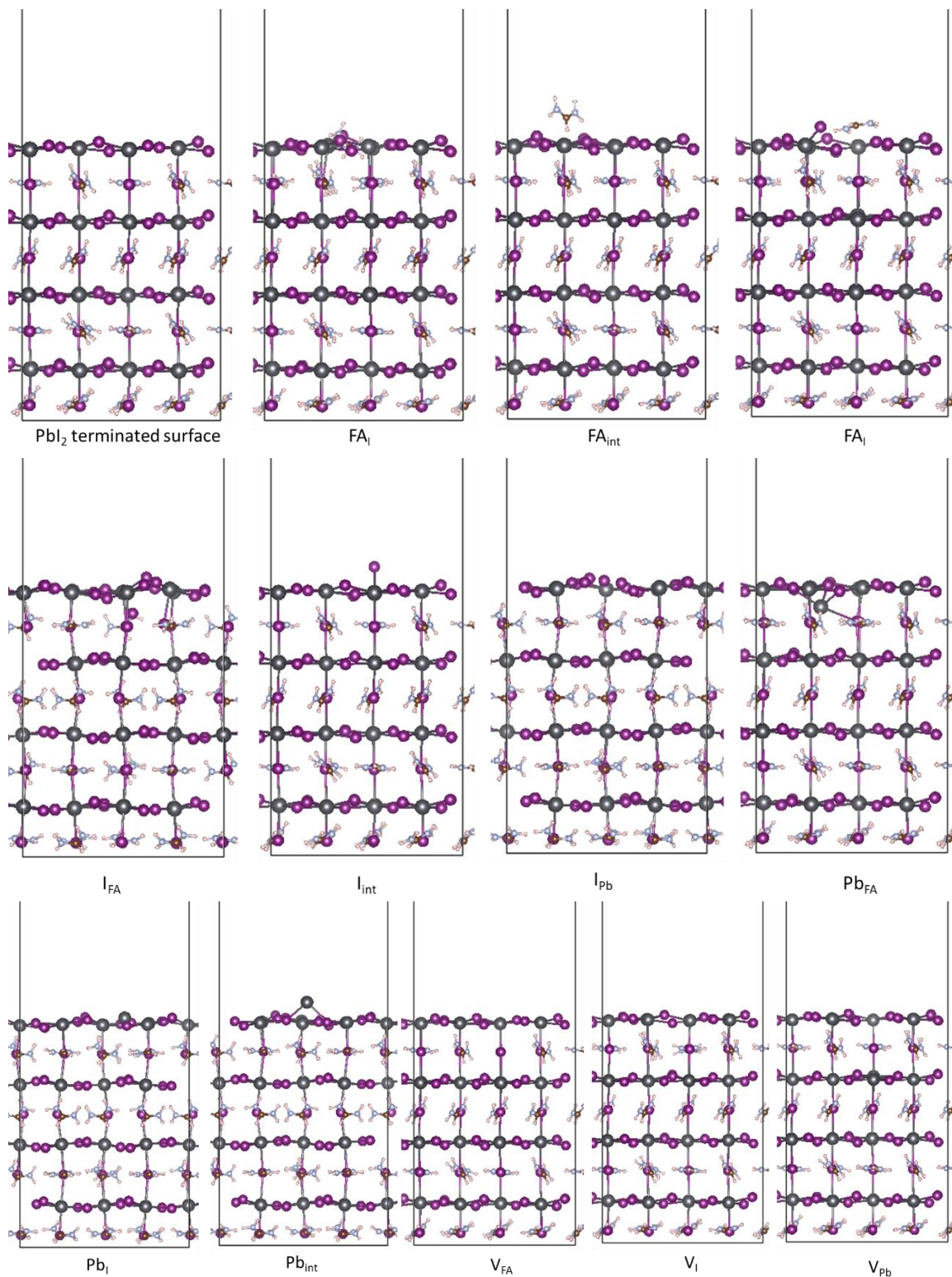
Supplementary Figure C4.20 Photo stability test of perovskite solar cells. The devices are based on $FAMACsPbI_3$ and $FAMACsPb(I_{0.8}Br_{0.2})_3$ under (A) non-encapsulated or (B) encapsulated conditions. Data was obtained from the average of 6 devices of each condition. The samples were aged under illumination of 90 ($\pm$10) mW/cm^2 at open-circuit and cooled by a mini fan during the test.
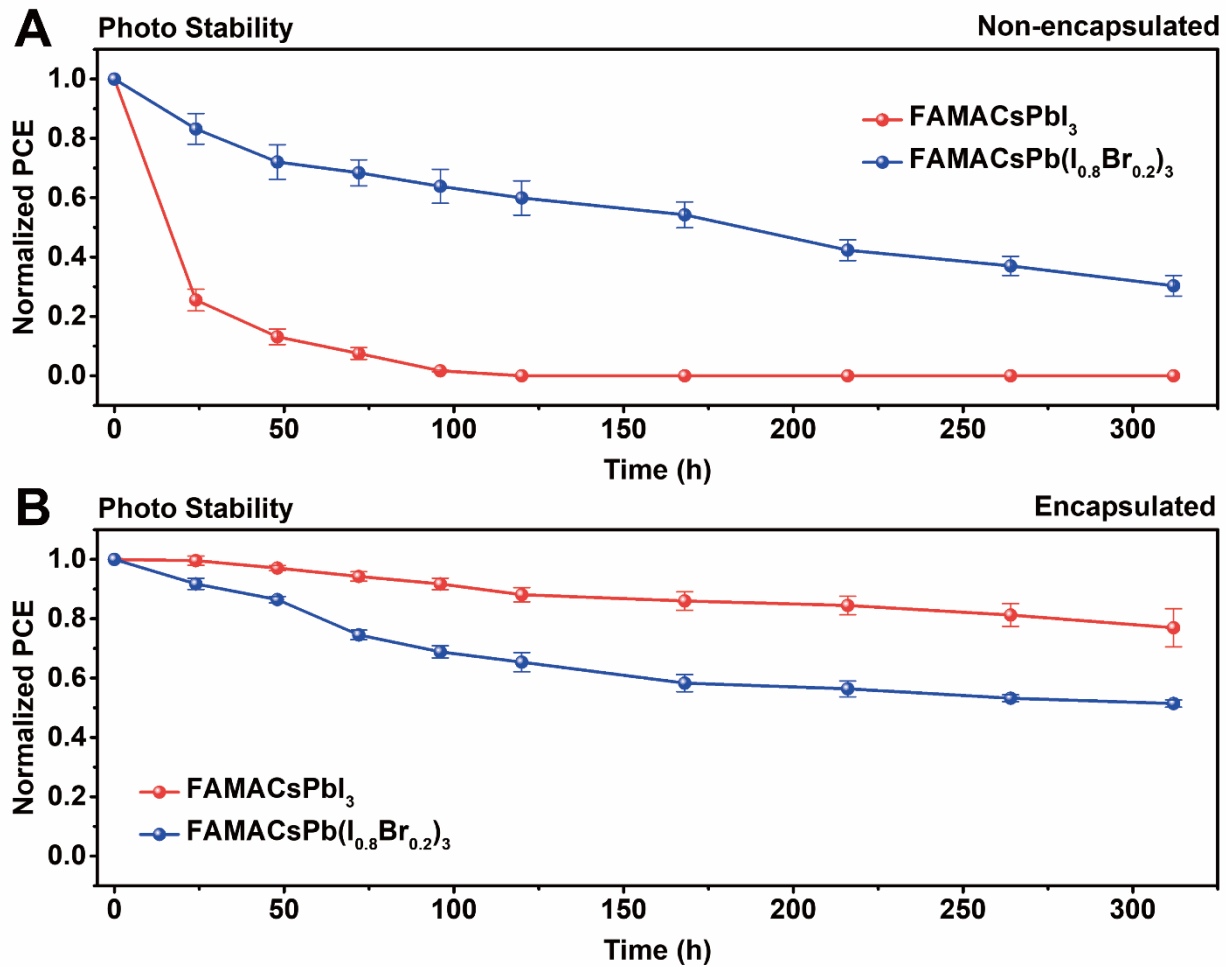
Supplementary Figure C5.1 Optimized geometries of FAI-terminated surface and the surface point defects.

FAI terminated surface

FA$_I$

FA$_{int}$

I$_{FA}$

I$_{int}$

Pb$_{FA}$

Pb$_I$

Pb$_{int}$

V$_{FA}$

V$_I$

V$_{Pb}$

Supplementary Figure C5.2 Optimized geometries of PbI$_2$-terminated surface and the surface point defects.

PbI$_2$ terminated surface

FA$_I$

FA$_{int}$

FA$_I$

I$_{FA}$

I$_{int}$

I$_{Pb}$

Pb$_{FA}$

Pb$_I$

Pb$_{int}$

V$_{FA}$

V$_I$

V$_{Pb}$

Supplementary Figure C5.3 Calculated density of states (DOS) of FA-I terminated FAPbI$_3$ perovskite with surface point defects that do not form deep-level traps.
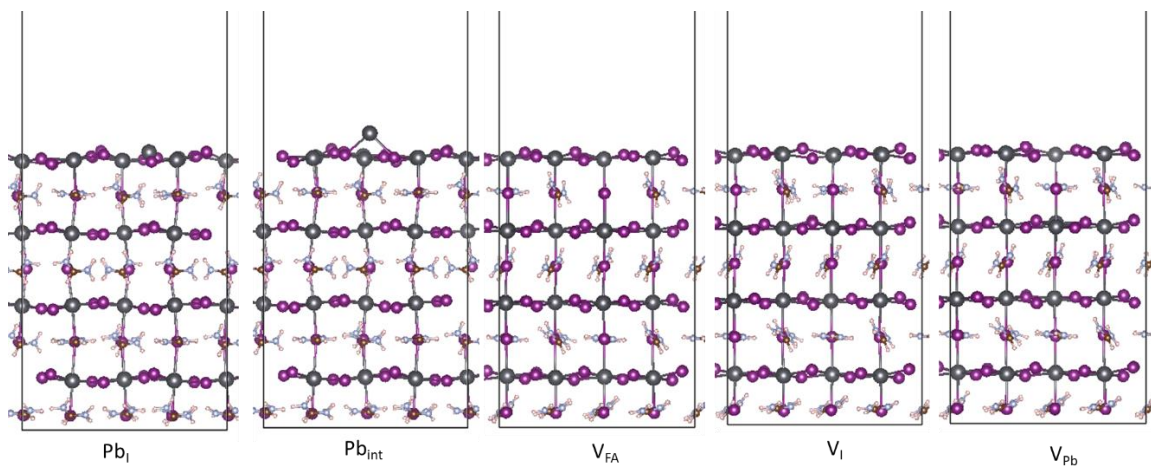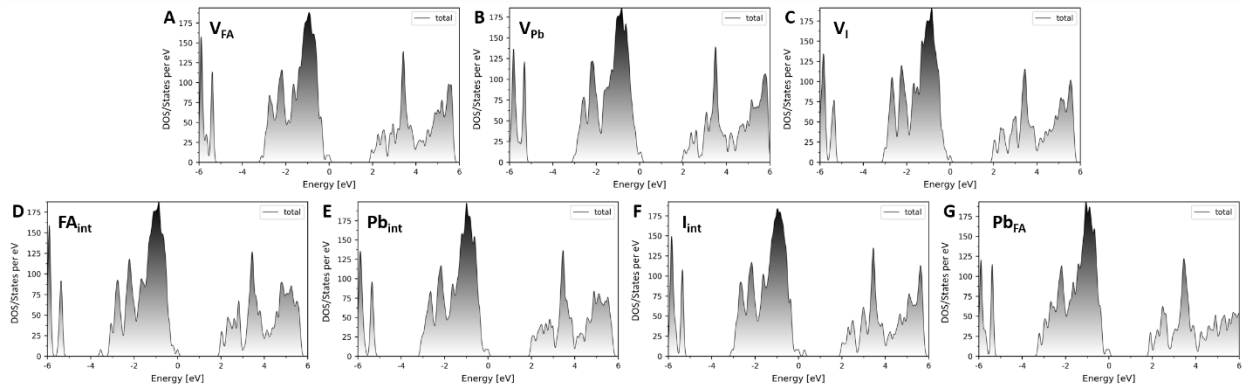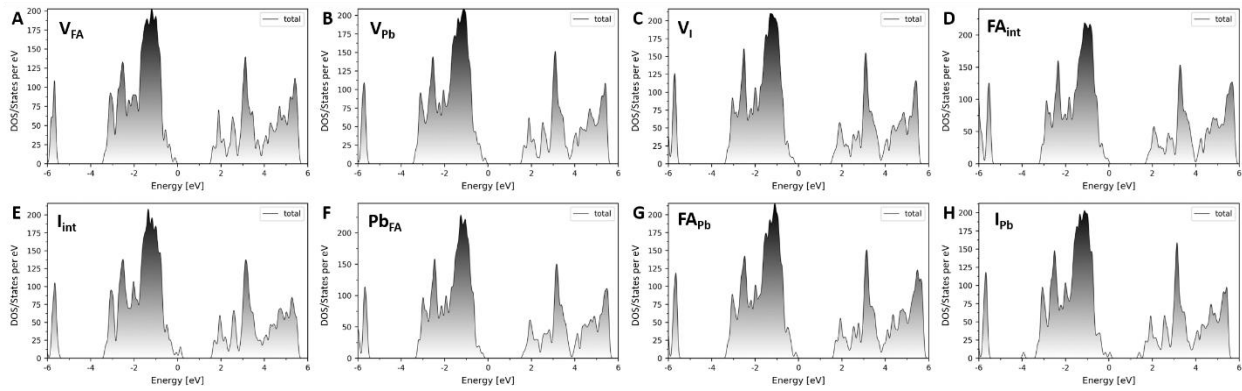
Supplementary Figure C5.3 Calculated density of states (DOS) of FA-I terminated FAPbI$_3$ perovskite with surface point defects that do not form deep-level traps.
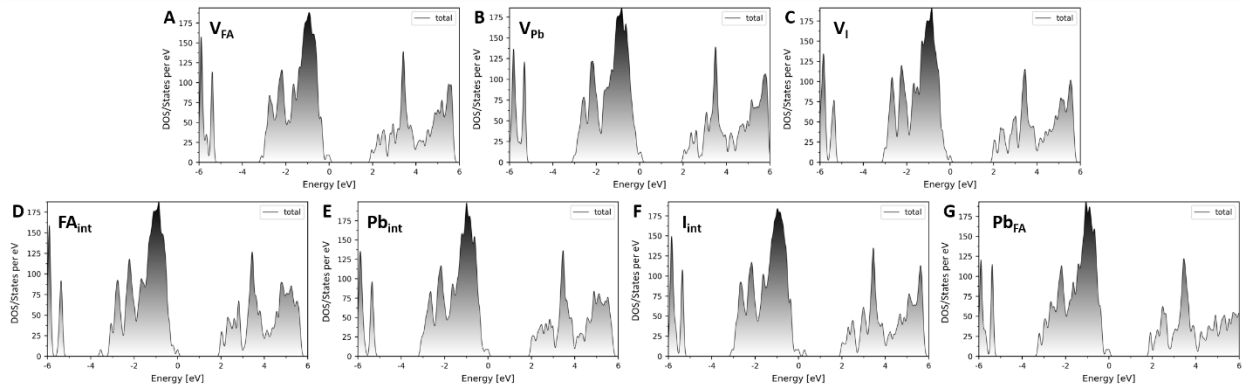
Supplementary Figure C5.4 Calculated density of states (DOS) of PbI$_2$ terminated FAPbI$_3$ perovskite with surface point defects that do not form deep-level traps.

Supplementary Figure C5.5 Complete XPS spectra of FAPbI3 thin films and the corresponding atomic ration of Pb and I.
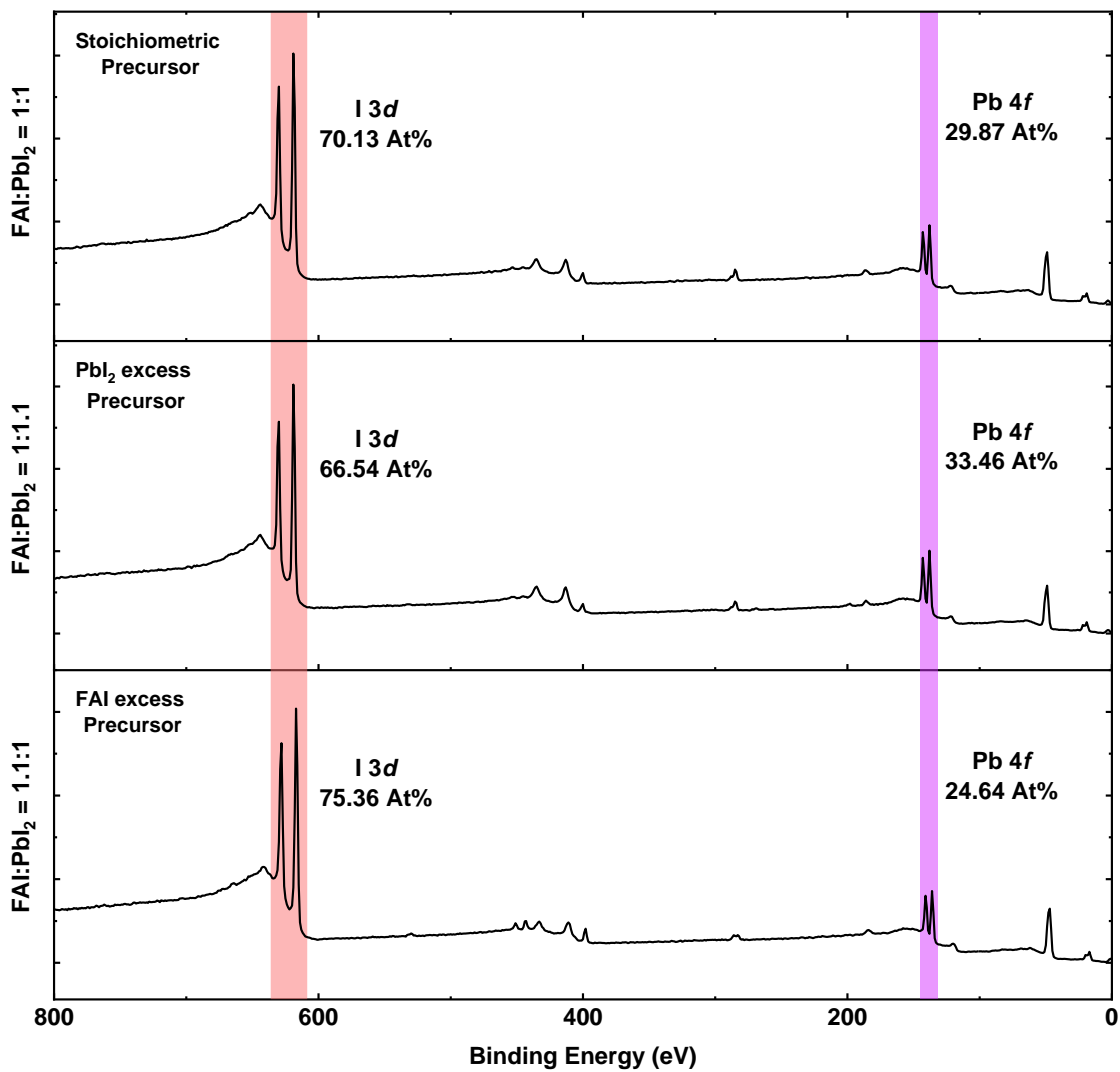
Supplementary Figure C6.1 ¹H NMR spectrum of 2-(6-oxo-5,6-dihydro-4*H*-cyclopenta[*c*]thiophen-4-ylidene)-malononitrile (INTC)
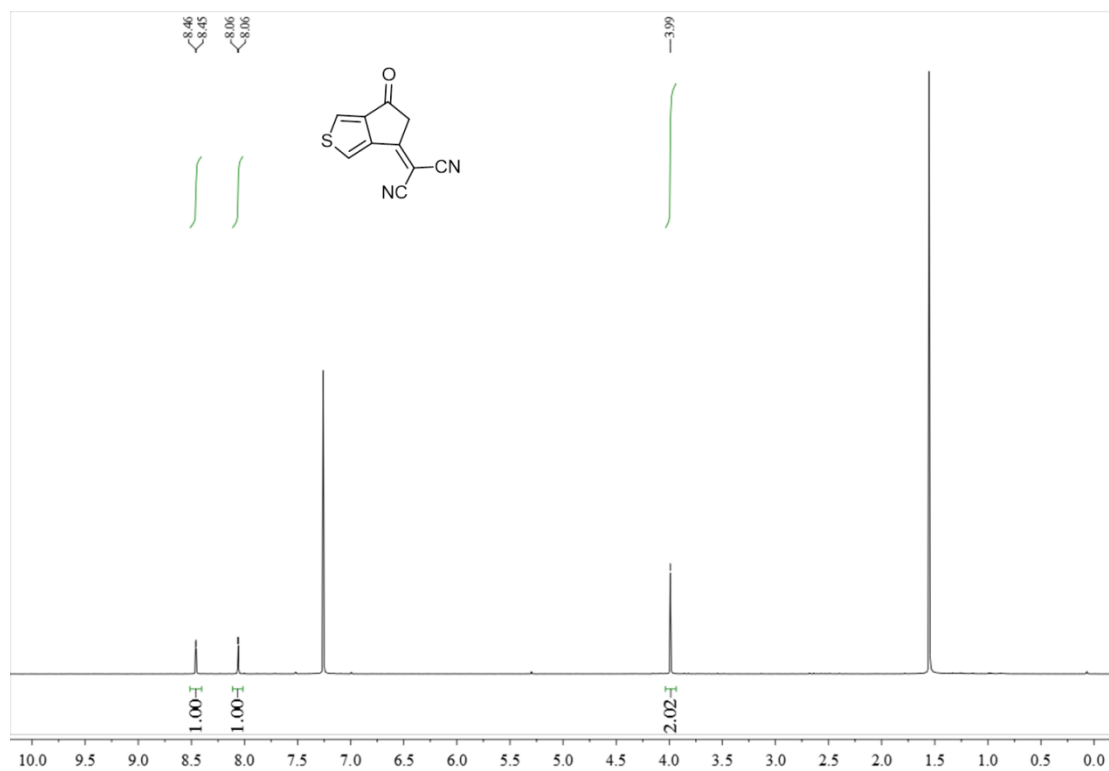
Supplementary Figure C6.2 ^{1}H NMR spectrum of compound 3.
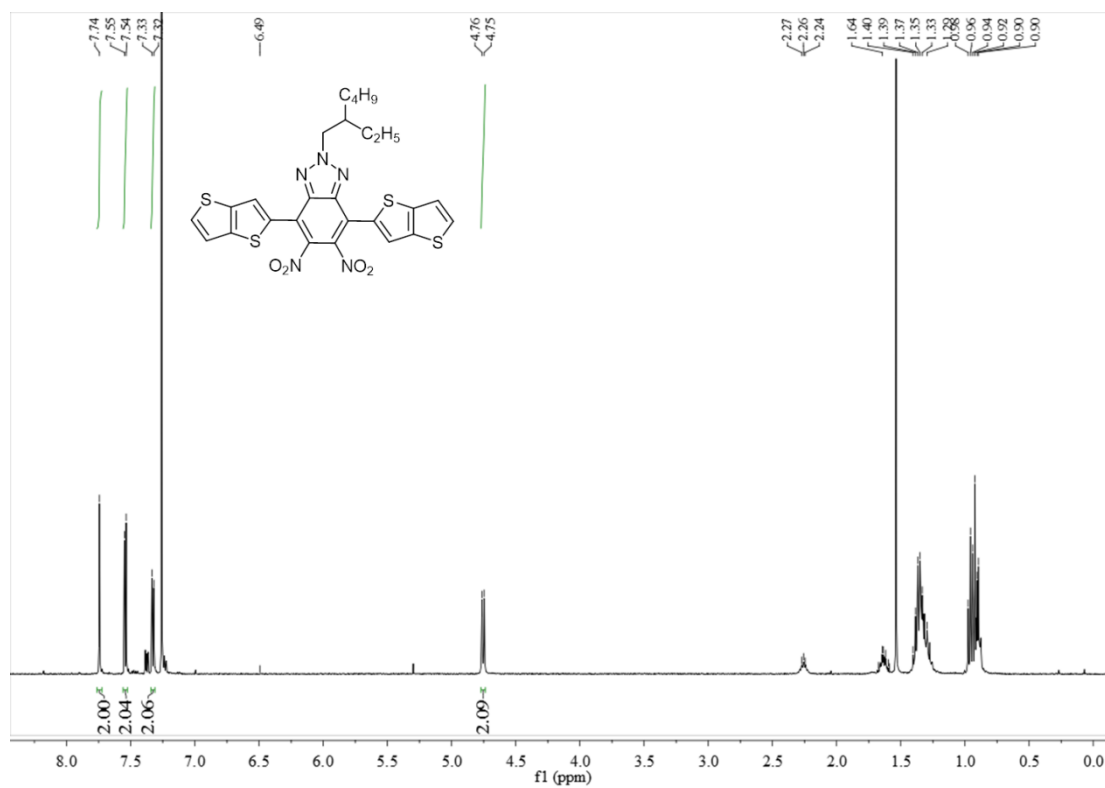
Supplementary Figure C6.3 ^{1}H NMR spectrum of compound 5.
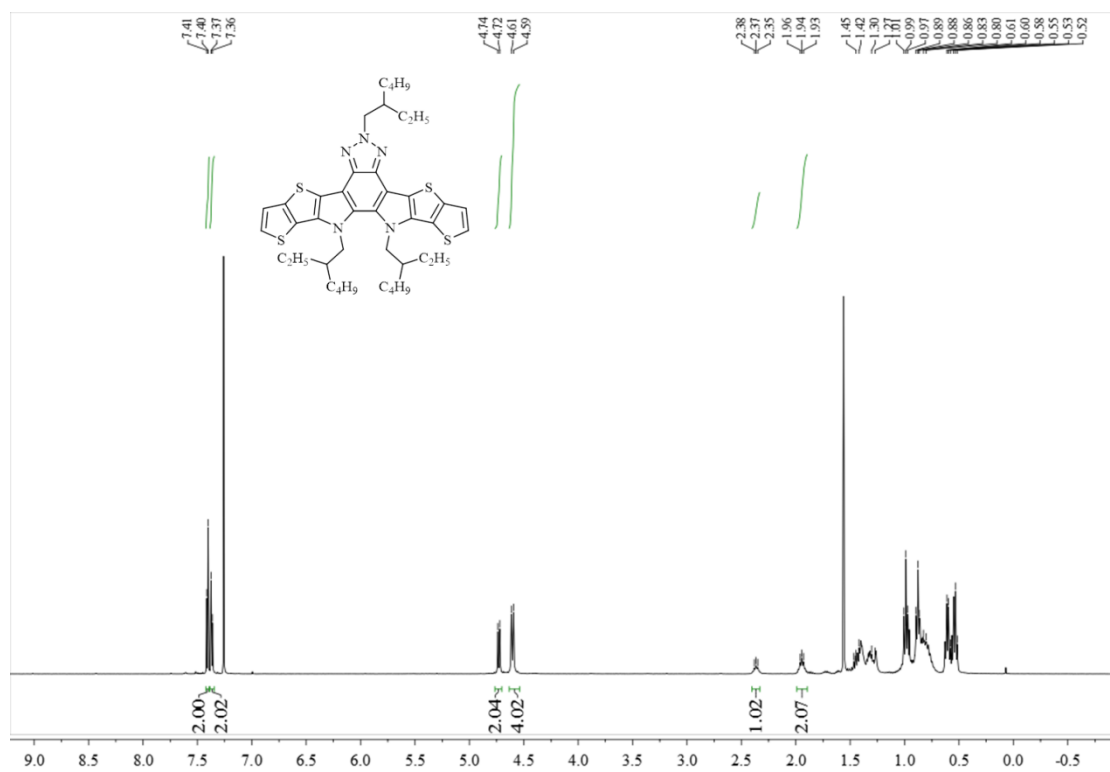
Supplementary Figure C6.4 ^{1}H NMR spectrum of compound 6.
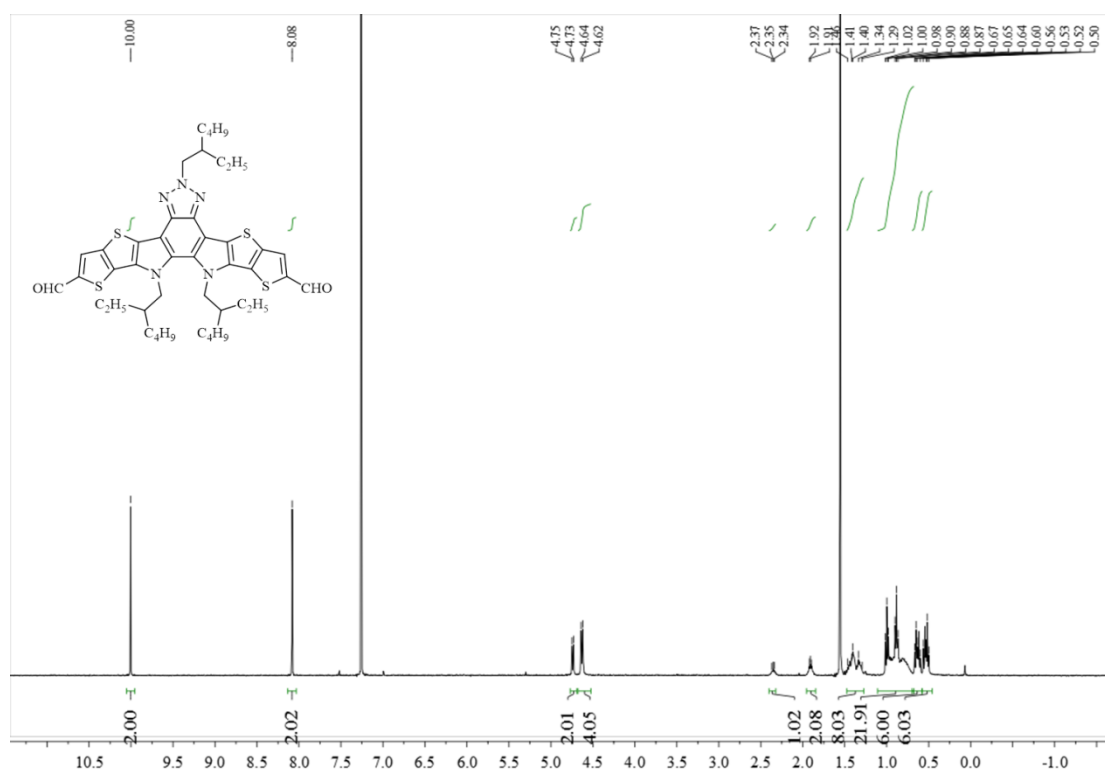
Supplementary Figure C6.5 ^{1}H NMR spectrum of Y1.
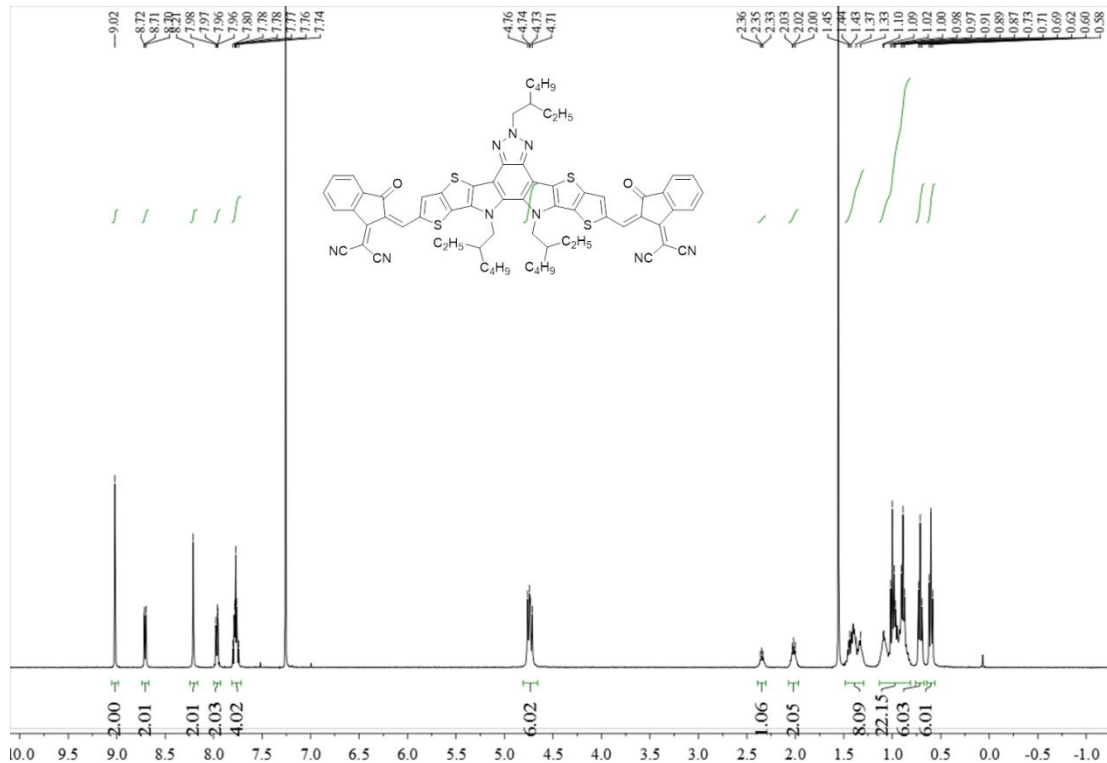
Supplementary Figure C6.6 ^{1}H NMR spectrum of Y2.
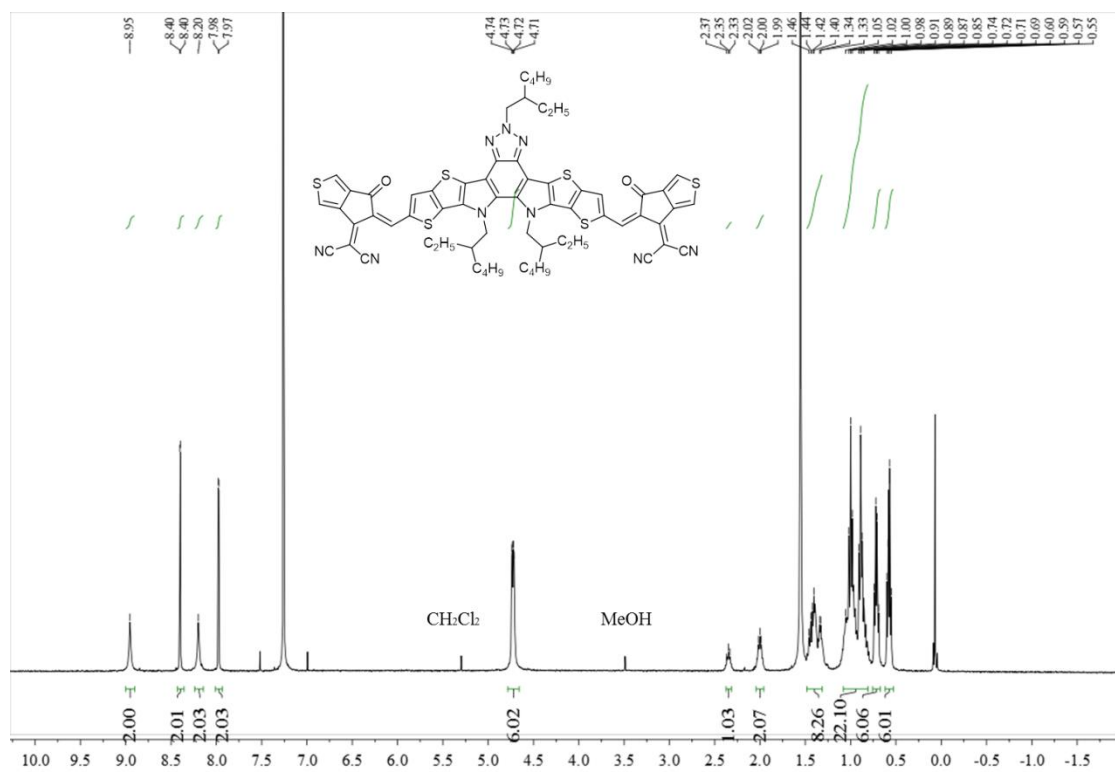
Supplementary Figure C6.7 The high resolution mass spectrum (MALDI-TOF) of Y1 and Y2
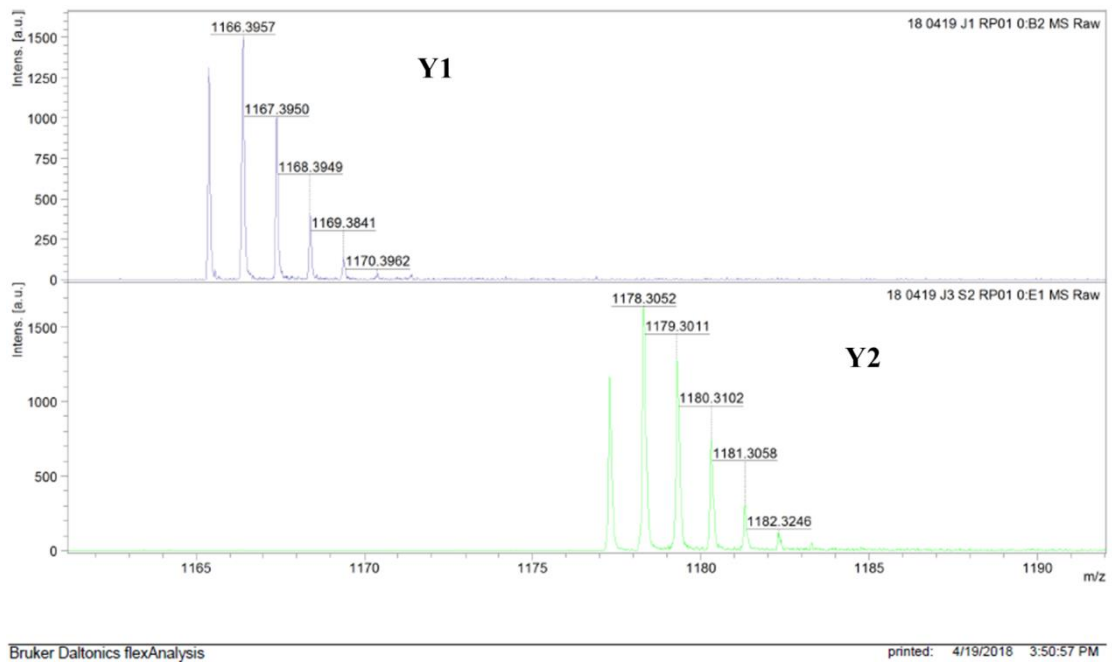
Supplementary Figure C6.8 (a) Molecular structural formulas of the donor (PBDB-T) and acceptors (Y1 and Y2) used. **(b)** Device architecture of the solar cells.

a

Y1 (acceptor)

Y2 (acceptor)

PBDB-T (donor)

b

172
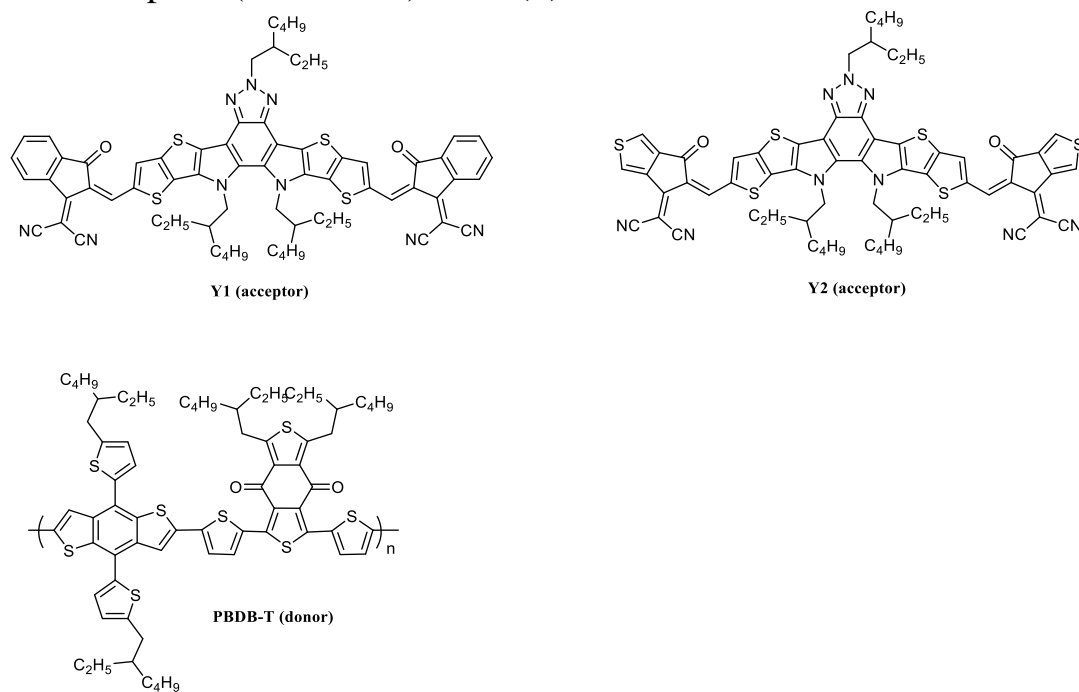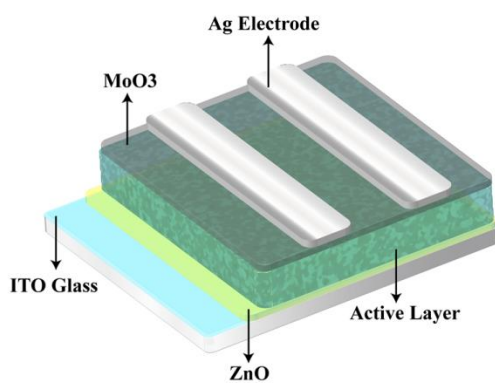
Supplementary Figure C6.9 Thermogravimetric analysis curves and heat flow curves of a, Y1. b, Y2 with a heating rate of 20 K min⁻¹.
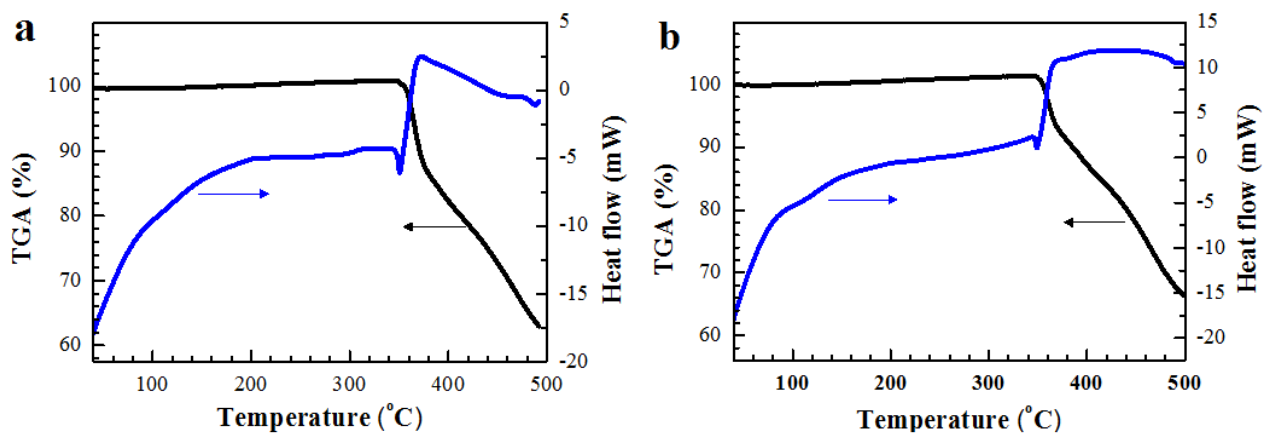
Supplementary Figure C6.10 Cyclic voltammograms of Y1, Y2 and PBDB-T films measured in 0.1 M Bu$_4$NPF$_6$ solution at the scan rate of 20 mV/s.
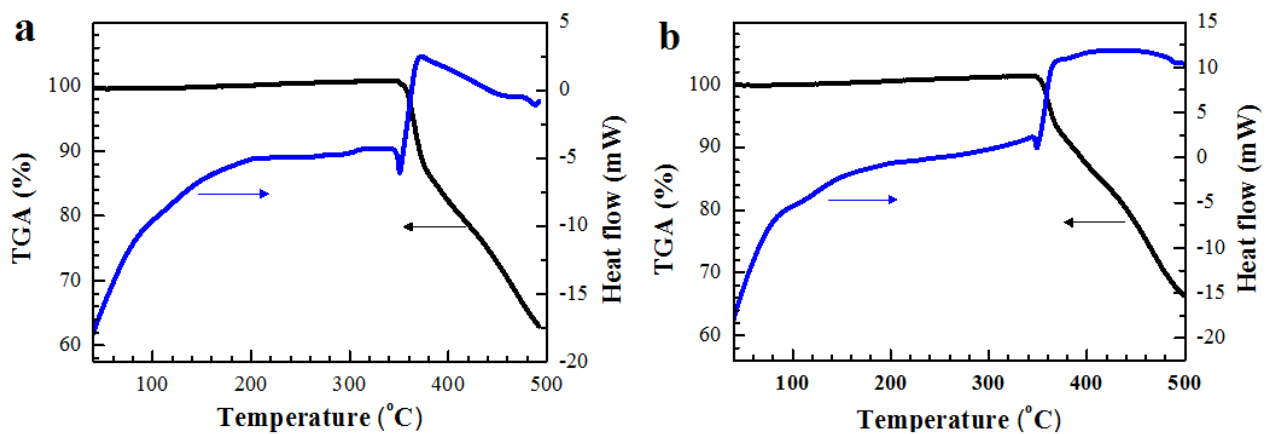
Supplementary Figure C6.11 *J-V* plots in both forward and backward direction of the cell based on PBDB-T:Y1.

Supplementary Figure C6.12 PCE verification by Newport. Independent certification by Newport Corporation of PBDB-T:Y1 blend film solar cell confirming a high V_{oc} of 0.88 V and a stability power conversion efficiency of 12.56 %.

Newport

Technology and Application Center
PV Lab

Calibration Cert. # 2893.01

Newport Calibration Cert. # 1908

DUT S/N: 7173902 T6
Newport Calibration #: 1908
Manufacturer: UCLA, Yang Yang and Central South University, China
Material: OPV
Measurement Date: 31-May-2018
Temperature Sensor: TC-K, DUT Temperature: 24.6 ± 0.6 °C
Environmental conditions at the time of calibration: Temperature: 24 ± 3 °C; Humidity: 40 ± 10 %

The above DUT has been tested using the following methods to meet the ISO 17025 Standard by the PV Lab at Newport Corporation. Quoted uncertainties are expanded using a coverage factor of k = 2 and expressed with an approximately 95% level of confidence. Measurement of total irradiance is traceable to the World Radiometric Reference (WRR) and all other measurements and uncertainties are traceable to either NIST or CNRC and the International System of Units (SI). The performance parameters reported in this certificate apply only at the time of the test, and do not imply future performance. *Designated area defined by thin metal aperture mask.

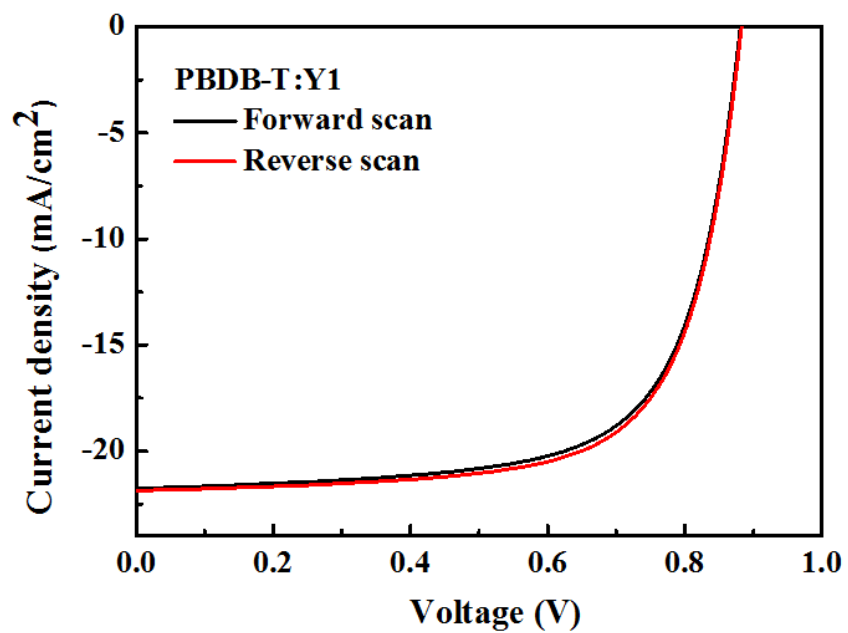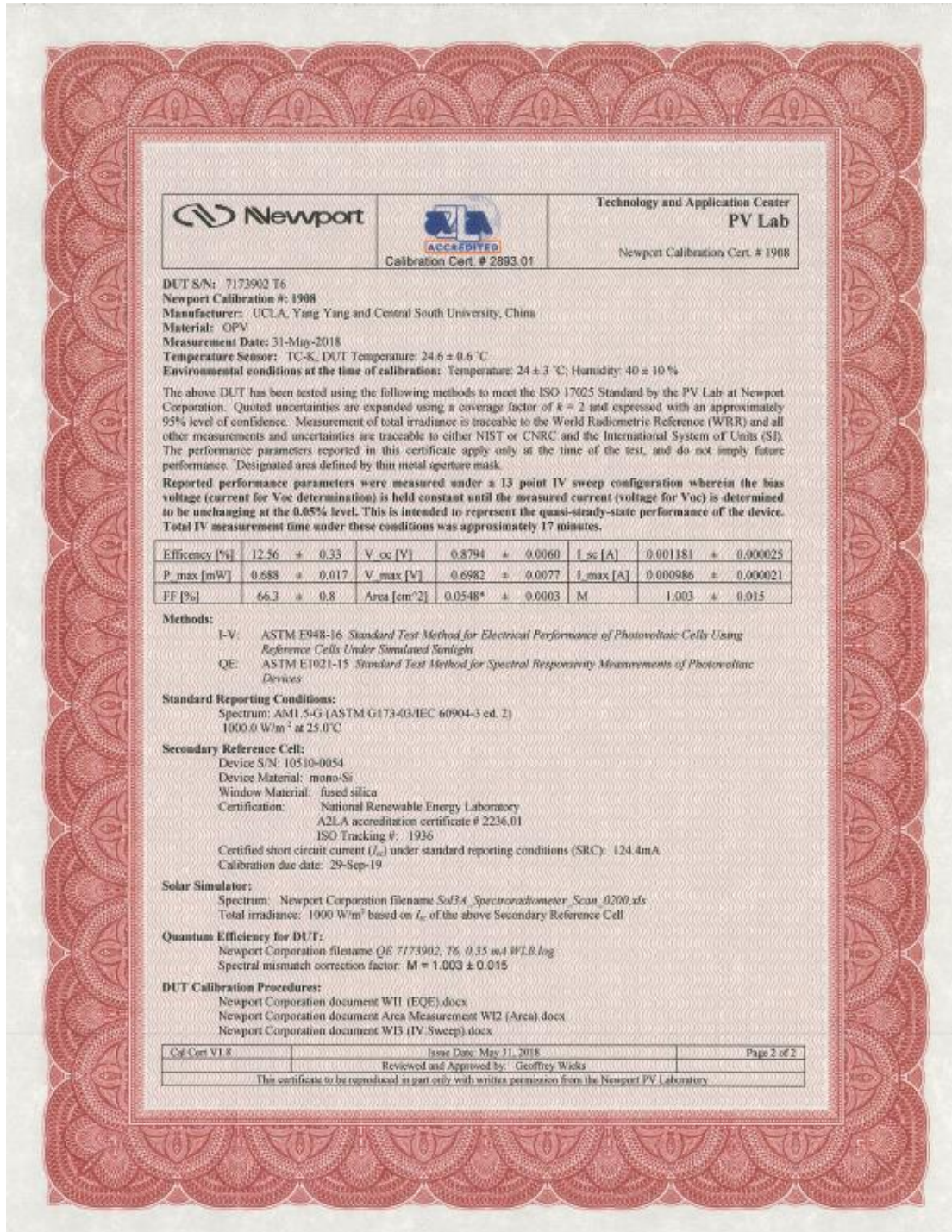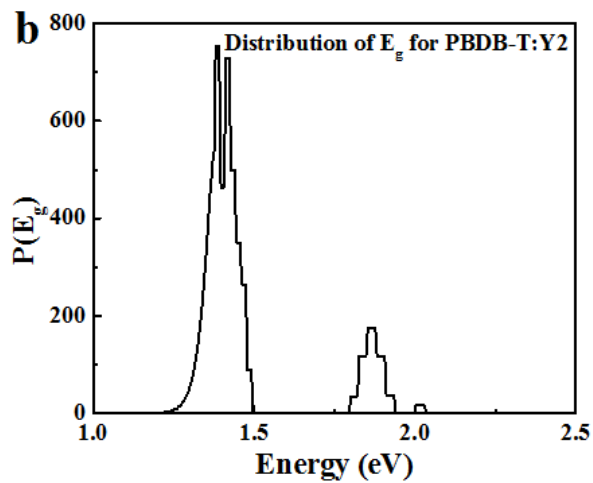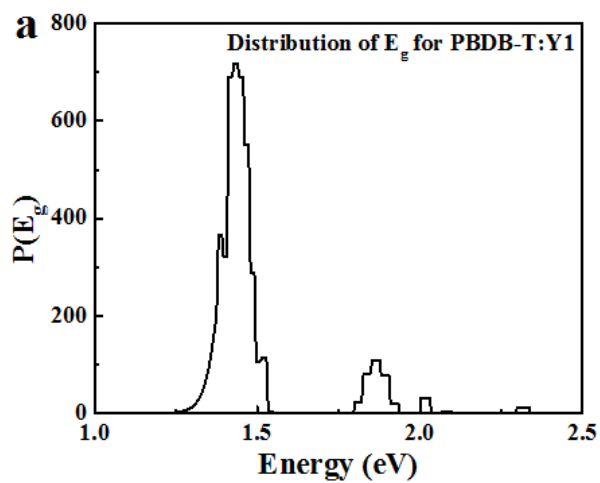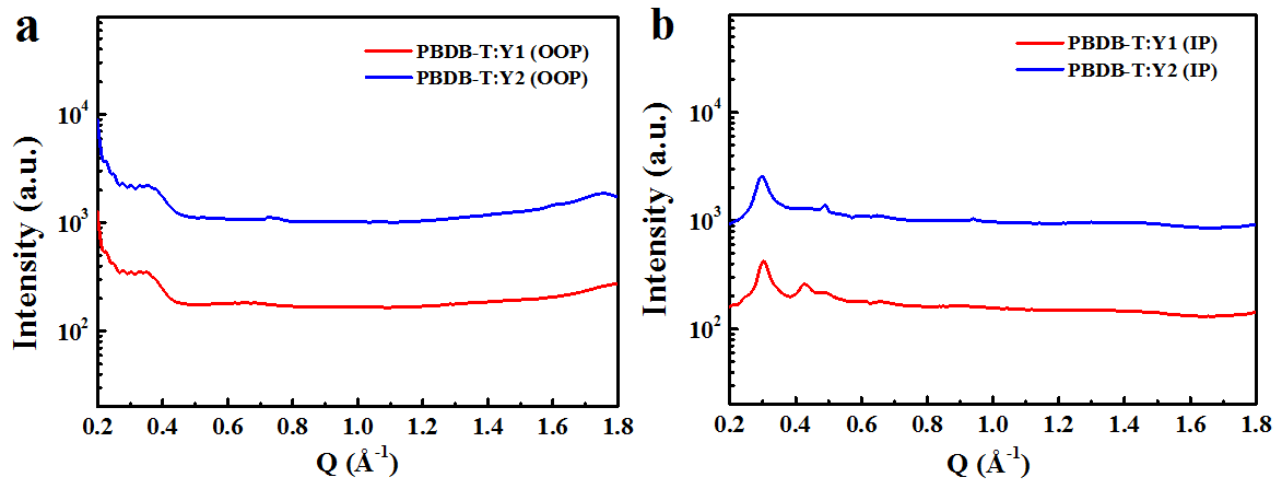Reported performance parameters were measured under a 13 point IV sweep configuration wherein the bias voltage (current for Voc determination) is held constant until the measured current (voltage for Voc) is determined to be unchanging at the 0.05% level. This is intended to represent the quasi-steady-state performance of the device. Total IV measurement time under these conditions was approximately 17 minutes.

Efficiency [%]	12.56	±	0.33	V_oc [V]	0.8794	±	0.0060	I_sc [A]	0.001181	±	0.000025
P_max [mW]	0.688	±	0.017	V_max [V]	0.6982	±	0.0077	I_max [A]	0.000986	±	0.000021
FF [%]	66.3	±	0.8	Area [cm^2]	0.0548*	±	0.0003	M		1.003	±	0.015

Methods:
I-V: ASTM E948-16 *Standard Test Method for Electrical Performance of Photovoltaic Cells Using Reference Cells Under Simulated Sunlight*
QE: ASTM E1021-15 *Standard Test Method for Spectral Responsivity Measurements of Photovoltaic Devices*

Standard Reporting Conditions:
Spectrum: AM1.5-G (ASTM G173-03/IEC 60904-3 ed. 2)
1000.0 W/m² at 25.0°C

Secondary Reference Cell:
Device S/N: 10510-0054
Device Material: mono-Si
Window Material: fused silica
Certification: National Renewable Energy Laboratory
A2LA accreditation certificate # 2236.01
ISO Tracking #: 1936
Certified short circuit current (I_{sc}) under standard reporting conditions (SRC): 124.4mA
Calibration due date: 29-Sep-19

Solar Simulator:
Spectrum: Newport Corporation filename *Sol3A_Spectroradiometer_Scan_0200.xls*
Total irradiance: 1000 W/m² based on I_{sc} of the above Secondary Reference Cell

Quantum Efficiency for DUT:
Newport Corporation filename *QE 7173902, T6, 0.35 mA WL8.log*
Spectral mismatch correction factor: M = 1.003 ± 0.015

DUT Calibration Procedures:
Newport Corporation document WI1 (EQE).docx
Newport Corporation document Area Measurement WI2 (Area).docx
Newport Corporation document WI3 (IV Sweeps).docx

Cal Cert V1.8		Issue Date: May 11, 2018		Page 2 of 2
	Reviewed and Approved by: Geoffrey Wicks			
	This certificate to be reproduced in part only with written permission from the Newport PV Laboratory			

Supplementary Figure C6.13 E_g distribution of PBDB-T:Y1 or Y2 solar cell.

Supplementary Figure C6.14 (a) Out-of-plane GIWAXS profiles for the PBDB-T:Y1 and PBDB-T:Y2 films. (b) In-plane GIWAXS profiles for PBDB-T:Y1 and PBDB-T:Y2 films.

Supplementary Figure C6.15 AFM height images (0.6 μm × 0.6 μm) of the active layers: (a) PBDB-T:Y1 film and (b) PBDB-T:Y2 film.
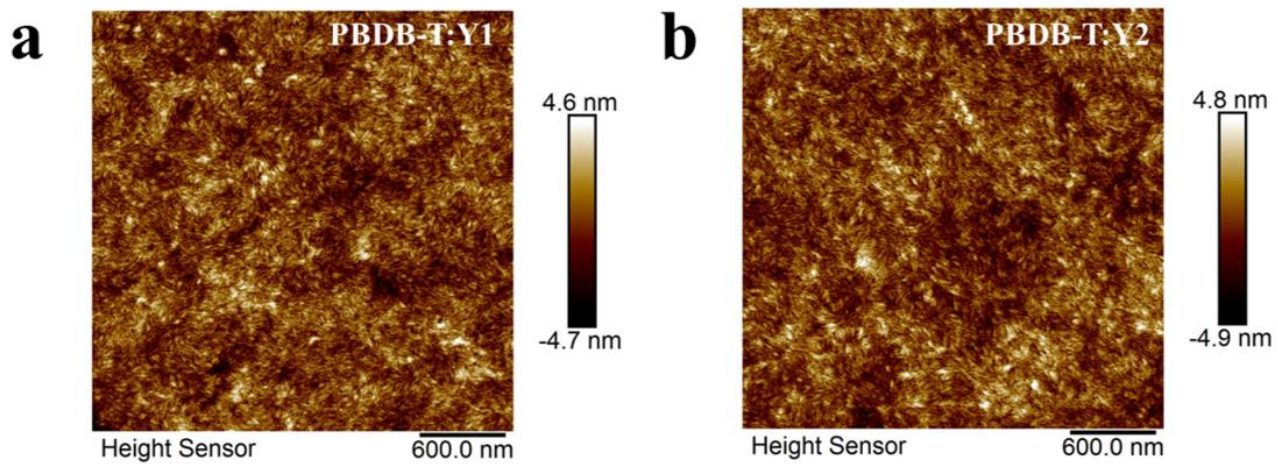
Supplementary Figure C6.16 (a) Hole-only and (b) electron-only devices based on PBDB-T:Y1 and PBDB-T:Y2 films.